

# UV light source for next generation immunoassay analyzer

**Rodenko, Olga**

*Publication date:*
2018

*Document Version*
Publisher's PDF, also known as Version of record

Technical University
of Denmark

RADIOMETER

# UV LIGHT SOURCE FOR NEXT GENERATION IMMUNOASSAY ANALYZER

PH.D. THESIS

Olga Rodenko

May 2018

## SUMMARY

The thesis presents a study of time-resolved fluorescence system designs based on novel light sources for Radiometers next generation immunoassay analyzer for *in vitro* diagnostics.

The general concept of time-resolved fluoroimmunoassays is given. The main parts constituting the basis of time-resolved fluoroimmunoassays, such as lanthanide based labels, time-resolved fluorimetry, and all-in-one dry cup concept, are explained. Critical analytical parameters of immunoassays are discussed.

The design, development and investigation of an optical system based on UV LED excitation at 340 nm for time-resolved fluorescence measurement of immunoassays are presented. For the first time to the authors knowledge, a LED based time-resolved fluorescence measurement system is successfully employed for immunoassays detection. The system is tested to measure cardiac marker troponin I in immunoassays. The signal-to-noise ratio is comparable to a state-of-the-art Xenon flash lamp based unit with equal excitation energy and without overdriving the LED. A comparative study of the flash lamp and the LED based system is performed and temporal, spatial, and spectral features of LED excitation for time-resolved fluorimetry are discussed. Optimization of the suggested key parameters of the LED promises significant increase of the signal-to-noise ratio and hence of the sensitivity of immunoassay systems.

Preliminary tests of an immunoassay analyzer employing an optimized LED excitation are reported, measuring on a standard troponin I and a novel research high-sensitivity troponin I assay. High-sensitivity cardiac troponin assay development enables determination of biological variation in healthy populations, more accurate interpretation of clinical results and points towards earlier diagnosis and rule-out of acute myocardial infarction. With the optimized LED based system, the limit of detection is improved by a factor of 5 for the standard troponin I and by a factor of 3 for the research high-sensitivity troponin I assay, compared to that of the flash lamp excitation. The obtained limit of detection was 0.22 ng/L measured on plasma with the research high-sensitivity troponin I assay and 1.9 ng/L measured on tris-saline-azide buffer containing bovine serum albumin with the standard troponin I assay.

The main highlight of the thesis is the first demonstration of an optimized LED excitation based point-of-care immunoassay analyzer. We have preliminarily fulfilled the high-sensitivity criteria for troponin measurements in immunoassays. The demonstrated results are an important step in the development of high-sensitivity troponin I assays for point-of-care testing, and will ultimately lead to more accurate interpretation of clinical results and earlier diagnosis and rule-out of acute myocardial infarction.

A general model of background noise sources in heterogeneous time-resolved fluoroimmunoassays is suggested. The suggested model can be generally applied to fluoroimmunoassays employing the dry-cup concept. The optimization of timing parameters in the time-resolved measurement of

lanthanide fluorescence is discussed. Impact of the light sources on main immunoassay parameters is discussed, and potentials and limitations of immunoassay measurements are investigated.

For the first time to the authors knowledge, a passively Q-switched, solid-state UV laser at 343 nm is demonstrated. The novel cost-effective passively Q-switched 343 nm solid-state laser delivers up to 20 µJ per pulse, with a pulse width of 2.3 ns at a repetition rate of 100 Hz. The 343 nm is obtained through third harmonic generation of a passively Q-switched 1030 nm Yb:YAG laser with pulse energy of 190 µJ at 100 Hz and a pulse width of 5.4 ns. The IR-UV conversion efficiency is 10.4%, comparable to that achieved with mode locked IR lasers. The light source is electronically controlled for easy synchronization with a detection circuit. The controllable low repetition rate specifically targets applications exploiting the millisecond scale lifetime of lanthanides employed in fluoroimmunoassay measurements for time-resolved fluorescence spectroscopy. Low repetition rate and even pulse-on-demand operation is demonstrated. The main challenges of the design of a high-power passively Q-switched solid state laser at 343 nm are discussed.

Finally, the results of laser induced time-resolved fluorescence measurements in immunoassays are presented. The impact of laser illumination area, narrow emission spectrum, and significantly higher peak power compared to the LED are discussed.

# RESUMÉ

Denne afhandling præsenterer et studie af et tidsopløst fluorescenssystem design, baseret på nye lyskilder til Radiometers næste generation af immunoassay analysatorer til in vitro diagnostik.

Der redegøres for det generelle koncept i tidsopløste fluoroimmunoassay analyse. De centrale dele af tidsopløst fluoroimmunoassay analyse forklares, herunder lanthanid baseret mærkning, tidsopløst fluorimetri, og all-in-one dry cup konceptet. De analytiske parametre for immunoassays diskuteres.

Designet, udviklingen og undersøgelsen af et optisk system baseret påUV LED excitation ved 340 nm af tidsopløst fluorescens måling af immunoassays præsenteres. Systemet testes til måling af den kardiologiske markør troponin I i immunoassays. Signal-til-støj forholdet var sammenligneligt med den nyeste Xenon blitz lampe baserede enhed med samme excitationsenergi, uden at overstyre LED'en. Et komparativt studie af det blitz lampe og det LED baserede system er blevet udført. Tidsmæssige, rumlige og spektrale egenskaber af LED excitation af tidsopløst fluorimetri diskuteres.

Optimering af de undersøgte nøgleparametre for LED lampen giver en signifikant forøgelse af signal-til-støj forholdet og dermed følsomheden af immunoassay systemet. Derudover rapporteres der om indledende tests af en immunoassay analysator ved brug af optimeret LED excitation. Her måles på en standard troponin I og en nyudviklet high-sensitivity troponin I assay. Udvikling af kardiologisk troponin assays med forøget følsomhed muliggør bestemmelse af biologisk variation i sunde populationer, dermed en mere præcis fortolkning af kliniske resultater, hvilket åbner muligheden for en tidligere diagnose og udelukkelse af akut myokardieinfarkt. Med det optimerede LED baseret system er grænsen for detektion forøget med en faktor 5 for standard troponin I, og med en faktor 3 for den nye troponin I assay med forøget følsomhed, i forhold til blitz lampe excitationen. Den opnåede grænse for detektion var 0.22 ng/L målt på plasma med troponin I assay med høj følsomhed og 1.9 ng/L målt på tris-saline-azide buffer indeholdende bovine serum albumin med standard troponin I assay.

Der foreslås en model til beskrivelse af kilder til baggrundsstøj i et heterogen tidsopløst fluoroimmunoassay. Den foreslåede model kan anvendes til fluoroimmunoassays ved brug af dry-cup konceptet. Optimeringen af timing parametre i tidsopløst detektion af lanthanid fluoroscens diskuteres. Lyskildens indflydelse på immunoassay parametre diskuteres. Potentiale og begrænsninger af immunoassay målinger undersøges.

Der rapporteres om en omkostningseffektiv passiv Q-switchet 343 nm solid state laser, der leverer op til 20 µJ pr. puls, med en pulsbredde på 2.3 ns ved en puls repetitionsfrekvens på 100 Hz. 343 nm opnås gennem tredje harmonisk generering af en passiv Q-switchet 1030 nm Yb:YAG laser med pulsenergi på 190 µJ ved 100 Hz og en pulsbredde på 5.4 ns. IR-UV-konverteringseffektiviteten er 10.4%, hvilket er sammenlignelig med hvad, der kan opnås med mode-locked IR-lasere. Lyskilden styres elektronisk for at få en simple synkronisering med et detekteringskredsløb. Den lave justerbare puls repetitionsfrekvens er specifikt målrettet mod anvendelser, der

udnytter millisekundlevetiden for lanthanider anvendt i fluorimmunoassaymålinger til tidsopløst fluorescensspektroskopi. Lav puls repetitionsfrekvens og endda pulse-on-demand operation demonstreres. De vigtigste udfordringer ved design af en passiv Q-switchet solid state laser ved 343 nm diskuteres.

Endelig præsenteres resultaterne af laserinducerede tidsopløste fluorescensmålinger i immunoassays. Betragtninger omkring størrelsen af det laser belyste områdes størrelse, laserens smalle emissionsspektrum og en væsentligt højere topkraft sammenlignet med LED'en diskuteres.

## PREFACE

The thesis presents the results of an industrial PhD project from June 2015 to June 2018. The Ph.D study is a collaboration between the Department of Photonics Engineering (DTU Fotonik) of Technical University of Denmark and the company Radiometer Medical ApS. The project is funded by Innovation Fund Denmark (grant 4135-00118B) and Radiometer Medical ApS. The experimental work was carried out in the laboratory facilities of the Optical Sensor Technology Group located at DTU Risø Campus and in the laboratory facilities of Radiometer Medical ApS.

Moreover, some experiments are performed in collaboration with Radiometer Turku, Finland. The assays employed in the project are manufactured by Radiometer Turku. In addition, a few experiments are carried out in Turku, Finland, with the system developed in this work.

## ACKNOWLEDGMENTS

I would like to thank my university supervisors, Christian Pedersen and Peter Tidemand-Lichtenberg. Without their continuous optimism, encouragement, support and sense of humour, this thesis would have never been completed. I consider it an honour to work with my dear colleagues of the Optical Sensor Technology group. Many thanks for the friendly atmosphere and assistance. Special thanks to Finn A. C. Pedersen for technical support.

I owe my deepest gratitude to my supervisors from Radiometer, Henrik Fodgaard, and Carl Peder Troldborg. I am particularly grateful to Esbjørn Schroll for support and encouragement throughout the project. Many thanks to the following people: Thomas Ernst, Allan Byrnard, John Petersen, Jesper Rene Lydestad-Hansen. I also thank the AQT laboratory staff, Sylvana van Os, and Benjamin Jørgensen. Many thanks to all Radiometer AQT team for the friendly atmosphere and assistance.

Many thanks to Susann Eriksson and Henri Sund for their constructive comments and valuable suggestions. I also thank Radiometer Turku team in Finland.

Olga Rodenko, May 2018

# CONTENTS

# PUBLICATIONS

Some ideas and figures have appeared previously in the following publications:

## JOURNAL PUBLICATIONS

1. O. Rodenko, H. Fodgaard, P. Tidemand-Lichtenberg, P. Petersen, and C. Pedersen, 340 nm pulsed UV LED system for europium-based time-resolved fluorescence detection of immunoassays, Opt. Express 24(19), 22135-22143 (2016).
2. O. Rodenko, S. Eriksson, P. Tidemand-Lichtenberg, C. Troldborg, H. Fodgaard, S. van Os, and C. Pedersen, High-sensitivity detection of cardiac troponin I with UV LED excitation for use in point-of-care immunoassay, Biomed. Opt. Express 8(8), 3749-3762 (2017).
3. O. Rodenko, P. Tidemand-Lichtenberg, and C. Pedersen, Low repetition rate 343 nm passively Q-switched solid-state laser for time-resolved fluorescence spectroscopy, Opt. Express 26(16), 20614-20621 (2018).

## PUBLICATIONS IN CONFERENCE PROCEEDINGS

1. O. Rodenko, H. Fodgaard, P. Tidemand-Lichtenberg, and C. Pedersen, 340nm UV LED excitation in time-resolved fluorescence system for europium-based immunoassays detection, Proceedings of SPIE Vol. 10072, 100720M (2017).

## PATENTS

1. O. Rodenko, H. Fodgaard, P280DK (2017).

# 1 INTRODUCTION

## 1.1 MOTIVATION

Specific detection of analytes in biological samples is critical for medical disease diagnosis and monitoring. The measurements require high sensitivity and specificity to enable early diagnosis and accurate interpretation of the results. Point-of-care (PoC) immunoassay instruments, in contrast to central laboratory, are employed in testing performed near the patient (e.g., in emergency units and intensive care departments), with the focus on a short turnaround time and automated testing [1, 2]. PoC instruments have to be easy to use, fast, reliable, and portable, and at the same time have the quality of results not inferior to that of central laboratory.

Immunoassay testing is widely employed in both PoC environment and in laboratories. It targets infectious, respiratory, cancer diseases, and cardiovascular testing. Immunoassays employ a unique antibody-antigen recognition to detect analytes, and are especially suited for the analysis of compounds at low concentration and in samples with little or no preparation, since their detection limits are very low. Because biological liquids exhibit high background, often an analyte needs to be physically separated from the other substances in a sample (heterogeneous assays). However, even heterogeneous immunoassays are limited or suffer from the background signal present without the analyte. One of the most sensitive immunoassays, time-resolved fluorescence immunoassay (TRFIA), is based on the combination of time-resolved fluorescence techniques and lanthanide based fluorescent labels. State-of-the-art PoC fluoroimmunoassay instruments have approached the performance of central laboratories in terms of sensitivity and specificity with equal or marginally inferior performance [3, 4].

Time-resolved fluorescence is a powerful tool that has been used in immunoassays detection to suppress short-lived background fluorescence and allow for high sensitivity [5, 6]. It relies on employing high-fluorescent fluorophores with long fluorescence lifetime and light sources emitting excitation pulses terminating prior to the gated measurement. A high sensitivity is reached when the excitation and detection events are separated in time. Moreover, the fall time of the excitation pulse has to be shorter than the delay between the excitation and detection [7, 8]. Time-gated fluorescence detection delayed by tens or even hundreds of microseconds exhibits improved signal-to-background ratio (S/B) and often improved signal-to-noise ratio (SNR) compared to steady-state measurements as it reduces interference from unwanted fluorophores having a fluorescence lifetime typically in the range of nanoseconds [5].

Many fluorophores with long fluorescence lifetime belong to the group of lanthanides which are commonly employed due to their long fluorescence lifetime and large Stokes shift [9, 10]. Europium $Eu^{3+}$ is a lanthanide ion

which has been widely used as a marker in time-resolved fluorescence instruments due to its large Stokes shift and long fluorescence lifetime (µs-ms) [11]. Europium chelates are excited in the UV-A region and emit fluorescence with an emission peak at 615 nm with a FWHM of 10-20 nm. The excitation peak of many lanthanides (europium, terbium) is approximately at 340 nm [10]. The excitation peak wavelength may vary slightly depending on the composition of the chelate. Moreover, many other fluorophores can be excited at this wavelength, including NADH [6, 12].

So far, flash lamps have been widely used as an excitation light source in fluoroimmunoassays (FIAs) with long fluorescence decay labels [13, 14]. Flash lamps are rather cost-effective, and have long lifetime (up to $10^9$ flashes [15]). However, they require high voltage of hundreds of volts. Flash lamps emit highly divergent light output, and are shown to exhibit a relatively long afterglow decay after emission of a pulse (hundreds of microseconds) [14]. Moreover, the employment of flash lamps is not efficient due to spatial and spectral filtering: only a small fraction of emitted light is used after collecting and spectrally filtering the light from their broad emission spectrum (180-2000 nm). Therefore, alternative light sources, which will potentially improve the measurements sensitivity, have been investigated.

UV LEDs have emerged as a new attractive light source for time-resolved excitation as shown in the following. LEDs have smaller footprint, less heat dissipation, higher wall-plug efficiency and higher operational stability compared to Xenon flash lamps. They are compact and cost-effective. Their narrowband emission spectrum, compared to flash lamps, allows better matching to particular peaks of the europium chelates excitation spectra. Moreover, LEDs exhibit no significant afterglow when compared to flash lamps [16]. Output power and temporal parameters of LEDs can be controlled easily by simple driver electronics in contrast to flash lamp systems. The technological advancement of LEDs has already resulted in the development of the lanthanide chelates based time-resolved systems using LED excitation at 365 nm: a 100 mW single LED at 365 nm with pulse duration of 101 µs and a gate delay of 5 µs was employed for excitation in time-gated luminescence microscopy [17]. UV LEDs at 365 nm have also been implemented for flow cytometry [18, 19, 20] and fluorescence microscopy [17, 21]. However, these LEDs do not match the excitation spectra of lanthanides well. 340 nm LEDs have until now been hampered by limited power [22]. Closest prior art has been LEDs at 340 nm with an output power up to 1 mW and dimension <100 µm in diameter which were employed in fluorescence lifetime measurements [23].

Laser sources have many advantages compared to other light sources, such as very narrow emission spectrum, high spatial beam quality, and the possibility to generate short pulses. The narrow (<1 nm) spectral bandwidth of the laser allows precise targeting of the lanthanides absorption peak. Moreover, the spatial beam quality of the laser enables easy light shaping and additionally makes 2D scanning of a sample possible with a high spatial resolution. With this in mind, we believe the precise spectral and spatial targeting of lanthanide fluorophores will allow for improved signal-to-noise-ratios in fluoroimmunoassay measurements. However, higher cost and increased complexity of a laser, compared to a LED, may be prohibitive

factors in relation to a PoC product, but very interesting for the system performance analysis.

One approach to design a UV laser source is based on a Q-switched NIR laser followed by a cascade of nonlinear conversion processes from the infrared to the UV wavelength, i.e. using third harmonic generation (THG) of the solid-state laser. Laser transitions of an Yb:YAG crystal allows for emission at the 1030 nm wavelength, which can then be tripled to obtain the desired 343 nm wavelength. The long upper state lifetime of Yb:YAG (1 ms) promotes high pulse energies and low repetition rates in a Q-switched configuration. Other advantages of Yb:YAG crystals are the small quantum defect and relatively simple energy level diagram, however, the latter at the same time leads to reabsorption due to the materials quasi-three-level operation. Advantages of passively Q-switched lasers include simplicity, cost-effectiveness and compactness compared to actively pulsed light sources. For excitation of lanthanides with long fluorescence lifetime (approximately 1 ms), low repetition rate is required to avoid cross talk between successive measurements. Such low repetition rates cannot be obtained with mode locked lasers without using pulse pickers [24].

In prior work at 343 nm, the following pulse energies have been obtained: 28.6 µJ at a repetition rate of 3.5 MHz, obtained from a mode locked IR laser delivering 177 µJ and a peak power of 240 MW, corresponding to an IR-UV conversion efficiency of 16% [25]. 780 µJ at 300 kHz, pumped with a mode locked thin disk laser amplifier with 4.7 mJ and a peak power of 590 MW, corresponding to IR-UV conversion efficiency of 17% [26]. These laser sources possess a high degree of complexity and are therefore expensive. However, the high peak power of mode locked lasers promotes high conversion efficiency of the third harmonic generation. High-power passively Q-switched Yb:YAG/Cr4+:YAG lasers have been demonstrated [27]. The highest pulse energies at 1030 nm have been achieved with composite Yb:YAG/$Cr^{4+}$:YAG microchip lasers: 1.6 mJ at a repetition rate of 50 Hz (pumped with 86 mJ at 50 Hz and a peak diode power of 100 W) [28], 3.6 mJ (pumped with 60 mJ at 20 Hz and peak diode power of 120 W) [29]. Third harmonic generation of passive Q-switched lasers has been demonstrated at the wavelength of 355 nm with pulse energy of 57 µJ at 38.6 kHz [30]. A UV laser, based on a frequency tripled mode-locked Nd:YAG laser, has been used for time-resolved fluorescence detection [31].

Moreover, the high spatial beam quality and brightness of lasers allows for for single molecule detection even in a solution, where biological liquid background is very high [32]. A single molecule detection immunoassay employing a laser as an excitation source has been demonstrated [33, 34].

## 1.2 HISTORICAL OVERVIEW

The quantitative immunoassay testing revolutionized the detection of biological analytes in early 1960s [35]. The first labeled immunoassays employed radioisotopic elements as labels were described in [36]. For a long time before the advent of fluorescence and enzyme immunoassays, the radioisotopic assays (RIA) were the most sensitive assays. However, RIA testing was based on counting trace quantity of radioactivity, and has severe drawbacks as the radio hazard and problems with radioactive waste. Therefore, alternative

immunoassays, employing non-radioisotopic labels, have been investigated and developed.

Fluorescence immunoassays (FIAs), employing fluorescence labels, have been gradually developing and at first were inferior to radioisotopic assays, until they reached the same sensitivity compared to RIAs in late 1970s and 1980s [5, 37]. Time-resolved FIAs based on lanthanide labels, exploiting its long fluorescence lifetime to obtain higher sensitivity were presented in [38, 39]. Since then, separation-based, time-resolved fluorescence immunoassays have outperformed radioimmunoassays.

The first time-resolved FIAs employed flash lamps with mechanical choppers [13], and argon lasers with a chopped modulator [7, 8] as excitation sources. In addition, nitrogen lasers have been implemented [40, 41, 42]. Nitrogen lasers emit at 337 nm and operate at very low repetition frequencies (typically 20 Hz). Because of the low repetition rate, only a few laser pulses can be used for the measurement, which limits its dynamic range. Nitrogen lasers are bulky, expensive, and the wall-plug efficiency is low.

## 1.3 PROJECT OBJECTIVES

The main objective of this project is design, development and investigation of a time-resolved fluorescence measurement system based on novel light sources for next generation of Radiometers immunoassay analyzer for *in vitro* diagnostics. Novel LEDs and UV solid-state lasers are investigated and bench marked against Radiometers current flash light source for use in the next generation Radiometer immunoassay analyzer. The project goals include:

1. Design of an LED based time-resolved fluorescence measurement system.
2. Design of a solid-state passively Q-switched UV laser at 343 nm with sufficient pulse energy, low repetition rate, and good stability.
3. Design of a laser based time-resolved fluorescence measurement system.
4. Assessment of the light sources potential and limitations for the use in time-resolved fluorescence system for immunoassays.
5. Investigation of potential improvements of the measurement sensitivity.

In addition, we investigate the impact of the light sources on the instrument performance, analyze the optimal configurations, and perform optimization analysis. The overall aim is to point to the optimal light source for next generation of Radiometers immunoassay analyzer, as well as to establish a platform for fundamental investigations of novel chelates.

## 1.4 THESIS STRUCTURE

In Chapter 2, the concepts of immunoassay testing and time-resolved fluorescence spectroscopy are explained. Most important concepts that constitute

the basis of the time-resolved fluoroimmunoassays are discussed, such as light sources, detectors, lanthanide based fluorophores, all-in-one dry concept technology, and analytes. In Chapter 3, the developed LED based time-resolved fluorescence system is described. Chapter 4 presents measurements of cardiac marker troponin I with the developed LED based immunoassay analyzer. Moreover, an investigation of background noise sources in time-resolved fluoroimmunoassays is presented, and consequently, optimization of the measurement analytical sensitivity is performed. Next two chapters report on the developed laser system and the laser induced time-resolved fluorescence measurements. In Chapter 5, the passively Q-switched solid state light source at 343 nm, obtained by third harmonic generation of a Yb:YAG laser at 1030 nm, is developed and investigated. Chapter 6 presents the results of the laser excited time-resolved fluorescence measurements of troponin I. Finally, the work is summarized in Chapter 7.

# 2 IMMUNOASSAYS

## 2.1 OVERVIEW

Immunoassays (IAs) are quantitative analytical tests which can be used to measure biological analytes. IAs are based on highly specific recognition reaction between an antibody and a respective determinant site of an antigen. An antigen is an immunogenic compound which can elicit the response of the immune system. It can be a peptide, protein, polysaccharide, or a polymeric compound [35]. The immunodeterminant side of an antigen is called an epitope and is recognized by the antibody. Figure 2.1 shows an antibody with an antigen attached to one of its binding sites. Antibodies are labeled to detect presence, localize, or measure the concentration of an antigen. IA instruments are widely employed in *in vitro* clinical diagnosis as an aid for the detection of various diseases, including bacterial, viral, parasitic and autoimmune. Measurement can be performed on a patient's blood, serum, plasma, urine, or saliva. In addition, the antibody-antigen reaction can also be employed in flow cytometers, which are particle counters with applications in clinical research (immunology, hematology, microbiology).

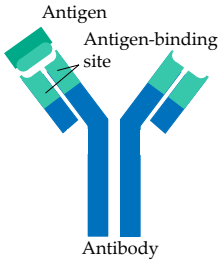


Figure 2.1: The specific recognition of an antibody and an antigen.

IAs are most often classified according to the employed labeling technology and in terms of how the immunoreaction occurs, although more classification types exist. Alternative to radioisotope labels which pioneered the first IAs, antibodies can be labeled by enzymes (biological proteins that catalyse specific reactions and produce an amplification effect), fluorescent markers, chemi-, and bioluminescent labels [43]. The immunoreaction takes place either in a solution (homogeneous IA) or in a solid phase (heterogeneous IA). The latter IAs are also called separation based, due to a physical separation of the bound labeled antibodies from the free unbound reagents prior to measurement. The bound fraction is then measured. Typical solid phases for a heterogeneous IA include microtitre plates, membranes and tissue slices, to which the antigen is either bound directly or on which it is captured by use of an appropriate antibody. A typical homogeneous assay utilizes two differently labeled antibodies which interact with one another in some way (e.g. by luminescence resonance energy transfer) in the presence of the target antigen. For a detailed table on immunoassay types, see Appendix A.1.

Depending on target analyte and application, different labels are used. Fluoroimmunoassays (FIAs) employing fluorescent labels as the means of detection are some of the most sensitive IAs and are discussed below. The main challenge with the fluorescent probes is background interference. In time-resolved fluorescence immunoassays (TRFIA), this issue is significantly alleviated. Employing the novel light sources, the sensitivity of FIAs can be potentially enhanced.

It should be noted that here and throughout the thesis the term sensitivity is not applied in the context of clinical research, where it relates to the rate

of true positive tests identified correctly. Here, it relates to the detection capabilities of an assay.

## 2.2 FLUOROIMMUNOASSAYS

Fluorescence labels are highly specific as the collected fluorescence signal is defined by the label excitation and emission spectra and sometimes also by the decay lifetime (time-resolved techniques). The variety of fluorescent probes includes organic fluorophores: fluorescein (FITC) and the derivatives, rhodamines, etc., organometallic: lanthanide chelates, fluorescence enhancement assays and others.

The fluorescence of endogenous constituents of a biological sample (plasma, serum, blood cells) is a problem in homogeneous assays and increases the background interference [44]. In heterogeneous assays, the problems of endogenous interference are solved by separating the analyte from the other components in the sample. However, in diagnostic testing, very low concentration of analytes are measured and thus high sensitivity is required. The main issue with heterogeneous assays remains to be the background fluorescence. Therefore, the materials used in heterogeneous assays must be chosen carefully. Some optical materials, such as glasses and plastics, exhibit high fluorescence [35]. Standard fluorophores emitting on a nanosecond scale (organic fluorophores) cannot reach the high sensitivity since they interfere with the background. In contrast, the TRFIAs, employing time-resolved fluorescence and lanthanides as labels, allow measuring very low concentrations. Another factor hampering the performance of a heterogeneous assay is non-specific binding, when antibodies attach to substances and surfaces other than the target analyte.

In the following, we discuss the core of the time-resolved fluorescence concept, and the lanthanide labels, especially europium which is employed in the experiments.

### 2.2.1 *Time-resolved fluorimetry*

Time-resolved fluorescence techniques can be classified based on the duration of the fluorescence emission, i.e. the fluorescence lifetime of the fluorophores excited state, see Appendix A.2. In heterogeneous immunoassays, the background light includes scattering (decay time $\tau = 0$), background fluorescence from the sample and the reagent constituents (1-10 ns) and background luminescence of solid materials (plastic disposable, filters, lenses (µs-ms). In time-resolved immunoassays the fluorescence decay time should preferably to be longer than 100 µs to eliminate the most significant parts of the background. Employing the fluorophores with long fluorescence lifetime (milliseconds), belonging to the lanthanides group, high sensitivity time-resolved immunoassays can be designed, which are able to detect fluorescence emission of tens and hundreds of photons per second.

Figure 2.2 shows the principle of time-resolved fluorescence spectroscopy. The excitation pulse (blue) and the measurement event (green area) are separated in time, so that when the measurement is taking place, the scattered light and the short-lived fluorescence background have decayed. Only a

part of the total emitted fluorescence signal is collected. We therefore want to determine the efficiency of the collection.

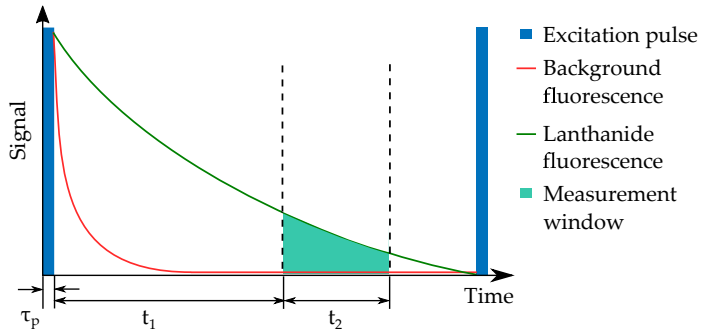


Figure 2.2: The principle of time-resolved fluorescence shown schematically: $\tau_p$ - excitation pulse width, $t_1$ - pre-delay time before the measurement, and $t_2$ - measurement window duration.

The efficiency of a time-resolved fluorescence system consists of several factors [45]:

$$E = q \cdot E_{TRF} \cdot E_O \cdot Q \tag{2.1}$$

$q$ is the quantum yield of a fluorescent label, $E_{TRF}$ is the efficiency of the time-resolved fluorescence measurement, $E_O$ is the total collection efficiency of the optical system (excitation and fluorescence), $Q$ is the quantum yield of the photodetector. The efficiency of the time-resolved fluorescence measurement $E_{TRF}$ corresponds to the part of the fluorescence exponential decay that is measured. It can be conveniently decoupled into a product of two parts: $E_{TRF} = W \cdot Y$, where $W$ depends on the pre-delay time and the measurement window duration, and $Y$ corresponds to the fluorescent signal decrease due to longer excitation pulse width compared to a delta-like excitation.

To calculate $Y$, we use a simple model. We denote the population of excited molecules, $N$ which is described by a simple rate equation:

$$\frac{dN}{dt} = R(t) - kN \tag{2.2}$$

$R(t)$ is pump rate proportional to excitation pulse peak power; $k$ is decay rate constant of the fluorophore (inverse proportional to fluorescence lifetime $\tau$). The formal solution to Eq. 2.2 is

$$N(t) = \int R(t) e^{-kt} dt \tag{2.3}$$

We assume an excitation pulse of a rectangular shape so that $R(t) = const$ when $t = [0; \tau_p]$, where $\tau_p$ is the excitation pulse duration. Then, the number of molecules, $N_0$ when the excitation pulse is switched off is:

$$N_0 = \frac{R(\tau_p)}{k}\left[1 - e^{-k \cdot \tau_p}\right] \tag{2.4}$$

Combining Eq. 2.2 and Eq. 2.4, the decay of excited molecules follows:

$$N(t) = R(t) \cdot \tau\left[1 - e^{-\frac{\tau_p}{\tau}}\right] \cdot e^{-\frac{t}{\tau}} \tag{2.5}$$

We calculate the decrease of the number of excited fluorescent molecules $Y$ due to a longer excitation pulse relative to the number of molecules $N_0^*$ when excited by very short excitation pulse $\tau_p^*$ so that $\tau_p^* \ll \tau$:

$$\begin{aligned} Y &= \frac{N_0}{N_0^*} \\ &= \frac{\tau}{\tau_p}\left[1 - e^{-\frac{\tau_p}{\tau}}\right]. \end{aligned} \tag{2.6}$$

In turn, $W$ is a function of the fluorescence decay lifetime $\tau$, the pre-delay time $t_1$ and the measurement window duration $t_2$:

$$W = e^{-\frac{t_1}{\tau}}\left[1 - e^{-\frac{t_2}{\tau}}\right]. \tag{2.7}$$

The timing parameters $t_1$, $t_2$ and $\tau_p$ are shown in Fig. 2.2.

We will later use Eq. 2.6 and 2.7 to investigate and optimize the efficiency of the time-resolved fluorescence system. Therefore, the efficiency of a time-resolved fluorescence measurement $E_{TRF}$ is

$$E_{TRF} = W \cdot Y = e^{-\frac{t_1}{\tau}}\left[1 - e^{-\frac{t_2}{\tau}}\right] \cdot \frac{\tau}{\tau_p}\left[1 - e^{-\frac{\tau_p}{\tau}}\right]. \tag{2.8}$$

In turn, the overall efficiency of the optical system is the product of: 1) the efficiency of the excitation light propagation from the light source to the sample, and 2) the efficiency of the fluorescence emission propagation from the sample to the detector:

$$E_O = \eta_{exc} \cdot \eta_{fl} \cdot I_{im}, \tag{2.9}$$

where $\eta_{exc}$ is the energy transfer efficiency of the excitation light (from the object plane to the sample plane), and $\eta_{fl}$ is the energy transfer efficiency of the fluorescence emission (from the sample plane to the detector). $I_{im}$ is the overlap factor of the excitation illumination area and the chemically active, thus fluorescent, area.

DETECTORS In immunoassay testing, measurements of extremely low concentrations are of interest [46]. This will be discussed later specifically for the measurements of cardiac markers. During the measurement time (about 10 s), only a few hundred of photons are detected. These low light levels correspond to analyte concentrations of ng/L. For comparison, the concentration of proteins in plasma is 76 g/L [47]. These proteins are sources of background interference. Therefore, detectors employed in time-resolved IAs have to be simultaneously highly sensitive at the emission wavelength of the fluorophore, and have low dark current (or dark counts) in order to detect low analyte concentrations.

Photomultiplier tubes (PMTs) have been mostly used for this application. PMTs amplify the weak fluorescence signal with a high gain ($10^6$), and contribute only slightly to the measurement due to their very low dark noise. They also have large photocathode area, which is beneficial for the fluorescence measurements from the large emitting area of samples, about 4x4 $mm^2$. The area of a PMT photocathode can be up to 24x8 $mm^2$, which is significantly larger than that of semiconductor detectors. Drawbacks of

PMTs include lower quantum efficiency in the visible range compared to solid state detectors, high required voltage, and large form factor. PMTs have high cathode sensitivity and thus offer the best option for extremely low light level measurement. Configured in a photon counting mode, PMTs are able to detect single photons.

The usage of semiconductor detectors, such as avalanche photodiodes (APDs), and silicon PMTs, has been hampered by their significantly larger dark current and smaller area compared to PMTs, despite their advantages such as high quantum efficiency and low cost.

QUENCHING AND BLEACHING Bleaching and quenching processes can impact measurements of fluorescence of biological samples significantly. Fluorescent signal can decrease either permanently or temporarily, impacting the measurement results. The effect can be especially severe in low signal conditions, when the measurement is repeated many times to improve the signal-to-noise ratio, thus with a higher excitation dose. Therefore, the bleaching and quenching processes are discussed below.

Bleaching is a photochemical reaction that causes the fluorescent signal to fade permanently when the fluorophore molecules are damaged. The exact mechanisms of the photobleaching process are not very well understood. Bleaching depends on the excitation dose applied to a fluorophore. At low excitation doses, the phenomena is not interfering. However, bleaching can be a problem with high intensity excitation, i.e. using lasers, and when continuous measurements are required. For organic fluorophores, the number of measurement cycles is therefore limited [48]. Bleaching of organometallic fluorophores, i.e. lanthanide chelates, is significantly reduced compared to organic fluorophores [10], thus preferred when possible.

In contrast, quenching is a reversible process. It is caused by noncovalent interactions between a fluorophore and its molecular environment. Often, it takes place when measuring in a solution. On the contrary, inner filter effect, or concentration quenching, can take place both in a solution or on a dried surface. It is a decrease in the quantum yield of a fluorophore after the increase of the number of fluorophore molecules per an antibody. However, this effect takes place for fluorophores with small Stokes shift.

### 2.2.2 *Lanthanide labels*

As discussed in previous section, fluorophores employed in time-resolved fluorescence measurements should have fluorescence lifetime which is significantly longer than the fast decaying background. Lanthanide based fluorophores have fluorescence lifetimes of about a millisecond, and thus constitute the basis of time-resolved fluorescence spectroscopy. Therefore, lanthanide based fluorophores are discussed below.

Lanthanides are metal ions with an electronic configuration of $4f^n$ and generally refer to elements from cerium to lutetium in the periodic table. Most lanthanide ions are fluorescent. Lanthanides' unique property is a long decay lifetime in the range of 0.5 - 3 ms. They have their 4f energy level filled and the orbitals shielded from the environment. Therefore, the emission transitions from the 4f orbital are electrically dipole forbidden, and thus the absorption coefficients are very low and the lifetimes of the excited states

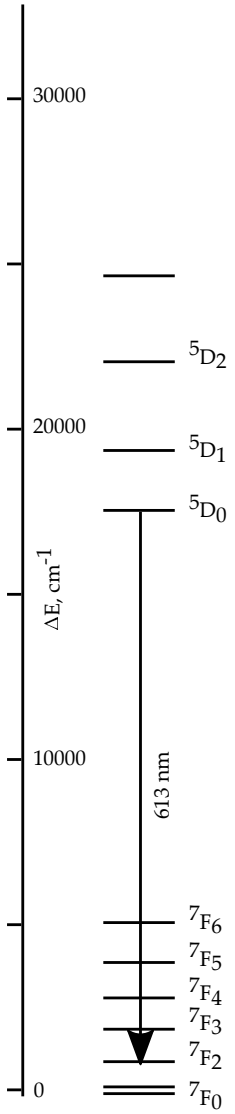


Figure 2.3: The energy levels of europium $Eu^{3+}$ ion shown schematically with the most intense transition denoted.

are long. The latter allows the use for time-resolved spectroscopy. However, due to the low absorption coefficient when excited directly, lanthanides are usually excited through chelated organic ligands, in order to improve the excitation rates. The chelated ligand absorbs an excitation photon and transfers the energy to the lanthanide ion. The excitation spectrum reflects then the excitation spectrum of the ligand used. Therefore, because the absorption and the fluorescence emission are performed by different entities: a ligand and a lanthanide ion, the resulting lanthanide chelate has large Stokes shift. The fluorescence is most intense when the metal ion has the oxidation state of 3+. Commonly used lanthanide metals include samarium(III) ($Sm^{3+}$), europium(III) ($Eu^{3+}$), terbium(III) ($Tb^{3+}$), and dysprosium(III) ($Dy^{3+}$). Large Stokes' shift, narrow emission bandwidth, sufficiently good quantum yield and the remarkably long fluorescence lifetime make lanthanide ions very good candidates for the time-resolved fluorescence techniques. The energy level diagram of an europium ion with the main emission line of transition $^5D^0$ to $^7F^2$ is shown in Fig. 2.3. The major challenges with lanthanide chelates are stability and fluorescence quenching in aqueous solutions [43].

Although the excitation wavelength depends on the chelated ligand, it has to be below 360 nm for europium and below 330 nm for terbium and dysprosium due to efficient energy transfer requirements [43]. The large Stokes' shift of lanthanides allows for easy spectral separation of the excitation and emission, and moreover prohibits self-quenching.

An excitation light source employed for the excitation of europium chelates has to emit pulses in the spectral range of 340-345 nm, with a repetition frequency low enough to match the long fluorescence lifetime and with a sufficient pulse energy.

### 2.2.3 *All-in-one dry reagent technology*

One of the challenges in point-of-care (PoC) testing is maintaining high sensitivity of measurements, while increasing the processing speed comparing to central laboratory [2]. The technique of all-in-one dry reagent technology allows for rapid automatic measurements and simultaneously high sensitivity, and is therefore discussed below.

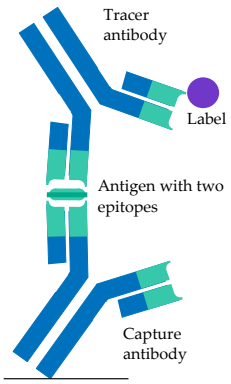


Figure 2.4: Sandwich immunoassay.

The technique of two specific antibodies in one assay is sometimes called sandwich assay and enhances the assay specificity [35]. In this case, two recognition reactions take place: between the capture antibody and one epitope of an antigen, and the tracer antibody and another epitope of the antigen. An antigen with two bound antibodies is shown in Fig. 2.4. Combined with the dry cup concept, this technique is employed in TRFIA automated measurements in PoC testing. The process is described in the following.

The test cups are produced corresponding to the all-in-one dry reagent technology [49, 50, 51]. The original empty cups are made of polystyrene. Polystyrene materials absorb UV light [52]. Analyte-specific capture and tracer antibodies are placed in the bottom of the cup and are separated and immobilized by means of an insulation layer, see Fig. 2.5. The insulation layer contains trehalose which stabilizes antibodies. The tracer antibodies are marked with a europium chelate label. The europium chelate synthesis and the labeled structure are described in [53]. The test cups are prepared for the experiments as in the following. The capture and tracer antibodies,

as well as the insulation layer which prevents contact between them during storage, are all in a ready-to-use dry format (1). The test cup is processed with a 20 µL sample solution and an assay buffer. During the incubation, the cup is incubated at 37°C for 15 minutes and shaken to reduce the reaction time (2). After the reaction, the cup is washed and the unbound tracer antibodies are washed out (3). The separation step of the bound antibodies from the unbound reagents is critical. The labeled tracer antibodies bound to the antigen are then excited by a UV light source in the measurement step (4). The fluorescence is then detected at 615 nm.

We introduce a few terms which we will later use in the experimental chapters. Hereafter, a sample cup refers to a test cup processed with a sample with a known concentration. In turn, a blank cup refers to a test cup processed with a null concentration solution.

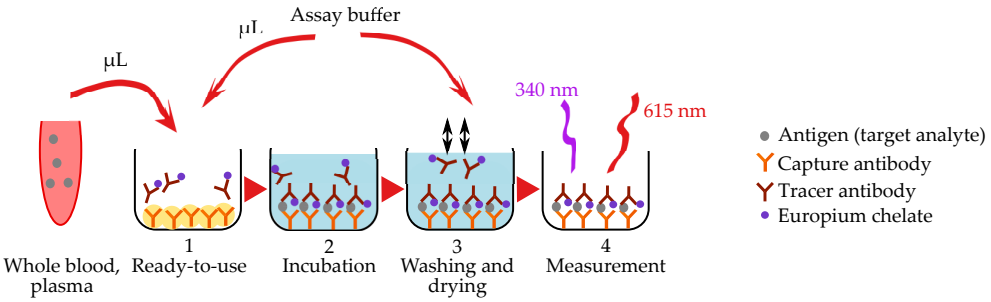


Figure 2.5: The preparation cycle of a test cup.

## 2.3 PERFORMANCE PARAMETERS

The most relevant parameters of an IA are the performance parameters, i.e. assay sensitivity and dynamic range. These are discussed below. In addition to that, the IAs employed in a PoC testing have extra requirements such as speed, i.e. short turn-around time, automated operation, ease of operation, safe waste disposal, and no manual preparation of reagents [2]. In this section, we focus only on the performance parameters which are then later employed to evaluate the impact of the novel light sources.

**SNR, S/B AND CV** The sources of background noise in a time-resolved fluorescence immunoassay include the detector dark current (or counts per second), the fluorescence from the sample and reagents, and the fluorescence from components such as optics and used cuvettes. The photon counting statistics of the instruments is described by the Poissonian model. The useful fluorescence signal $S_f$ is defined as $S_f = \overline{S} - \overline{B}_{total}$, where $S$ is the measured signal, and $B_{total}$ is the subtracted total background noise. Then, we define signal-to-noise ratio (SNR) as the useful fluorescence signal divided by the noise taking into account both the signal and background variations:

$$\mathrm{SNR} = \frac{S_f}{\sqrt{\sigma_S^2 + \sigma_{B_{total}}^2}}. \tag{2.10}$$

Since SNR is a function of an analyte concentration, it should be reported with the concentration.

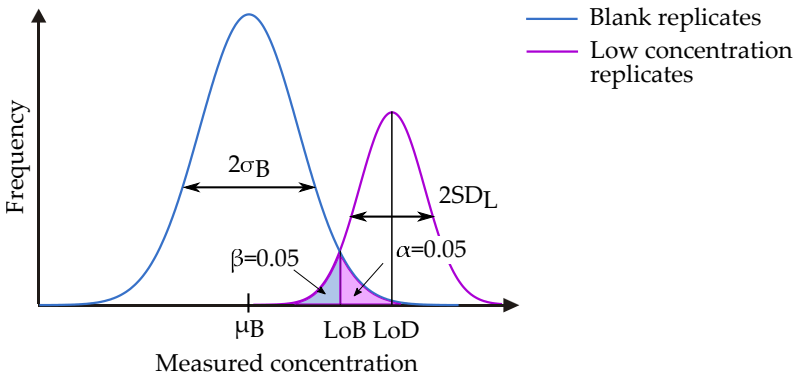


Figure 2.6: The distribution of replicates of a blank sample (blue) and a sample with low analyte concentration (purple).

Signal-to-background ratio (S/B) is defined as the relation of the useful fluorescence signal $S_f$ and the background noise:

$$S/B = \frac{S_f}{B_{total}}. \tag{2.11}$$

Thus, the SNR is Eq. 2.10 takes into account the noise fluctuations, while the S/B in Eq. 2.11 takes into account only the absolute value of the background noise.

The second important parameter is the coefficient of variation (CV). Generally, CV of a set of measurements is defined as a relation of a standard deviation $\sigma$ of this set of measured values to its mean value $\mu$. Through this report, the variation of measured signal and background is denoted as $CV_i$:

$$CV_i = \frac{\sigma_i}{\mu_i} \tag{2.12}$$

with $i$ is either S, for measured signal, or B, for measured background noise. At the same time, the CV as an assay performance parameter calculated for a given concentration is denoted $CV_C$. $CV_C$ is defined as: $CV_C = \frac{\sigma_S}{S_f}$. A plot showing $CV_C$ of replicate measurements for different concentrations is referred to as the *precision profile*, see Fig. 2.7. The precision profile is one of the most relevant characteristics of an assay and shows the measurement accuracy as a function of concentration.

LOB, LOD, LOQ The most relevant analytical parameters in immunoassays are limit of blank (LoB), limit of detection (LoD), and limit of quantification (LoQ). In simple terms, these parameters can be thought of as follows. LoB is the highest measurement result that is likely to be observed on a blank sample. LoD is the lowest analyte concentration that can be statistically distinguished from blank. LoQ is the lowest concentration that can be reliably quantified with a pre-defined accuracy.

There are many ways in literature to define these parameters accurately. In this report, the definitions given in Clinical and Laboratory Standards Institute (CLSI) guidelines are used [54]. The definitions of LoB and LoD are shown in Fig. 2.6. LoB is defined relative to the distribution of blank sample replicates, so that only $\alpha$ of the distribution exceed the LoB. For LoD, the

probability of falsely claiming the absence of an analyte is $\beta$, and the probability of falsely claiming its presence is $\alpha$. In other words, $\alpha$ is the probability of a false-positive result and $\beta$ is the probability of a false-negative result. They are also referred to as Type I and Type II error, respectively. Nominal values for $\alpha$ and $\beta$ are 5% [54]. 95% ($\alpha$ is 5%) of the blank sample replicates (blue curve) are below the LoB. For the sample with a concentration equal to LoD, 95% ($\beta$ is 5%) of the replicates (purple curve) are above the LoB.

At this point we introduce the limit of quantification as the lowest concentration $C^*$ that can be measured with a defined coefficient of variation $CV_0$, see Fig. 2.7:

$$LOQ = C^*(CV_C = CV_0) \tag{2.13}$$

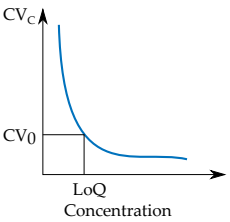


Figure 2.7: Precision profile of an assay with the limit of quantification shown.

In this work, the LoB and LoD are calculated using the parametric approach [54]. The LoB is calculated with blank cups processed with a null concentration sample as:

$$LoB = \mu_B + c_p \cdot \sigma_B \tag{2.14}$$

$\mu_B$ and $\sigma_B$ are the average value and the standard deviation of the measured blank cups, respectively; $c_p$ is a multiplier for the 95th percentile of the normal distribution of the blank samples, see Fig. 2.6 and is calculated as:

$$c_p = \frac{1.645}{1 - \frac{1}{4(B-K)}} \tag{2.15}$$

where B is the number of blank cups replicates measured (of all blank samples in total), and K is the number of blank samples used in the experiment (number of subsets of blank cups).

The LoD is calculated from LoB according to:

$$LoD = LoB + c_p \cdot SD_L \tag{2.16}$$

with $c_p$ used as a multiplication factor which is now calculated for low concentration samples:

$$c_p = \frac{1.645}{1 - \frac{1}{4(L-J)}} \tag{2.17}$$

$SD_L$ is a pooled standard deviation for all low concentration samples:

$$SD_L = \sqrt{\frac{\sum_{i=1}^{J}(n_i - 1)\sigma_i^2}{\sum_{i=1}^{J}(n_i - 1)}} \tag{2.18}$$

where L is the total number of low concentration sample results, i.e. the total number of replicates of all concentrations used in the calculation. J is the number of the low concentration samples used in the experiment, $n_i$ is the number of results for i-th low concentration sample, and $\sigma_i$ is the standard deviation of the distribution of replicates of i-th low concentration sample. The LoQs are calculated by fitting a power fit function to the precision profile (CV vs. concentration curve) shown in Fig. 2.7.

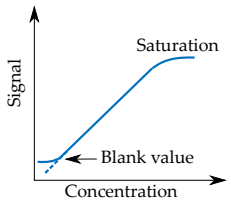


Figure 2.8: Response curve of an assay.

The background and noise sources in an immunoassay detection system determine the measurement performance, i.e. LoB and LoD. The background value measured with blank cups, i.e. LoB, determines the lower limit of a response curve of the assay, shown in Fig. 2.8. Thorough discussion of the background and noise of an IA is given in Section 4.6. The upper limit of the response curve can be determined by the detector nonlinearity, fluorophore saturation and high-dose hook effect [55].

## 2.4 ANALYTES

Time-resolved fluorescence immunoassays target disease-specific protein markers. Examples of different analytes currently available for PoC immunoassay testing include cardiac markers (troponins, myoglobin, CK-MB), infection markers (CRP, PCT), thrombosis markers (D-dimer), hormones (hCG), and diabetics markers (glycated hemoglobin). In this study, the developed systems are tested on a cardiac troponin marker which is described below.

### 2.4.1 *Cardiac troponins*

Cardiovascular diseases (CVDs) are a major cause of human death in the world [56]. CVDs are a class of several diseases, including acute myocardial infarction (AMI). For patients with suspected AMI, the early diagnosis is critical as the mortality risk is strongly connected to time until treatment. The mortality rate is 1% when treatment is implemented within one hour after the acute event and 10-12% within first 6 hours [57]. The AMI symptoms are often non-specific, such as chest pain. Therefore, the measurement and monitoring of cardiac markers is critical for the diagnosis and rule-out.

Cardiac troponin (cTn) is the preferred biomarker for aid in the diagnosis of AMI [58]. A troponin protein complex consists of troponin I, troponin T and troponin C, where the first two exist in cardiac-specific forms and these are widely used for the AMI diagnosis. The recommended decision limit for the myocardial injury is the $99^{th}$ percentile of the healthy reference population, as shown in Fig. 2.9. However, troponin levels often do not reach the detection limit of standard troponin assays until about 6 hours after the acute event. Moreover, recent studies suggest that the troponin values in healthy individuals are sex and age dependent [59, 60, 61, 62]. Determining the biological variation has not been possible with contemporary cTn assays because the assays cannot reliably measure and quantify the cTn concentrations of a healthy population. Most of the assays only detect measurable values in <15% of healthy individuals [46]. The measurement of troponin variations in healthy populations will allow for the adjustment of the $99^{th}$ percentile values, which in turn will assist to determine accurate decision limits. This will help in the clinical interpretation of the results leading to earlier and improved diagnosis and rule-out of AMI [46, 63, 64, 65].

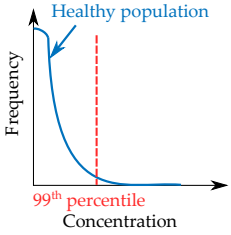


Figure 2.9: The $99^{th}$ percentile: 99% of the healthy population have troponin level below this value.

For these reasons there has been a need for the development of a high-sensitivity troponin (hsTn) assay [63, 66]. However, the lack of standardization of troponin I is a known issue. Therefore, the detection limits of two different platforms cannot be compared on an absolute scale. Instead, relative numbers, such as the $99^{th}$ percentile value (and $CV_C$ at this value)

and its relation to the detection limits can be compared to evaluate assays. Recently, as high-sensitivity assays are being developed, the percent of the detection of the healthy population is also used for comparison. A manufacturer of an assay provides its own upper reference limit (the $99^{th}$ value) and the analytical parameters. With this in mind, two criteria for hsTn (can be troponin I or T) assays are defined [46]:

1. The CV at the $99^{th}$ percentile value has to be smaller than or equal to 10%.

2. The troponin values of at least 50% (ideally >95%) of the healthy population have to be measurable, i.e. above the LoD.

Contemporary cTn assays do not satisfy these criteria [46]. Recently, Abbott [62, 46, 64, 66], Siemens Healthcare Diagnostics [59] and Roche [61, 46, 65] have been developing assays which potentially meet these hsTn assay criteria. However, these assays are only intended for laboratory use.

In this study, we use both standard and recently developed high-sensitivity troponin assays to test the developed systems. We will demonstrate that with the developed point-of-care system we potentially fulfill the hsTn criteria, thus move towards earlier diagnosis and rule-out with the designed system combined with the high-sensitivity assay.

# 3 LED BASED TIME-RESOLVED FLUORESCENCE SYSTEM

This and the following chapter are based on the developed light emitting diode (LED) based fluorescence time-resolved system. The objective was to develop an LED based optical unit for the Radiometer AQT90 immunoassay (IA) analyzer. Besides the performance requirements, the mechanical requirements dictated that the developed system has to be compatible with the IA analyzer. Moreover, the new excitation system has to fit into the currently used Xenon flash lamp based system. The designed LED based optical system is compared against the currently used flash lamp based system. In order to compare the impact of the light sources only, the detection optical system remained unchanged. With these mechanical requirements in mind, we design the system for maximum excitation light efficiency.

## 3.1 SETUP AND OPTICAL DESIGN

ETENDUE Etendue $d^2G$ of a light source corresponds to a volume (or an area in 2D) in phase space and is defined as:

$$d^2G = n^2 dS \cos\theta d\Omega \tag{3.1}$$

where $n$ is medium refractive index, $dS$ is a unit emission area, $\theta$ is a projection angle, and $d\Omega$ is a unit emission solid angle. We express the solid angle in spherical coordinates and assume the etendue being uniform over the solid angle. Then, one obtains:

$$dG = n^2 dS \int \cos\theta d\Omega = n^2 dS \iint \cos\theta \sin\theta d\theta d\phi = \pi n^2 dS \sin^2\alpha \tag{3.2}$$

$\alpha$ is the 2D emission half-angle. Under the assumption that the source S distribution is uniform, and assuming that every small unit area radiates in the same angle cone, we can integrate over all area and obtain:

$$G = \pi n^2 S \cdot NA^2. \tag{3.3}$$

In an ideal optical system, etendue is conserved. An etendue of a light beam can never decrease as it passes through an optical system. It is the optical equivalent of the entropy as defined in the second law of thermodynamics. The etendue conservation corresponds to the Abbe sine condition in nonparaxial notation, and to the Lagrange invariant in paraxial notation. An etendue of an optical system is limited by the optical component with the smallest etendue. In our excitation system, that component is the test cup. The test cup is shown in Fig. 3.1 and measures 6.7 mm in diameter and 10.7 mm in height. The acceptance half-angle is 17.4° and the solid angle is 0.29 sr. Relative to the full sphere $4\pi$ it is 2.3%. Thus, the etendue of the cup is 9.9 $mm^2 \cdot$ sr. However, the fluorescence system collection efficiency has to be taken into account. The first lens in the emission light path accepts a light

Figure 3.1: Drawing of a test cup.

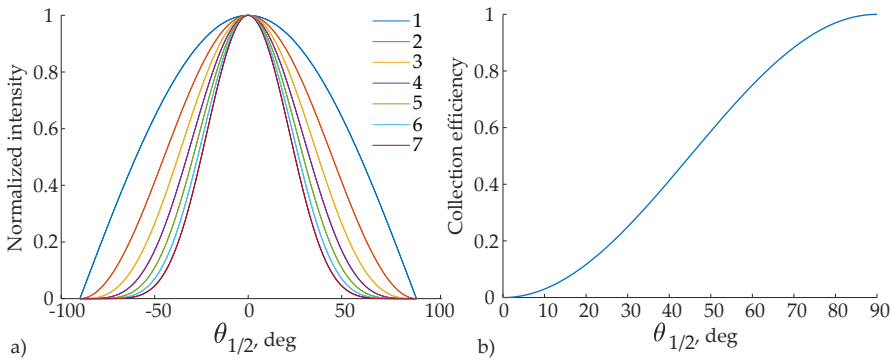


Figure 3.2: a) Angle distribution of a Lambertian light source of different orders (1-7); b) collection efficiency from a first order Lambertian light source as a function of half-angle.

cone with the half-angle of 12.1°. The field of view (FOV) of the detector is area of 5 mm in diameter. Therefore, the image plane etendue is only 2.7 $mm^2 \cdot$ sr.

A single emitter LED is a first order Lambertian light source and emits in the full hemisphere of $2\pi$. Figure 3.2(a) shows the normalized intensity of a Lambertian light source of different orders (1-7) as a function of emission half-angle. For the first order Lambertian source, the light intensity drops by 50% at the half-angle of 60°. The higher the order, the narrower the angular spectrum is. It is rather difficult to collect light from an LED efficiently. Figure 3.2(b) shows collection efficiency from a first order Lambertian source as a function of collection half-angle. At the angle of 45°, which corresponds to a rather high numerical aperture (NA) of 0.7, 50% of the emitted light is collected. The options like coupling to an optical fiber are not preferred due to resulting low efficiency. Assuming the emitting angle to be 60°, a single emitter LED with the dimensions of 1x1 $mm^2$ has the etendue of 2.4 $mm^2 \cdot$sr, which is smaller than the image plane etendue (2.7 $mm^2 \cdot$ sr). Thus, theoretically it is possible to focus all the LED light at the bottom of the test cup.

Two optical systems were developed with two different image magnifications. The magnification of the first system is $-5$, i.e. the maximum magnification dictated by the FOV of the detector. The second system is designed with a smaller magnification of $-4$. Hereafter, we refer to the systems as *system 1* and *system 2*.

The first designed optical system, *system 1* is shown in Fig. 3.3. The excitation light is collected from a Lambertian emitter with an area of 1x1 $mm^2$ (SMD LED YL-6363F-340nM manufactured by Seoul Vyosys Co., Ltd) by an aspheric lens with a short focal length and high NA. The next two plano-convex lenses and a biconvex lens form an image 50 mm away. All lenses are made of UV grade fused silica to ensure high transmission in the UV-A region and to minimize autofluorescence from the lens material. The image is formed in the bottom of the UV absorbing test cup which is made of polystyrene. The excitation system is designed for maximum collection efficiency reaching 80%. If smaller magnification is needed, the first lens, $f_1$ needs to have a larger focal length and thus smaller object side NA, or alternatively, the last lens, $f_4$ needs to have shorter focal length, thus larger image side NA. The first option reduces the collection efficiency. The second

option is not feasible due to the limited acceptance angle of the test cup and the mechanical requirement of a minimum distance between beam splitter and test cup, imposed by the mechanical design of AQT90 system. Thus, there is a trade-off between the magnification and collection efficiency when selecting the first lens, $f_1$. A diffuse reflector is placed under the test cup in order to increase the fluorescence collection efficiency. The reflector is modeled as a flat Lambertian reflector. A dichroic beam splitter separates the excitation and detection light paths. The emitted fluorescence is collected by two aspheric PMMA lenses and focused on a photocathode of a photomultiplier tube (PMT) with a magnification of $-1$. The PMT has a photocathode effective area of 8x24 $mm^2$ and is configured for a photon counting mode. Two bandpass filters in the excitation and detection systems ensure that only emitted fluorescence at 615 nm reaches the PMT. The reference photodiode is used to monitor the light source power.

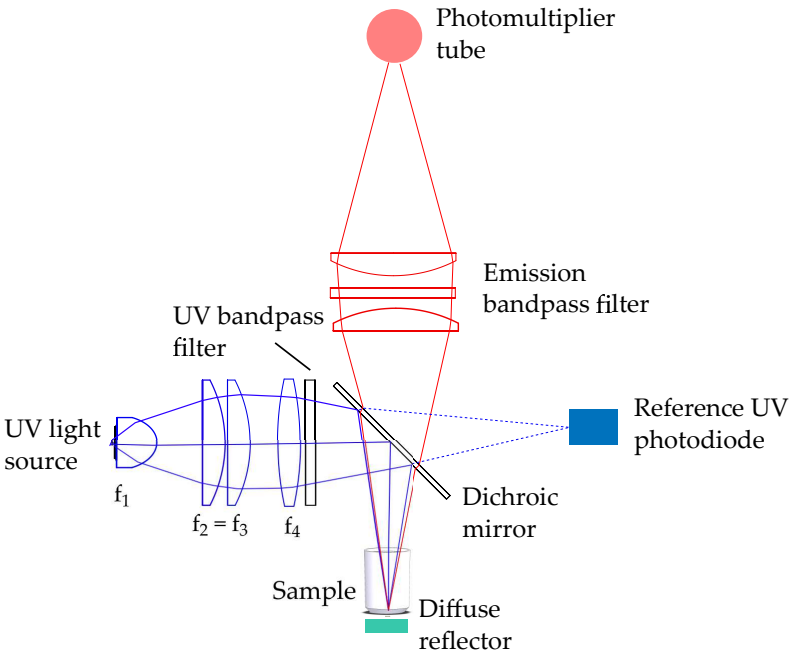


Figure 3.3: Schematic layout of the optical system (*system 1*) with the excitation and detection light paths.

Using commercial ray tracing software the image of the light source was modeled. The image is a square with 90% of the power encircled in a 5x5 $mm^2$ area, see Fig. 3.4(a). The obtained experimental image was in a good agreement with the model, as shown in Fig. 3.4(b). The low-intensity decaying edges are not observed experimentally due to limited dynamic range of the camera used. The LED image covers 71% of cup bottom area, which is three times larger than the flash lamp image. The exploited illumination area is limited by the PMT photocathode area and its FOV. The calculated FOV corresponds to a 5 mm diameter circle at the bottom of the cup, thus using a larger LED emitting area is not an advantage.

It will be shown later that the *system 1* is not optimal for the fluorescence measurements due to poor overlap between the illumination area and the fluorescent area. Therefore, a system with smaller magnification, *system 2* is designed.

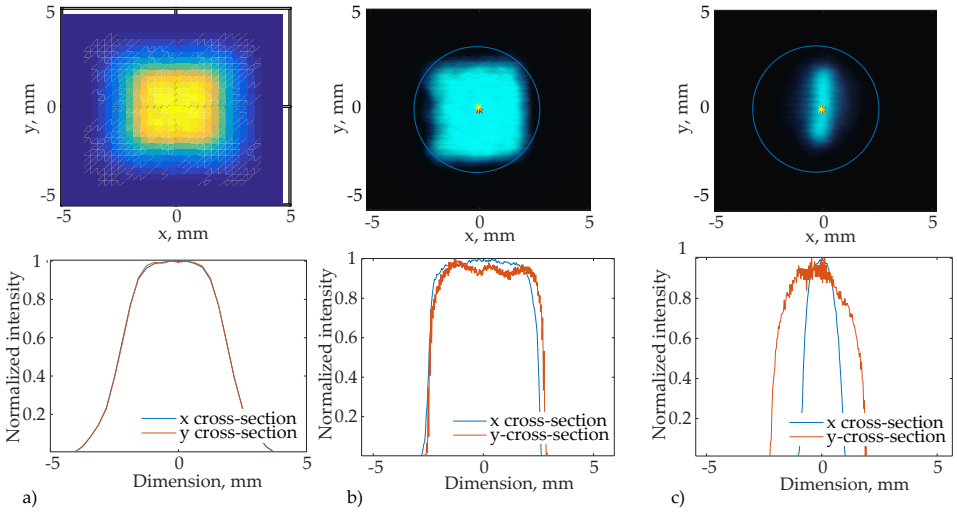


Figure 3.4: Images formed in the test cup and its normalized intensity distribution in *system 1*, a) modeled LED image using commercial ray trace software; b) experimentally obtained LED image; the blue circle shows the boundary of cup bottom which is 6.7 mm in diameter; c) image of flash lamp arc (current light source). The illuminated area is 2x4 $mm^2$, thus three times smaller than that of the LED image.

In *system 2*, the formed image is 4x4 $mm^2$ in size and takes up 45% of cup bottom area, as shown in Fig. 3.5. The design of the excitation optics was modified to obtain smaller magnification at the cost of less collected light compared to *system 1*. The detection optical path remains unchanged.

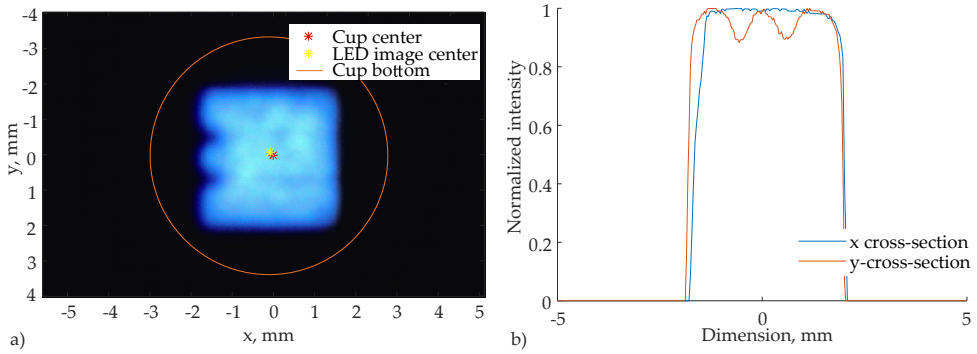


Figure 3.5: a) Experimentally obtained LED image in *system 2*; the image is 4x4 $mm^2$ and takes up 45% of the cup area. b) Normalized intensity distribution of the LED image.

The connection diagram of the fluorescence measurement system is shown in Fig. 3.6. The LED is controlled by an LED driver, which is synchronized with the detection system. An FPGA controls both the excitation and detection systems using a trigger pulse train, which is transmitted to the LED driver via a pulse generator, and at the same time to the PMT PCB. The FPGA is a part of the main board (MB). The inlet PCB and the flash driver are used with a flash lamp based system. The MB, inlet PCB, flash driver, and AQT power supply are all parts of an analyzer.

The LED based optical units (OUs) are compatible with the flash lamp based immunoassay analyzers and can be integrated for automated measurements in a standard point-of-care (PoC) environment. The excitation

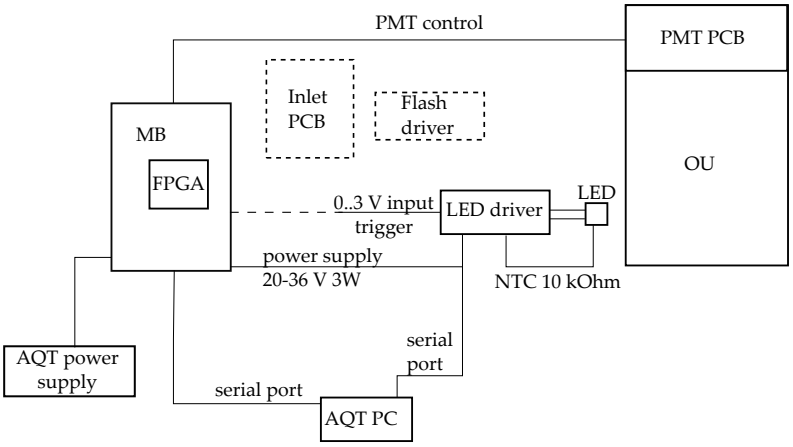


Figure 3.6: Electric diagram of the LED based optical unit (OU). MB - main board; PMT - photomultiplier tube.

energy of the LED based instruments is equal to that of the flash lamp based instruments.

FLASH LAMP BASED SYSTEM The currently used flash lamp system employs the Xenon flash lamp L9455 from Hamamatsu with an average power output of 5 W in the emission spectral range of 185-2000 nm. It delivers from 8.8 to 19.8 mJ per pulse depending on discharge voltage. However, due to mostly spectral, but also spatial filtering only about 5.1 µJ is delivered to the test cup. Out of the broadband spectrum, only 48 nm are spectrally selected for the sample excitation. The Xenon flash lamp used in the current optical system has a lamp arc length of 1.5 mm. It is imaged with a magnification of $-2$ in the sample cup, see Fig. 3.4(c). The repetition rate can be varied in the range of 250-530 Hz. In the system, the flash lamp is triggered by the FPGA with a repetition frequency of 250 Hz. The object side NA is smaller (<0.5) compared to that of the UV LED, thus the collection efficiency is smaller due to vignetting. The flash lamp was modeled as a Lambertian emitter that measures 0.75x1.5 $mm^2$ in size, corresponding to the arc size, and emitting as the $4^{th}$ order Lambertian source, see Fig. 3.2(a). The optical excitation efficiency is 0.4. Therefore, combined with the spectral filtering the overall efficiency is much smaller for the flash lamp, about 0.02.

## 3.2 CHARACTERIZATION OF THE LED BASED OU

The LED emission spectrum is centered at 343 nm with a FWHM of 10 nm, as shown in Fig. 3.7(a). Filters WG320 and Schott DUG11 transmit a window with a FWHM of 48 nm of the flash lamp emission spectrum. When increasing the LED current from 100 mA to 1 A in pulsed mode, no visual shift in peak wavelength was observed, see Fig. 3.7(b). Similar results were also reported in [23], thus indicating that UV LEDs are spectrally stable. The inset figure shows the normalized LED irradiance in a logarithmic scale. The light emission drops fast to 1% and 0.1% of the peak emission at 372 nm and 404 nm, respectively.

In continuous wave (CW) operation, the LED emits up to 55 mW at the specification current of 500 mA. The LED pulse width of 200 µs is chosen

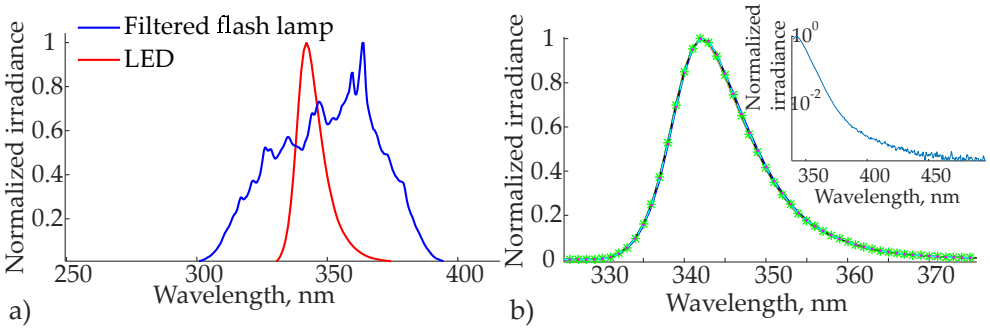


Figure 3.7: a) Normalized emission spectra of the LED (red) and the filtered flash lamp (blue); b) normalized emission spectra of the LED for different LED currents ranging from 100 mA to 1 A (curves overlap); inset figure: normalized irradiance of the LED in a logarithmic scale.

in order to deliver the same excitation energy as the flash lamp (5.1 µJ) and to obtain a good signal-to-noise-ratio (SNR) of the instrument without overdriving the LED. The LED is capable of delivering up to 15 µJ at a current of 1.5 A, which is still only three times above the maximum continuous wave current as specified with the dotted line in Fig. 3.8.

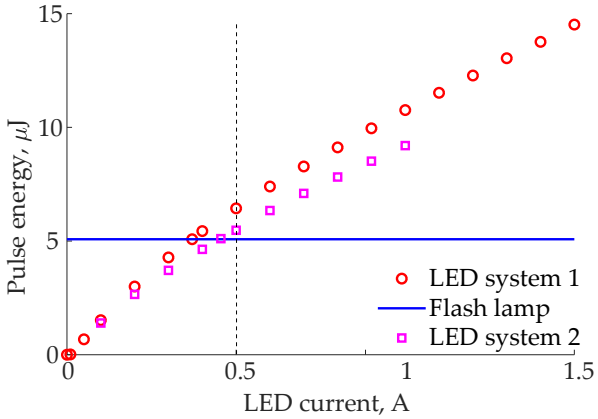


Figure 3.8: Excitation pulse energy delivered to the cup vs. LED current. The pulse width is 200 µs and the duty cycle is 0.05. *System 1* (red circles): at the current of 370 mA, the delivered energy is equal to that of the currently used Xenon flash lamp. Energy levels up to 15 µJ are achieved when overdriving the LED three times above the specified maximum current of 500 mA (indicated by the dotted line). *System 2* (magenta squares): at the current of 455 mA, the delivered energy is equal to that of the currently used Xenon flash lamp.

Figure 3.9(a) shows the LED current pulse (magenta) and the optical pulse (light green), triggered by the FPGA pulse (dark blue) through the pulse generator (light blue). The flash lamp pulse width is 200 ns, shown in Fig. 3.9(b) and exhibits a long fall time of 400 ns (90% - 10%) relatively to its width. The LED pulse width is about three orders of magnitudes longer than the flash lamp pulse. The LED pulse width can be longer, thus increasing the excitation energy and improving the SNR, as long as the pulse terminates before the measurement. A delay of 8 µs between the trigger pulse and the LED current pulse is observed and the fall time of the LED pulse is smaller than 3 µs.

In the following, we discuss the efficiency of the LED based time-resolved fluorescence system as described in Eq. 2.1 in Section 2.2. The quantum yield of the employed europium chelate is 0.13 [53]. The PMTs quantum yield is 0.04 (R4220 at 615 nm). The efficiencies of the excitation light paths are 0.8 and 0.5 for *system 1* and *system 2*, respectively. The efficiency of the fluorescence optical path is 0.01, modeled for the UV illumination area of 4x4 $mm^2$. The overlap factor is theoretically unknown. One of the goals of the experiment is to estimate its value. Assuming the factor to be 1, $E_O$ is 0.008 and 0.005 for the two systems, respectively.

We have chosen the pre-delay time, $t_1$ of 400 µs between the end of the excitation pulse and the measurement window in order to match a typical timing parameter used in the flash lamp excitation system. In the flash lamp excitation system, this parameter is required due to the flash lamp afterglow which was reported to last for hundreds of microseconds after the emission pulse [14]. This parameter can be optimized in the LED based excitation system. Reduced gate delay will increase the signal and improve the SNR, in contrast to the flash lamp based system. For a typical decay time $\tau$ of 1 ms, and both $t_1$ and $t_2$ of 400 µs, the measured part of the fluorescence decay $W$ is 0.22.

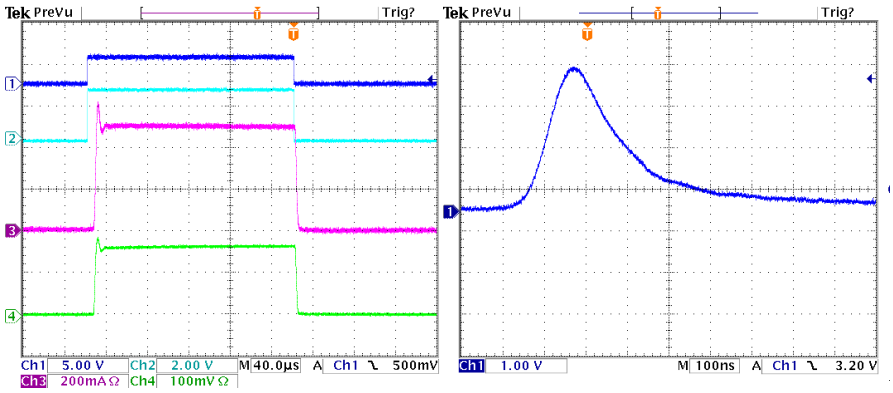


a) b)

Figure 3.9: a) The time response of the LED pulse triggering system; trigger pulse from the FPGA (dark blue); pulse generator (light blue); LED current pulse (magenta); and optical output (light green). The delay between the LED current pulse and the trigger is 8 µs and the LED fall time is below 3 µs. b) The Xenon flash lamp pulse showing a FWHM of 200 ns and a fall time of 400 ns.

In the following, we assess the factor $Y$, defined in Eq. 2.6, which reflects the fluorescence signal decrease due to the longer LED excitation pulse width. The much longer LED pulse affects the excitation efficiency of europium chelates, but only slightly as discussed below. The LED pulse width is comparable to the fluorescence lifetime, whereas the flash lamp pulse is in the range of hundreds of nanoseconds. Therefore, the number of the fluorophore excited molecules at the end of the pulse, $N_0$ is smaller in the first case. Figure 3.10(a) shows the number of excited molecules, N when illuminated by an excitation pulse of 200 ns and 200 µs respectively (blue and orange curve). N builds up exponentially during the pulse proportional to the excitation peak power, reaches the value $N_0$ at the end of the pulse, and then decays exponentially with the lifetime, $\tau$ when the pulse is switched off. This curve can also be obtained as the convolution of the excitation

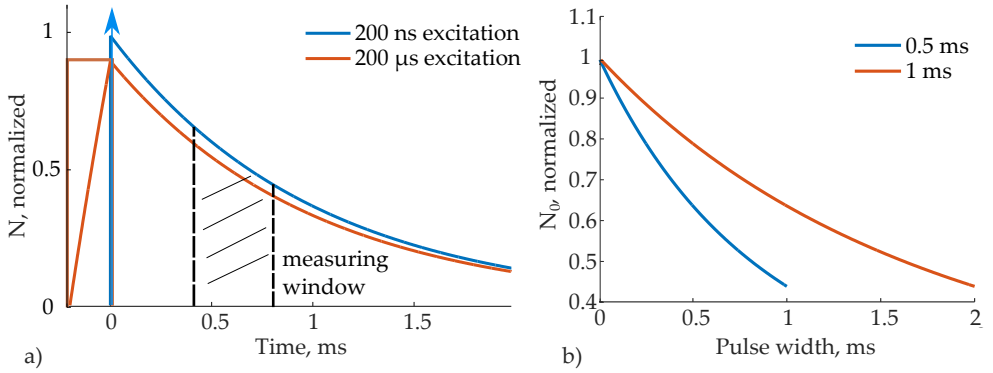


Figure 3.10: a) Excitation pulse and number of excited molecules, N for a LED pulse of 200 µs (orange curve) and a 200 ns flash lamp pulse (blue curve); during the excitation pulse the number of excited molecules builds up exponentially and reaches the maximum value by the end of the pulse; then it decays exponentially with the decay rate constant, k, related to the europium chelate lifetime of 1 ms. The number of excited molecules is 10% smaller for the longer excitation pulse. b) The number of excited molecules, $N_0$ vs. excitation pulse width with a constant total energy plotted for two different fluorophore lifetimes.

pulse and the fluorescence decay. The factor Y is equal to the number of molecules by the end of the pulse, $N_0$, normalized to that when excited by a very short pulse (see Eq. 2.4 and 2.6). Thus, Fig. 3.10(b) also shows the factor Y as a function of the excitation pulse width.

The main conclusion is that the difference of three orders of magnitude in pulse widths only gives rise to a 9% decrease in the number of excited molecules, thus in the fluorescence signal, as shown in Fig. 3.10(b). Thus, Y is 0.91 and $E_{TRF}$ is 0.20. Overall efficiency E is $8{\cdot}10^{-5}$ and $5{\cdot}10^{-5}$ for *system 1* and *system 2*, respectively.

## 3.3 CONCLUSION

Two LED based optical systems were designed for maximum excitation collection efficiency with the mechanical limitations dictated by the Radiometers AQT90 analyzer. The first optical system was designed to collect up to 80% of LED light, emitted from the 1x1mm$^2$ Lambertian chip and simultaneously be focused to an area of 5x5 mm$^2$ in the bottom of a test cup with a 6.7 mm diameter. The image area was three times larger than the image of the Xenon flash lamp, however still small enough to excite fluorescence efficiently and subsequently be imaged on the PMT photocathode. The LED was operated at 370 mA in pulsed mode. It was later concluded that an illumination area of 5x5 mm$^2$ was not optimal in this system. In the following chapter, we will discuss the impact of the illumination area on the fluorescence signal. The second system with a smaller magnification was designed, which collected up to 50% of LED light, with an illumination area of 4x4 mm$^2$ in the bottom of the test cup. The LED current is then 455 mA and still below the specified maximum current.

Spectral, temporal and spatial parameters of the LED based systems were investigated. The LED pulse width was 200 µs and the pulse energy was 5.1 µJ when operated below the specified maximum current limit, equal to

the pulse energy from the Xenon flash lamp. A three orders of magnitude increase in pulse width of the LED excitation compared to the flash lamp was estimated to reduce the fluorescence signal by a mere 9% due to the long fluorescence lifetime of europium. The efficiencies of time-resolved detection were discussed.

# 4

# TROPONIN MEASUREMENT BY LED BASED ANALYZER

In this chapter, the developed LED based systems, both *system 1* and *system 2*, are tested for the measurements of cardiac marker troponin I, discussed in Section 2.4. The systems are first tested on a test bench setup, so that cup-to-cup variation is eliminated. Then, fully automated, LED based immunoassay analyzers are built and tested for troponin I measurement. In the following, we aim to perform a comparative study of the currently employed flash lamp excitation, and the novel LED excitation. In addition, we investigate the impact of the LED excitation on the most relevant analytical parameters of immunoassays and perform an optimization analysis of the time-resolved fluorescence measurements. We suggest a model describing the background noise sources in a time-resolved fluoroimmunoassay system.

## 4.1 ASSAYS AND CHEMISTRY

In the following, the samples employed for the troponin I measurement are described. The test cups are prepared at Radiometers daughter company, Radiometer Turku, according to the all-in-one dry cup technology [49] with the europium chelate as a fluorescence marker. The assays used in the experiments are described below.

- Assay 1: the standard troponin I (TnI) assay of Radiometer AQT90 FLEX [67, 68]. It is used to determine the improvement of signal-to-noise ratio (SNR) and limit of detection (LoD) obtained by the light emitting diode (LED) excitation source compared to the standard flash lamp based system.
- Assay 2: a high-sensitivity TnI (hsTnI) research assay [69] utilizing three biotinylated capture antibodies and one europium-labeled tracer antibody.
- Assay 3: an hsTnI research assay used in the optimization study is similar to assay 2 but with two tracer antibodies binding to separate epitopes on the TnI molecule.

The research hsTnI assays 2 and 3 have been developed with the standard TnI assay (assay 1) as a starting point by modifying the chemical components in order to increase analytical sensitivity. The research hsTnI assays are also based on the all-in-one dry cup technology. All assays are developed at Radiometer Turku.

The main parameters of the assays are shown in Table 4.1, data from [69]. The emission spectrum peak of all assays is at 615 nm as shown in Fig. 4.1. The europium chelate used for the tracer antibody in the standard TnI assay (assay 1) has an excitation peak at 325 nm with a FWHM of 64 nm, shown in Fig. 4.2, yellow. The chelate structure and synthesis are described in [53]. Both hsTnI assays (assay 2 and 3) have their excitation peak at 345 nm, as shown in Fig. 4.2, green. The LED emission spectrum has approximately

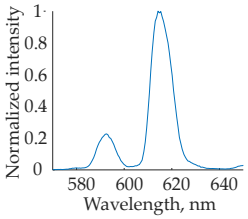


Figure 4.1: The emission spectrum of europium chelate, measured at Radiometer Turku. The emission peak is at 615 nm.

20% larger overlap with the assay 1 excitation spectrum than the filtered flash lamp. The hsTnI assays have 73% and 28% better spectral overlap (calculated using the emission spectra normalized to have equal area under the spectral curve) with the LED and the filtered flash lamp emission spectra, respectively, compared to the standard TnI assay. For both standard and high-sensitivity TnI assays the LED excitation is more optimal compared to the filtered flash lamp. Calculated spectral overlap for the filtered flash lamp and the LED excitation is shown in Table 4.2.

Table 4.1: Absorption maxima ($\lambda_{abs}$) and excitation maxima ($\lambda_{exc}$), luminescence decay times ($\tau$), molar absorption coefficients ($\epsilon$), brightness ($\epsilon\Phi$) and quantum yields ($\Phi$) as the enhanced brightness on dried surface. Data from [69] with permission.

| Assay | $\lambda_{abs}$, nm | $\lambda_{exc}$, nm | $\tau$, ms | $\epsilon$, $M^{-1}cm-1$ | $\epsilon\Phi$, $M^{-1}cm-1$ | $\Phi$, % |
|---|---|---|---|---|---|---|
| 1 | 325 | 325 | 1.01 | 55000 | 8000 | 9 |
| 2&3 | 344 | 340 | 0.97 | 55000 | 16100 | 10 |

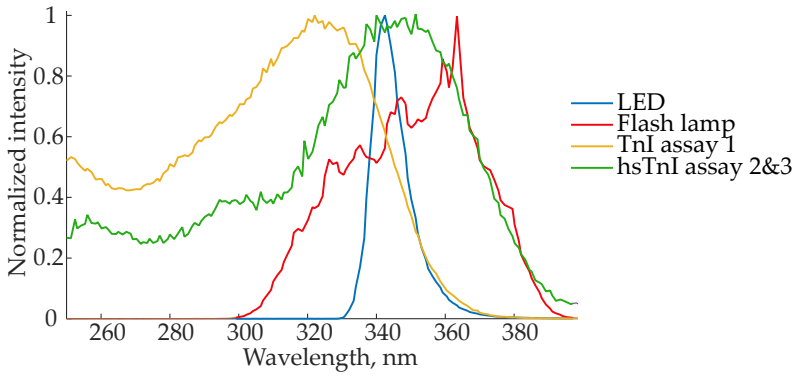


Figure 4.2: Normalized emission spectra of the LED (blue), filtered flash lamp (red) and normalized excitation spectra of the standard TnI (yellow) and the research high-sensitivity TnI assays (green).

Table 4.2: Normalized spectral overlap between the emission spectra of the light sources and the excitation spectra of the assays.

| Excitation | Assay 1 | Assays 2&3 |
|---|---|---|
| Filtered flash lamp | 0.46 | 0.78 |
| LED | 0.58 | 1 |

Test samples used in the experiments can be based on either tris-saline-azide buffer containing bovine serum albumin (BSA-TSA), LQC, whole blood (WB), or serum. An LQC is a solution of spiked serum. The samples based on BSA-TSA consist of ternary troponin ITC complex (produced by HyTest) and troponin complex (by BBI Solutions) diluted in BSA-TSA. In WB samples, the fluorescence signal is lower proposedly because blood constituents are quenching the signal.

## 4.2 MEASUREMENT ON THE STANDARD TNI ASSAY 1 WITH THE LED BASED SYSTEM 1

The LED based system is tested for time-resolved fluorescence measurements of the cardiac marker, TnI on the standard TnI assay (assay 1). The employed LED system is *system 1*. The measurements are performed on a test bench, not on the Radiometer analyzer. The LED based system is compared to a flash lamp based system. The sensitivity of the standalone flash lamp system was adjusted before the experiment to a known europium standard. In turn, the LED current of the LED based optical unit (OU) was adjusted to deliver the same excitation energy per pulse as the flash lamp unit. The experiment with the test cups was performed manually. Each test cup was measured consequently on the flash lamp unit and the LED unit without rotation (in the same cup holder). The samples used in these experiments are LQC. Fifteen sample cups (with 200 ng/L), and fifteen blank cups (0 ng/L) were produced for the experiment with the standard TnI assay.

Table 4.3 shows the parameters of the light sources as well as the statistical data of the measurements. Samples were exposed to 777 pulses with a pulse energy of 5.1 µJ each using a repetition frequency of 250 Hz corresponding to 1.27 mW average power. The measurements were performed without bleaching effects due to the small exposed energy. The average counts are listed with confidence intervals for the sample mean value which are calculated from the t-parameter Student's distribution, corresponding to a 95% confidence level. The sample standard deviations σ are given with confidence intervals calculated from the $\xi^2$ distribution [70]. For a confidence level of 95% and 15 samples, standard deviation confidence intervals (CI) are [0.73·σ; 1.58·σ]. Figure 4.3 presents the data for a total of 30 cups (15 sample and 15 blank cups).

Table 4.3: Parameters of the excitation light sources and statistical data presented for the sample concentration of 200 ng/L and blank cups (null concentration) measured on assay 1. Data calculated for 15 replicates. Measured with *system 1* on a test bench.

| | Total signal (TnI 200 ng/L) | | Background (0 ng/L) | |
|---|---|---|---|---|
| | Flash lamp | LED | Flash lamp | LED |
| Average power, mW | | 1.27 | | |
| Number of pulses | | 777 | | |
| Frequency, Hz | | 250 | | |
| Pulse energy, µJ | | 5.1 | | |
| Average counts | 2114.1 | 1574.3 | 119.1 | 73.3 |
| (±95%CI) | ±28.6 | ±26.8 | ±12.4 | ±7.1 |
| Sample std. dev. | 51.6 | 48.3 | 22.4 | 12.9 |
| [95%CI] | [37.8; 81.4] | [35.4; 76.2] | [16.4; 35.3] | [9.4; 20.3] |
| $CV_{S(B)}$ | 2.4% | 3.1% | 18.8% | 17.5% |
| S/B @ 200 ng/L | 17.7 | 21.5 | | |
| SNR @ 200 ng/L | 35.5 | 30.0 | | |

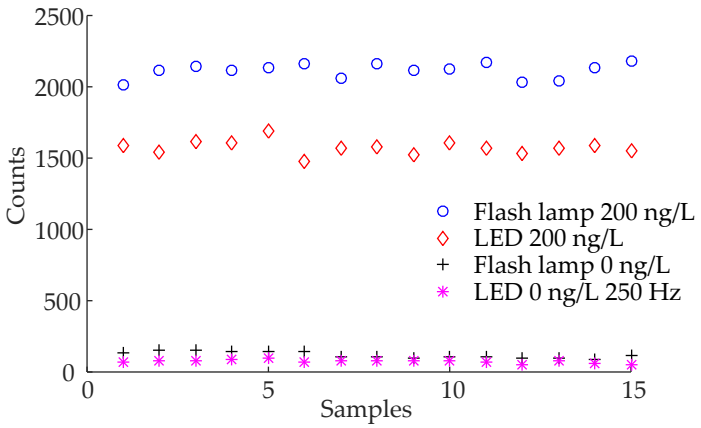


Figure 4.3: Total detected counts of 15 replicates with TnI 200 ng/L concentration and 15 blank cups processed with a solution of null concentration, excited by the flash lamp and LED based systems with equal excitation energy; each point represents one measurement of one test cup with 777 pulses.

It should be noted that a sample size of 15 cups is not sufficient to obtain high statistical precision but it was not the primary goal in this investigation. It would require about 200 replicates to achieve a confidence interval for the standard deviation in the range, $[0.91 \cdot \sigma;\ 1.08 \cdot \sigma]$ at a 95% confidence level. $CV_S$ and $CV_B$ are coefficients of variation for the cups with 200 ng/L concentration and blank cups, respectively. These values are calculated with Eq. 2.12.

Following conclusions have been drawn from the obtained data. Firstly, with the *system 1*, the fluorescence response of the sample cups is 26% lower when excited with the LED unit compared to the flash lamp excitation. We believe the main reason of the reduction is a less optimized spatial overlap between the illumination area and the fluorescence emitting area. The UV LED illumination area in the test cup can be decreased at the cost of collected LED light, as discussed in Section 3. Another possibility is to change the size of the fluorescence emitting area in a test cup. It can be done for example by employing a spot coating [50]. In the spot coating approach, capture antibodies are pipetted in a very small volume in the test cup, thus determining the area of potential location of immunocomplexes. Combination of the two approaches (manipulating the excitation area and the fluorescence emitting area) allows maximization of the overlap. The factor of the area overlap appears to be dominating, as the other two factors of spectral and temporal parameters nearly cancel each other. The longer excitation pulse duration results in a signal reduction of 10%, demonstrated in Fig. 3.10(b), whereas the better spectral overlap of the LED emission is responsible for the 14% signal increase, compared to the flash lamp with the equal pulse energy. Moreover, the information of the europium chelates distribution in the test cups is missing but does probably contribute to the signal change as well. For these reasons the second optical system, *system 2*, with a illumination area was designed and implemented for the measurements.

Secondly, the background level is reduced by 39% when excited by the LED based OU compared to the flash lamp excitation. A thorough discussion of the reasons and the contributing factors is given later in Section 4.6 dedicated to the background noise analysis.

In order to test the full implication of substituting the flash lamp with a LED for the excitation of the europium chelates we performed a comparative study with the SNR as a key performance parameter encompassing all the different aspects as discussed above.

The SNR is calculated as in Eq. 2.10 and was 35.5 and 30.0 for the flash lamp based optical unit and the LED based optical unit, respectively (blue square and magenta rhomb in Fig. 4.4(a). The values are calculated based on 15 replicates. The position of the data point for the flash lamp corresponds to the value of the LED current where the pulse energies of the flash lamp and LED units are equal. The fluorescence response of the sample cups was 26% lower when excited with the LED unit, however the SNR decreased only by 15% for the LED compared to the flash lamp unit. Therefore, the SNR of the LED based unit was comparable to that of the flash lamp unit, with the equal excitation energy. Several properties of the LED based system contribute to the reduced signal level, as discussed above: the increased excitation pulse width and the enlarged illumination area.

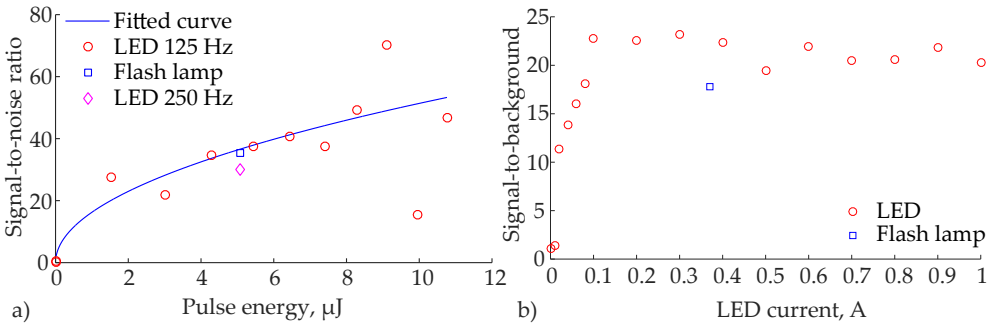


Figure 4.4: a) SNR averaged for four cups vs. LED current (excitation pulse energy) for the TnI concentration of 200 ng/L; the SNR grows with square root with the excitation power; blue square and magenta diamond show the mean values for the experiment with 15 replicates for the flash lamp and LED based unit, respectively; b) S/B ratio as a function of the LED current.

Four extra sample and blank cups were measured to demonstrate the SNR dependence on the excitation energy. The LED was operated at the repetition frequency of 125 Hz however still with the same excitation energy so that it does not affect the signal, but only the measurements take longer time. The SNR grows with square root as a function of the excitation energy as Fig. 4.4(a) demonstrates for a TnI concentration of 200 ng/L (fitted blue curve). The SNR was calculated for four replicates, shown as red circles. The excitation energy was increased by changing the LED current. The LED current was increased up to 1 A, which is by a factor of 2 above the specified maximum current of 0.5 A. The behaviour is explained by the Poisson distributed signal and noise in the system. The outliers at 0.8 and 0.9 A are presumably effects of the large variation of the data, as discussed above. The variation of the data is large due to the small sample size. Higher statistical precision can be achieved increasing the number of samples.

There are several possibilities to improve the SNR of the LED based OU by optimizing different system parameters. The SNR can be improved by increasing the excitation energy using higher LED current and/or longer pulse width. Moreover, for a constant excitation energy the SNR can be improved

in following ways. Firstly, decreasing the excitation pulse width, while keeping the excitation energy constant, will enhance the signal however limited to a 10% improvement, see Fig. 3.10 in Chapter 3. Secondly, a better spectral overlap between the chelate excitation spectrum and the light source emission, will further improve the signal. Many lanthanide based chelates (such as $Eu^{3+}$ or $Tb^{3+}$) have the excitation peak at 340 nm and therefore are a better match to the 340 nm LED [71]. An improvement by a factor of two is expected, if the light source emission peak matches the excitation peak. Thirdly, the delay time between the excitation and detection can be reduced in the LED based system due to the absence of the long afterglow compared to flash lamps. This will result in the increased fluorescence signal. At the same time, the measurement window duration can be increased for the same reason. Lastly, the roughly three times enlarged illumination area compared to the flash lamp system causes a signal reduction, if the spatial overlap is non-optimal and/or the chelates distribution in the cup is non-uniform and the chelates concentration is higher in the center of the cup than in the edges. It was observed that a misalignment of the flash lamp image in the order of 1 mm in the test cup decreases the signal by up to 30% compared to a centered setup. The optimal illumination area with the largest overlap with the chelates distribution will result in higher fluorescence signal.

In order to demonstrate the impact of the LEDs narrower emission spectrum and its absence of afterglow we calculate signal-to-background (S/B) as in Eq. 2.11. The S/B was in our experiments improved by 18% when using the LED illumination compared to the flash lamp system. The S/B behaviour depends mostly on the dominating background contributor, which will be thoroughly investigated later in Section 4.6. The S/B ratio grows rapidly when the excitation energy is small (lower current) and the signal is comparable to the detection system noise, see Fig. 4.4(b). The S/B dependence on the excitation energy ($E_p$) is explained by Eq. 4.1 as in the following.

$$S/B(E_p) = \frac{S_f(E_P)}{B_{total}(E_P)} = \frac{A \cdot E_p}{B_{dark} + C \cdot E_p} \approx \frac{A}{C}. \tag{4.1}$$

The S/B reaches a constant value when the intensity-dependent unwanted fluorescence contributors, $B(E_p) = C \cdot E_p$, which grow with the excitation energy linearly with a coefficient C, are considerably higher than the independent detection background sources, $B_{dark}$. The specific signal, $S_f(E_p) = A \cdot E_p$, also grows linearly with the excitation energy, with a coefficient A. At this point the S/B reaches a plateau and is independent on the excitation energy. The intensity-dependent background noise is much larger than the dark noise, $C \cdot E_p \gg B_{dark}$. Now, the background fluorescence is the dominating source.

## 4.3 MEASUREMENT ON THE STANDARD TNI ASSAY 1 WITH THE OPTIMIZED LED BASED SYSTEM 2

In previous section, the fluorescence signal was lower by 26% when excited by the LED compared to the flash lamp. This was mainly due to the non-optimal spatial overlap of the UV illumination area and the chemically active

area. For assay 1, the size of the active fluorescent area was estimated with a scanning fluorimeter in Radiometer Turku to be approximately 4 mm in diameter. Considering these conclusions, the illumination area was decreased by 36%, from 5x5 $mm^2$ to 4x4 $mm^2$, in order to increase the detected fluorescence signal. In this section and hereafter we have therefore run the experiments with *system 2*. The performance of the LED based instruments was again tested with the standard TnI assay (assay 1). Moreover, the LED based optical units were mounted into the immunoassay analyzers. Five fully automated immunoassay (IA) instruments were used in the experiment. The experiment procedure was as in the following. Firstly, the measurements from the instruments with flash lamp OUs (AQT90 FLEX manufactured by Radiometer Medical) are used as a reference baseline for the measurements. Secondly, the flash lamp OUs were replaced with the LED OUs. Finally, measurements were performed with a single measurement consisting of 3x861 excitation pulses at a repetition frequency of 250 Hz resulting in the total measurement time of 10.3 s. The number of cycles was increased to be equal to that of the first flash lamp based instrument. The samples are BSA-TSA. The sample TnI concentration was 139 ng/L for instrument 1, and 30 ng/L for instruments 2-5. The IA instruments 1-5 are equivalent.

Table 4.4 shows the relative change of the average fluorescence signal of the sample and blank cups for the five instruments. The relative change of signal of the blank cups (processed with assay buffer (AB), i.e. background) has decreased with the LED excitation for four out of the five instruments, whereas the fluorescence signal of the sample cups increased when excited by the LED. The data for the individual test cups measured on instrument 2 is shown in Fig. 4.5. Compared to the previous experiment, the smaller illumination area provides an increased fluorescence signal, all other parameters being equal. With the optimized LED system with instrument 1, the fluorescent signal is higher by 57% compared to the flash lamp system (measured on BSA-TSA samples with TnI concentration of 139 ng/L), see Table 4.4. On average for 5 instruments, the signal increased by 31%, and background dropped by 22%, compared to the flash lamp excitation. As previously reported, with *system 1* the signal with the LED system was by 26% lower compared to the flash lamp system, see Table 4.3. This change corresponds to the better overlap factor $I_{im}$ in Eq. 2.9.

Table 4.4: Relative change of the averaged fluorescence signal of sample cups with a concentration of 30 ng/L and blank cups, after the flash lamp OUs were replaced by the optimized LED based OUs measured with the TnI assay 1.

| Instrument | 1 | 2 | 3 | 4 | 5 | Average |
|---|---|---|---|---|---|---|
| Relative change of sample cups averaged signal, % | +57* | +25 | +40 | +18 | +17 | +31 |
| Relative change of blank cups averaged signal (null concentration, % | -28 | -26 | +17 | -28 | -47 | -22 |

*data for 139 ng/L sample

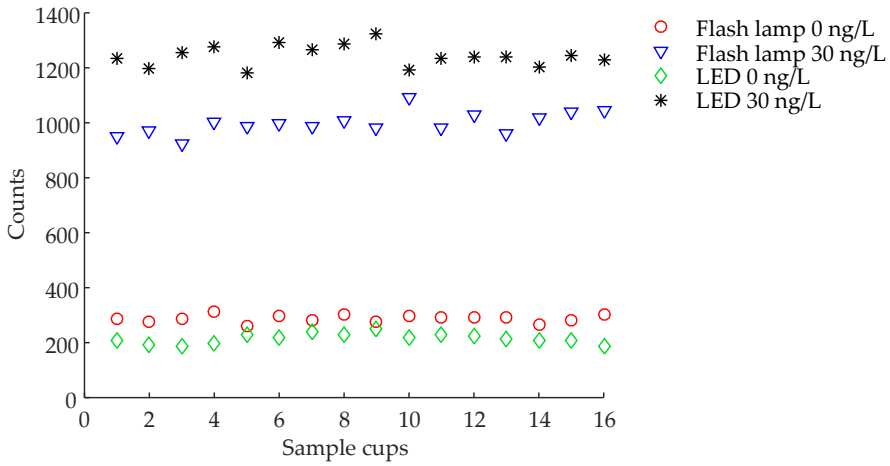


Figure 4.5: Fluorescence signal of 16 replicates measured on instrument 2 for the flash lamp based analyzer (baseline measurement) and with the optimized LED based unit: for blank cups (processed with AQT90 FLEX assay buffer) and BSA-TSA buffer containing 30 ng/L TnI. The fluorescence signal at the concentration of 30 ng/L has increased by 25% whereas the background (concentration of 0 ng/L) dropped by 26%.

In the following, we aim to determine limit of blank (LoB) and LoD of assay 1 measured with the LED based instruments according to the procedure described in Section 2.3. We ran a dilution series with the TnI concentrations of 1; 2.5; 5; 15; 30 ng/L in BSA-TSA. The blank cups were processed with AB. The sample volume was 35 µL. For the first instrument we had 16 replicates for 1; 2.5; 5 ng/L and 8 replicates for 15 ng/L and 30 ng/L. For the other four instruments we had 16 replicates at all concentrations. The LoD was calculated with the low concentration samples of 1; 2.5; 5 ng/L. The SNR and $CV_C$ values are shown as a function of the sample concentration in Fig. 4.6(a) and (b), respectively. The limits of quantification (LoQs) were calculated by fitting a power fit function to the $CV_C$ vs. concentration curves. The dashed line in Fig. 4.6(b) shows the precision profile of a flash lamp based AQT analyzer constructed using the data taken from [67].

The LoBs are calculated to be in the range from 0.8 ng/L to 1.1 ng/L, and the LoDs are in the range from 1.5 ng/L to 2.1 ng/L for the five LED based instruments as shown in Table 4.5. We compare the calculated values of the LoB and LoD to the data of the standard TnI assay measured in the current platform AQT90 FLEX [67], where the reported experiment was performed according to the CLSI EP17-A protocol [72]. The reported LoB was 4.3 ng/L, the LoD 9.5 ng/L, and the concentration that corresponded to the $CV_C$ of 10% and 20% was 24 ng/L and 18 ng/L for WB, and 24 ng/L and 16 ng/L for plasma, respectively. In our experiment the LoB was improved by a factor of 4.7 corresponding to the decreased background value. The LoD was improved by factor of 5. However, it should be noted that our experiments are preliminary in the sense that they do not contain the full required number of replicates as recommended by [54].

In an automated immunoassay analyzer, the alignment of an optical unit and a test cup takes places automatically for each cup, without any manual correction. An imprecise alignment would result in an increased variation of the measurements. Therefore, the alignment of the LED illumination area positioning was tested in the following. A photosensitive paper was

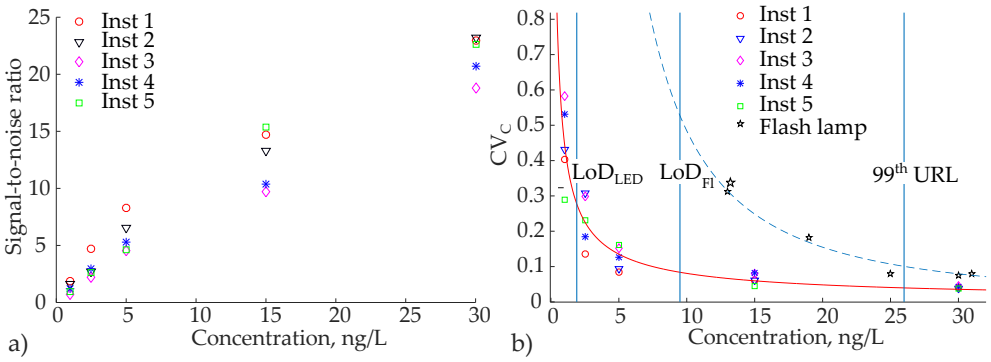


Figure 4.6: SNR (a) and $CV_C$ (b) of the five LED based IA instruments measured on the TnI assay 1. The flash lamp $CV_C$ data is from [67].

Table 4.5: LoB, LoD and LoQ of the five LED based instruments measured on BSA-TSA buffer based TnI samples with TnI assay 1 compared to the current state-of-the art flash lamp based instrument.

| Instrument | BSA-TSA buffer based samples* 1 | 2 | 3 | 4 | 5 | Plasma/WB Radiometer AQT90 FLEX [67] |
|---|---|---|---|---|---|---|
| LoB, ng/L | 0.8 | 0.9 | 1.1 | 0.8 | 1.0 | 4.3 |
| LoD, ng/L | 1.5 | 1.9 | 2.1 | 1.9 | 2.0 | 9.5 (plasma) |
| LoQ ($CV_C$ 20%), ng/L | 1.9 | 2.5 | 3.3 | 2.7 | 2.4 | 18 (WB) 16 (plasma) |
| LoQ ($CV_C$ 10%), ng/L | 5.8 | 6.9 | 8.4 | 7.3 | 6.8 | 24 (WB) 24 (plasma) |
| Averaged background value $\mu_B$, counts | 204 | 214 | 281 | 195 | 149 | |
| Background standard deviation $\sigma_B$, counts | 19 | 18 | 20 | 15 | 14 | |

*LOB determined on AB samples

placed inside 5 test cups, and the cups were then processed automatically by the analyzer. Pictures taken after the processing are shown in Fig. 4.7. The numbers indicate different positions in a process wheel. The pictures demonstrated very good alignment of the LED based system inside an IA analyzer. The illumination area was centered for all processed test cups.

## 4.4 MEASUREMENT ON HIGH-SENSITIVITY TNI ASSAY WITH THE OPTIMIZED LED BASED ANALYZER

In this section we present the results of the LED based instrument using the research hsTnI assay (assay 2). The structure and description of the novel assay are published in [69]. We ran nine BSA-TSA samples, four lithium heparin (LiHep) plasma samples, five ethylenediaminetetraacetic acid (EDTA) plasma samples and two serum samples. The concentration values and number of replicates for each level are shown in Table 4.6. The sample volume

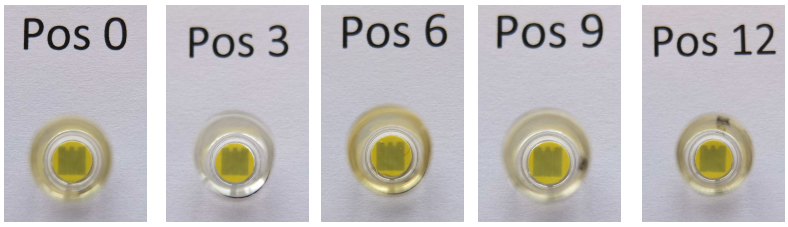


Figure 4.7: Alignment of a LED based optical unit and a test cup inside an analyzer. Pictures are taken after processing in the IA analyzer with the optimized LED based OU (*system 2*). The numbers indicate different process wheel positions.

was 80 µL (increased compared to 35 µL used previously), the shaking speed was increased by a factor of 2.5 to improve the chemical reaction efficiency. Additionally, a parabolic shaped specular reflector was placed under the test cup instead of a flat diffuse reflector. These changes were proven to make a positive impact on the detected signal (unpublished data). The LoB is calculated according to Eq. 2.14 based on the measurements of both BSA-TSA and AB processed blank cups. The LoD is calculated according to Eq. 2.16 based on a combination of 1) low sample signals from the three low level BSA-TSA samples, 2) estimated standard deviation from all BSA-TSA samples, 3) the specific signal level (signal/concentration) of the plasma and serum samples.

The LoD measured with the LED based instrument on plasma with the hsTnI assay was 0.22 ng/L. The hsTnI assay showed a LoD of 0.67 ng/L measured with the flash lamp based instrument and no hardware changes compared to the AQT90 FLEX instrument. The $CV_C$ as a function of sample concentration for the BSA-TSA and plasma samples is shown in Fig. 4.8, measured on the hsTnI assay 2 using both the AQT90 FLEX instrument and the optimized LED based instrument. The $CV_C$ was improved significantly using the LED based OU. The obtained LoD of the LED based instrument is improved by a factor of 3 compared to the LoD of the AQT90 FLEX instrument, see Table 4.7.

Table 4.6: Samples used in the hsTnI assay 2 measurements.

| | | | | | | | | | |
|---|---|---|---|---|---|---|---|---|---|
| Sample | BSA-TSA | | | | | | | | |
| Concentration, ng/L | 0.29 | 0.59 | 0.83 | 1.4 | 2.2 | 4.1 | 8.9 | 17 | 46 |
| Number of replicates | 10 | 10 | 10 | 10 | 5 | 5 | 5 | 5 | 5 |
| Sample | Lithium heparin (LiHep) plasma | | | | | | | | |
| Concentration, ng/L | 0.64 | 1 | 1.8 | 9.3 | | | | | |
| Number of replicates | 5 | 5 | 5 | 5 | | | | | |
| Sample | EDTA plasma | | | | | | | | |
| Concentration, ng/L | 0.8 | 1.1 | 0.62 | 8.4 | 0.23 | | | | |
| Number of replicates | 5 | 5 | 5 | 5 | 5 | | | | |
| Sample | Serum | | | | | | | | |
| Concentration, ng/L | 0.77 | 12.4 | | | | | | | |
| Number of replicates | 5 | 5 | | | | | | | |

Table 4.7: LoB and LoD measured with the LED based instrument and the flash lamp based instrument (AQT90 FLEX) on the hsTnI assay 2.

| Instrument | LED based | AQT90 FLEX (flash lamp based) |
|---|---|---|
| LoB, ng/L | 0.12 | 0.35 |
| LoD on plasma, ng/L | 0.22 | 0.67 |

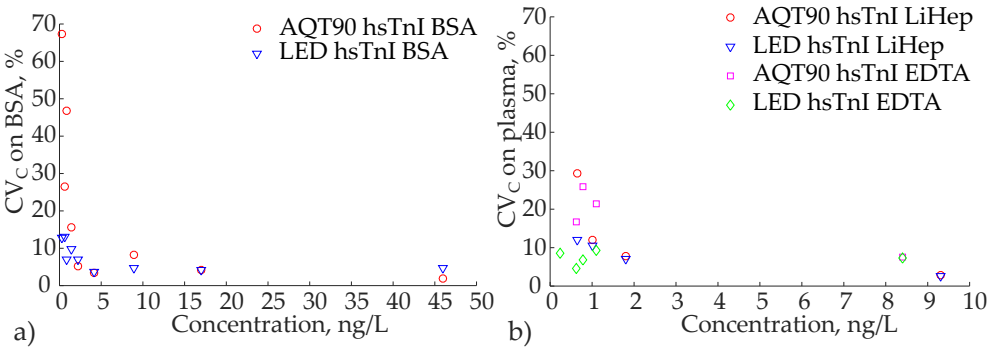


Figure 4.8: $CV_C$ vs. concentration measured on BSA-TSA samples (a) and plasma samples (b) with the LED based analyzer and the AQT90 FLEX analyzer (flash lamp based instrument) with the research hsTnI assay 2.

In order to estimate the required LoD to fulfill the hsTn assay criteria discussed in Section 2.4, we use the data of a prototype hsTnI assay measured with the Dimension Vista® 1500 System (Siemens Healthcare Diagnostics), with the reported LoD of 0.8 ng/L and the $99^{th}$ percentile value of 48 ng/L [59]. The ratio between the $99^{th}$ percentile and the LoD is 60, and measurable values of hsTnI were detected in 88% of the healthy reference cohort. Using the $99^{th}$ percentile value determined for the standard TnI assay of 26 ng/L for plasma, based on 298 plasma samples (152 female and 146 male) [67], we estimate the required LoD to be 0.43 ng/L. The obtained LoD is about a factor of two lower than this value. Based on the set arguments above we expect that the obtained improvement will allow us to meet the hsTnI criteria for PoC applications. The final proof will involve the determination of the $99^{th}$ upper reference limit with the LED based instrument and include a large study of the healthy reference population.

## 4.5 PHOTOBLEACHING STUDY

As discussed in Section 2.2, photobleaching effects can impact fluorescence measurements significantly. It is known that lanthanide based fluorophores exhibit lower bleaching compared to organic fluorophores [10]. However, no data on lanthanides photobleaching rates has been reported, to the authors best knowledge. Therefore, photobleaching of the europium chelates employed in the experiments, is investigated below.

The photobleaching study was performed on assays 1 and 2 with the optimized LED based test bench unit. The sample cups were exposed several hundreds times in a row.

Figure 4.9 shows the normalized fluorescence signal of three test cups (K2, K3 and K5) of the standard TnI (assay 1) as a function of excitation energy and time, measured with *system 1*. The TnI concentration was 200 ng/L.

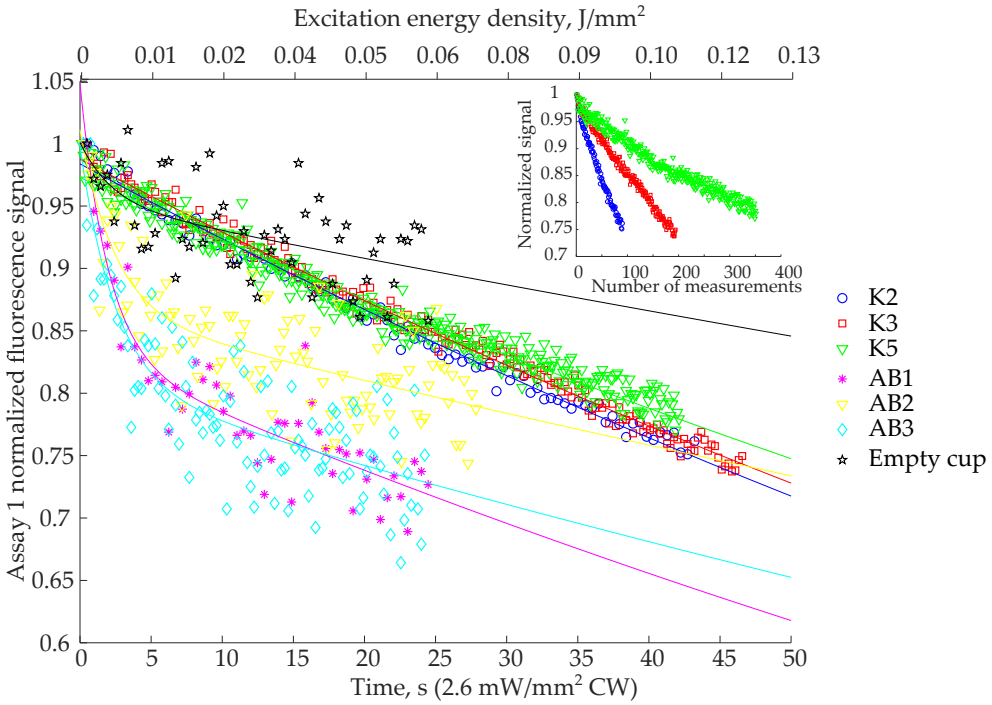


Figure 4.9: Normalized fluorescence signal as a function of excitation energy and time showing photobleaching, of: sample cups (K2, K3, K5) processed with a concentration of 200 ng/L with standard TnI (assay 1); blank cups processed with assay buffer (AB1-AB3); empty cup. Measured with *system 1*. The data were fit to single exponential functions for the sample cups and double exponential for the blank cups and the empty cup. Inset figure: fluorescence signal of the sample cups decreasing with a number of measurements (each measurement contains 1200 cycles).

The test cups were measured on a test bench setup with the LED current of 1.5 A and the pulse widths of 400 µs, 200 µs, and 100 µs, thus different pulse energies of 25.5 µJ, 12.5 µJ, and 6.4 µJ for the sample cups K2, K3 and K5, respectively. The inset figure shows the normalized fluorescence signal decreasing with number of measurements. Each measurement consisted of 1200 cycles. The power density was 2.6 mW/mm$^2$. In addition, the normalized fluorescence signal of three blank cups (AB1-AB3), processed with assay buffer, are shown. The blank cups were exposed to 25.5 µJ (AB1) and 12.5 µJ (AB2, AB3). The empty cup was exposed to 25.5 µJ.

The measured data were fit to single exponential functions (the sample cups) and double exponential functions (the blank cups and the empty cup). We introduce bleaching time constants $\tau_b$ and bleaching energy density constants $j_b$. When a sample is exposed to a bleaching energy density, its fluorescence signal drops to $1/e$, or approximately to 37% of the initial value. The constants calculated for assay 1 are presented in Table 4.8. The sample cups bleach at a rate of 171 s at the exposure level of 2.6 mW/mm$^2$ (average for K2, K3 and K5). The blank cups clearly exhibit double exponential decay with one short bleaching rate of 2.3 s (average for AB1-AB3) and a long bleaching rate approximately in the same range as for the sample cups, 235 s on average. The empty cup bleaching rate constants were not calculated due to too varying data.

For the hsTnI assay (assay 2), the normalized fluorescence signal showing photobleaching is shown in Fig. 4.10. The measured cups include sam-

Table 4.8: Photobleaching rate constants of the sample cups with a TnI concentration of 200 ng/L (K2, K3, K5), the blank cups (AB1-AB3) obtained by curve fitting for replicates measured with assay 1. The exposure level corresponds to 2.6 mW/mm$^2$ CW.

| Assay 1. LQC2, 200 ng/L | | | | |
|---|---|---|---|---|
| | K2 | K3 | K5 | Average |
| $\tau_{b1}$, s | 158 | 164 | 190 | 171 |
| 95% CI | [155; 162] | [162; 166] | [186; 194] | [168; 174] |
| $j_{b1}$, mJ/mm$^2$ | 404.4 | 409.8 | 484.2 | 432.8 |
| 95% CI | [395.8; 413.3] | [404.0; 415.7] | [474.8; 494.0] | [425; 441] |
| Assay 1. Blank cups, 0 ng/L | | | | |
| | AB1 | AB2 | AB3 | Average |
| $\tau_{b1}$, s | 1.9 | 2.4 | 2.5 | 2.3 |
| 95% CI | [1.2; 4.6] | [1.4; 9.5] | [1.5; 6.2] | [1.4; 6.8] |
| $\tau_{b2}$, s | 168 | 303 | 233 | 235 |
| 95% CI | [121; 278] | [193; 709] | [142; 644] | [152; 544] |
| $j_{b1}$, mJ/mm$^2$ | 4.9 | 6.1 | 6.2 | 5.7 |
| 95% CI | [3.1; 11.8] | [3.5; 23.7] | [3.8; 15.5] | [3.5; 17] |
| $j_{b2}$, mJ/mm$^2$ | 429.5 | 757.2 | 581.6 | 589.4 |
| 95% CI | [308.3; 708.1] | [481.5; 1772.1] | [355.2; 1604.0] | [382; 1361.4] |

Table 4.9: Photobleaching rate constants of test cups with a hsTnI concentration of 30 ng/L (LQC1), blank cup (AB) obtained by curve fitting for replicates measured with assay 2.

| | LQC1 | AB |
|---|---|---|
| $j_{b1}$, mJ/mm$^2$ | 17.7 | 2.0 |
| 95% CI | [15.2; 21.1] | [1.5; 3.2] |
| $j_{b2}$, mJ/mm$^2$ | 233.2 | 42.7 |
| 95% CI | [226.2; 240.6] | [30.7; 70.4] |

ple cups with a concentration of 30 ng/L (LQC1), 200 ng/L (LQC2), and a blank cup. The photobleaching constants are shown in Table 4.9. Firstly, the samples with different concentrations exhibit very similar exponential decay (light blue and dark blue), e.g. the photobleaching constants are independent of the analyte concentration. Secondly, the hsTnI assay samples are photobleached faster than the standard troponin assay, probably due to significantly better spectral overlap as discussed in Section 4.1 (see Table 4.2). The exponential decays of assay 1 samples are shown for comparison (green triangles). Thirdly, the blank cups processed with different assays exhibit very different behaviour, compare magenta stars and red squares: the hsTnI blank cups are bleached significantly faster. The reason behind is unknown. Understanding of the photobleaching effects required further investigation.

The main conclusion of the photobleaching study is the following. The excitation energy density of one measurement cycle is 0.31 mJ/mm$^2$ (1000 pulses of 5.1 µJ), which is by two orders of magnitude below the smallest

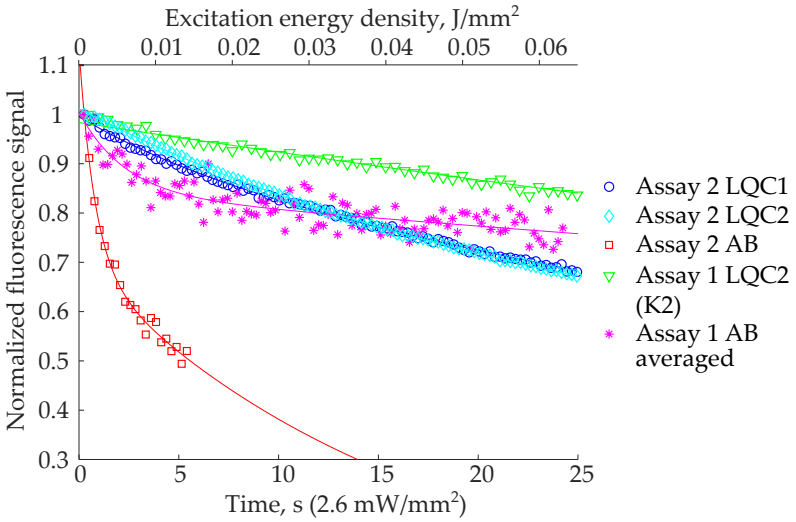


Figure 4.10: Normalized fluorescence signal as a function of excitation energy and time showing photobleaching, of: sample cups with a concentration of 30 ng/L (LQC1) and 200 ng/L (LQC2), blank cup (AB) all processed with hsTnI (assay 2); The data were fit to double exponential functions. For comparison, the exponential decays measured with assay 1 are also shown.

photobleaching constant, $j_{b1}$ of 17.7 mJ/mm$^2$, for assay 2 measured with LQC1, see Table 4.9. For AB samples, the excitation energy density of one measurement cycle is by an order of magnitude larger than the corresponding photobleaching constant (2.0 mJ/mm$^2$). For assay 1, the photobleaching constants are even larger than for assay 2 (433 mJ/mm$^2$ and 235 mJ/mm$^2$, averaged for LQC2 and AB cups, respectively, see Table 4.8). Therefore, the photobleaching effects can be neglected in the measurements.

## 4.6 OPTIMIZATION OF THE LED BASED OPTICAL UNIT

### 4.6.1 *Background contributions analysis*

The background and noise sources in an immunoassay detection system determine the measurement performance, i.e. LoB and LoD, as discussed in Section 2.3. Therefore, it is crucial to understand the main background contributors. We discuss the background and noise sources in the following model. The background contributions in a time-resolved fluoroimmunoassay system are the following:

$$B_{total} = B_{OU} + B_{cup} + B_{chem} + B_{dark} \tag{4.2}$$

$B_{OU}$ is the background fluorescence from the optical unit (no temporal dependence), $B_{cup}$ is the fluorescence of an empty cup (with a decay time of hundreds of µs), $B_{chem}$ is the contribution originated from the non-specific binding of the tracer antibodies with fluorescent markers to the inner walls of the cup (with a decay time of the europium chelate of ms) and $B_{dark}$ is a temperature-dependent constant contribution from the detector (dark counts of the photomultiplier tube (PMT). The background from the OU itself comes from autofluorescence of the employed materials and contamina-

tion. The empty cup, i.e. polystyrene only, absorbs UV light [52], and therefore must emit unwanted light. Indeed, empty cups are known to exhibit the background fluorescence with decay constants about 100 µs [42, 38]. A blank cup, processed with a null concentration solution, contains the chemical layer of antibodies in the bottom, as discussed in Section 2.2. Therefore, the background from a blank cup includes the fluorescence of polystyrene, streptavidin coating, non-specific binding, and contamination, i.e. both $B_{cup}$ and $B_{chem}$. These sources are independent from the useful fluorescence signal. We distinguish between the background contributors that are dependent on the optical system and excitation light and those which are independent from it. The first three sources of the background depend on the excitation light intensity, whereas the detector contribution is independent of the excitation light but is a function of temperature. The PMT dark counts are very low (less than 10 counts per second at 25°C).

Correspondingly, we distinguish the following contributions to the noise in the measurements:

$$N = N_{s.shot} + N_{b.shot} + N_c + N_l + N_i \tag{4.3}$$

N represents variance, or squared standard deviation, and $N_{s.shot}$ is the shot noise of the useful fluorescence signal, $N_{b.shot}$ is the shot noise of the total background defined in Eq. 4.2. The so far mentioned noise contributors refer to the measurement on one test cup. The noise contributions $N_c$, $N_l$, $N_i$ are cup-to-cup, lot-to-lot and instrument-to-instrument variations, respectively. These three noise contributions are not directly related to the background contributions. The cup-to-cup variation can originate both from the variation of individual empty cups ($B_{cup}$), from the difference in the chemical compositions of the cups ($B_{chem}$) and from the variation of cups processing in the instrument (e.g. washing). The lot-to-lot variation is caused by both $B_{cup}$ and $B_{chem}$. The instrument-to-instrument variation includes the variation of the background of the instrument ($B_{OU}$) and the variation of the optical component parameters in the OU. The noise contributions are independent from each other and therefore additive. The dominating noise source determines the signal-to-noise ratio of the measurements.

We first measure the background contributions on a test bench, thus excluding the noise sources of the lot-to-lot and instrument-to-instrument variations. We therefore aim to evaluate all background contributions in Eq. 4.2. The measurements were performed with the LED based *system 1* and compared to the measurement with the flash lamp based system with the same excitation pulse energy and number of cycles. The background of the OU itself was measured with a light tight fixture made of black polyoxymethylene (POM). The fixture is a closed volume without a test cup. All count values below are given for the total time of measurement (777 pulses at a repetition frequency of 250 Hz). For the LED based OU, *system 1* the background from the unit itself measured with the black POM was 26±3 counts (including the PMT dark counts), measured with an empty cup 57±5 counts, and 73±12 counts when measured on the blank cups, see Fig. 4.11(b). The average values and the standard deviations are calculated from the 10 repetitive measurements with the black POM and the empty cups; and from the data of 15 replicates for the blank cups. The flash lamp based OU exhibits

51±5 counts from the unit itself, 95±21 including the empty cup and 119±22 measured with the processed cup. The proportion of the four contributions is approximately the same for the two light sources but the total background level in the LED based unit is reduced by 39%. The points in Fig. 4.11(a) are repetitive measurements performed on one black POM fixture (referred to as OU) and the empty cups.

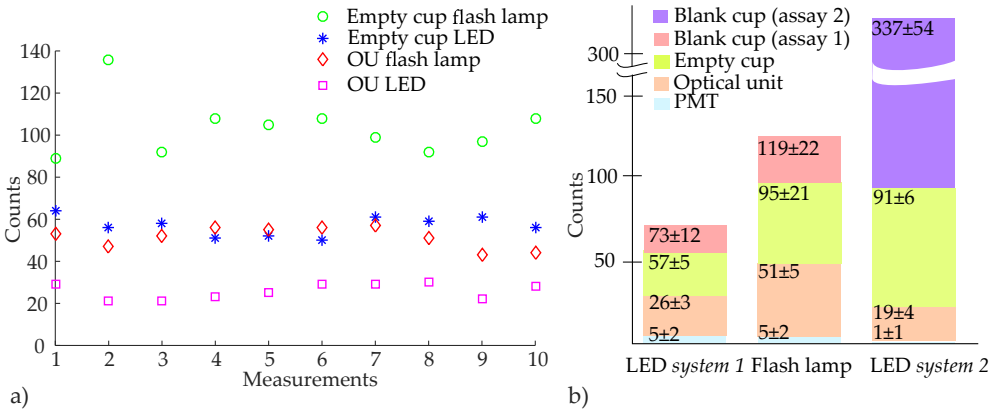


Figure 4.11: The background contributions of the LED (*system 1*) and the flash lamp based systems, a) the repetitive measurements of the OU itself, measured with the black POM closed volume fixture, and the empty cups; b) differentiated background sources for the LED based (*system 1* and *system 2*) and the flash lamp excitation: the PMT dark counts, the optical unit background, the empty cup (polystyrene only) and the blank cup (processed cup with a null concentration, assay 1 and 2).

The background reduction when measured with the LED *system 1* is partially explained by several factors. Firstly, the LEDs emission spectrum is narrower compared to the flash lamp spectrum and thus the spectral match to the background excitation spectrum is worse. Secondly, the intensity of the long-lived part of the background contributing to time gated measurements depends on the excitation pulse width. With a longer pulse width, the number of molecules emitting unwanted light is lower (see discussion in Section 3.2 and Fig. 3.10) and it drops faster if the background lifetime is shorter than the fluorophore lifetime. Finally, the amount of stray light is reduced in the LED based unit due to the optical system and the absence of reflectors in the excitation light path, in contrast to the flash lamp based system.

The background contributions were also measured with LED *system 2*, see Fig. 4.11(b). The optical unit background is 19±4 counts and is approximately as low as of the *system 1*. The empty cup background is 91±6 counts. The blank cup signal, measured with assay 2, is 337±54 counts, which is almost 5 times higher than that for the assay 1. The reason is that the assay 2 is more sensitive and has a larger spectral overlap with the LED spectrum, compared to assay 1, see Table 4.2.

### 4.6.2 *Optimization of the timing parameters of time-resolved fluorescence measurements*

In this optimization study we used the research hsTnI assay (assay 3) to experimentally determine optimum timing parameters of the time-resolved

detection of the europium chelates. Four LED based instruments were employed in the experiments, where the LED OUs were supplemented with a parabolic shaped specular reflector. No other hardware changes were made (normal sample volume, normal shaking speed). We ran a dilution series of ternary troponin complex diluted in a BSA-TSA buffer with the concentrations of 0; 0.25; 0.5; 1; 5; 30 ng/L. Here the blank samples were processed with a BSA-TSA null concentration buffer.

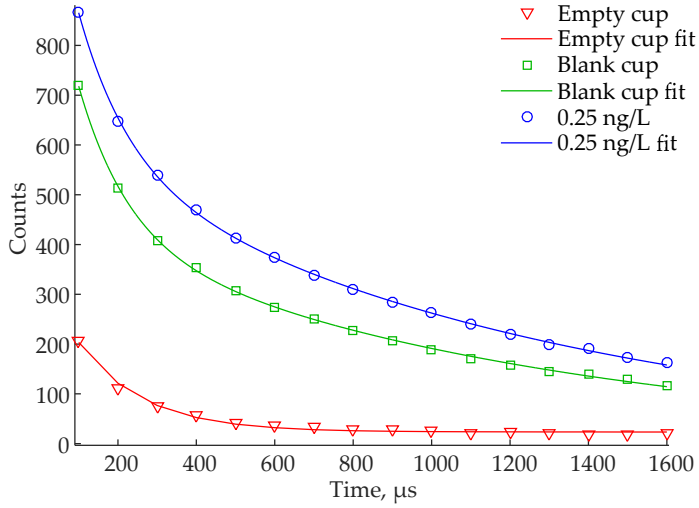


Figure 4.12: The fluorescence decays of empty cup (red), blank cup (green), and cup processed with the sample of 0.25 ng/L with the hsTnI assay 3 (blue).

Table 4.10: Fluorescence decay lifetime constants of an empty cup and BSA-TSA samples with a TnI concentration of 0 ng/L (blank cup), 0.25 ng/L and 30 ng/L obtained by curve fitting for the replicates measured on one instrument.

| | Empty cup | Blank cup (BSA-TSA + 0 ng/L TnI) | BSA-TSA + 0.25 ng/L TnI | BSA-TSA + 30ng/L TnI |
|---|---|---|---|---|
| Decay constant(s)*, µs | 155.6 (84.1) | 124.0 (43.6)<br>1049.6 (168.1) | 128.6 (42.8)<br>1108.0 (142.7) | 1168.1 (8.8) |
| Replicates | 16 | 32 | 32 | 8 |

*Average (std. dev.)

We have analyzed the decay time constants of empty cups (polystyrene only), blank cups (processed with BSA-TSA with null concentration), low concentration sample of 0.25 ng/L and high concentration sample of 30 ng/L. The data is averaged for 16 replicates for the empty cup, 32 replicates of the blank cup and the 0.25 ng/L sample, and for 8 replicates using 30 ng/L. The 16 replicates of the empty cups showed the variation CV of 10.7% of detected counts. We fitted a single exponential function to all replicates and obtained an average lifetime fluorescence decay of 155.6 µs with a standard deviation of 84.1 µs (CV 54.0%) with added constant background from the optical unit as shown in Fig. 4.12 (red curve) and Table 4.10. The constant term is calculated to be 23.4±4.0 counts. The blank cup which includes the chemical immunocomplexes before the processing, exhibits dou-

ble exponential fluorescence decay with time constants of 124.0±43.6 µs and 1049.6±168.1 µs. We believe that the short fluorescence decay of 124.0 µs comes from the empty cup and that the long decay is caused by the non-specific binding of tracer antibodies (with europium chelate attached) to the inner walls of the cup. However, due to high variation of the empty and blank cups the fitting data should be interpreted with caution. The decay curve of the cup processed with a low concentration sample of 0.25 ng/L shows the same double exponential behaviour. The cup processed with the high concentration sample of 30 ng/L shows only a single long lifetime exponential decay of 1168.1±8.8 µs because the europium fluorescence decay dominates the signal.

Table 4.11: Statistical data measured on four instruments with the hsTnI assay 3.

| | BSA-TSA + 0 ng/L TnI | | | BSA-TSA + 0.25 ng/L TnI | | |
|---|---|---|---|---|---|---|
| Inst. | Averaged signal, counts | Standard deviation, counts | $CV_S$, % | Averaged signal, counts | Standard deviation, counts | $CV_S$, % |
| 6 | 1128 | 56 | 4.9 | 1510 | 56 | 3.7 |
| 7 | 1441 | 82 | 5.7 | 1866 | 67 | 3.6 |
| 8 | 1410 | 57 | 4.0 | 1862 | 67 | 3.5 |
| 9 | 1306 | 82 | 6.2 | 1850 | 125 | 6.7 |
| Average | 1320 | 142 | 10.7 | 1773 | 172 | 9.7 |

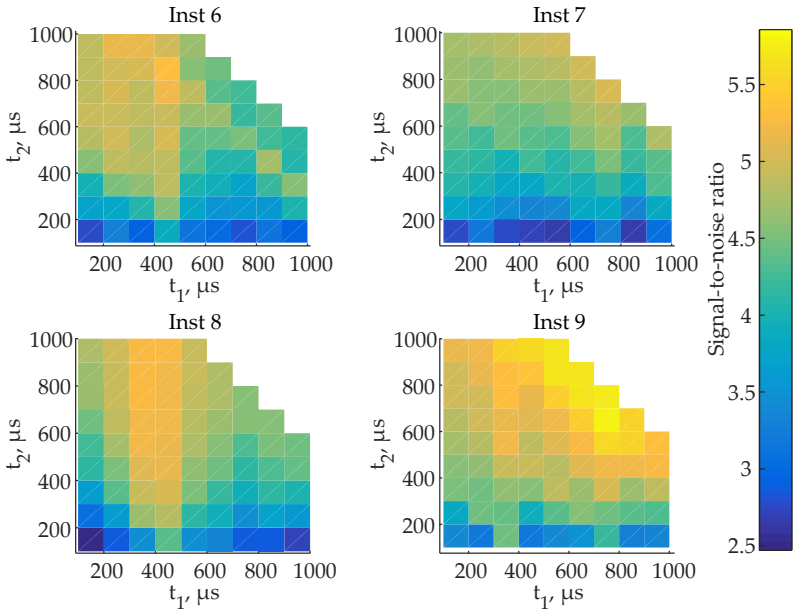


Figure 4.13: SNR calculated for four LED based instruments measured on BSA-TSA samples with a TnI concentration of 0.25 ng/L as a function of the timing parameters: $t_1$ as pre-delay time (i.e. time after the end of the excitation pulse before the measurement), and $t_2$ as duration of the measurement time window.

Table 4.11 presents statistical data for the blank cups and the sample cups with a concentration of 0.25 ng/L for four LED based instruments measured on the hsTnI assay 3. The cup-to-cup variation of the blank cups, measured

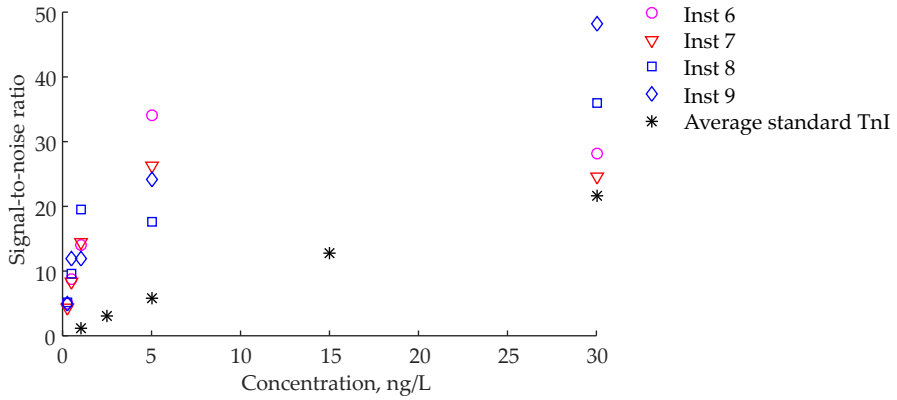


Figure 4.14: SNR calculated for four LED based instruments with the currently employed settings with the pre-delay time of 400 µs and the measurement window duration of 400 µs, measured on BSA-TSA samples with the novel hsTnI assay 3. The black star points represent the average value for the LED based instruments measured on the standard TnI assay 1.

on one instrument, does not exceed 10% for all four instruments. However, the instrument-to-instrument variation is 10.7%. For the sample cups with a concentration of 0.25 ng/L, the variation between the instruments is also larger than the cup-to-cup variations. In the following, we average the data for the cup replicates but present the instruments separately, thus only the cup-to-cup variations are present.

The optimal timing parameters such as pre-delay time, i.e. the time between the end of the excitation pulse and the measurement window, and the duration of the measurement time are determined by the fluorescence decay constants of the europium chelate and the background noise in the system. In the following, we analyze the impact of these timing parameters on the SNR as shown in Fig. 4.13 for a concentration of 0.25 ng/L, where $t_1$ is the pre-delay time and $t_2$ refers to the duration of the measurement. The optimum pre-delay time has to be longer than the decay time of the short fluorescent cup background signal (see Table 4.10), i.e. 300-400 µs after the excitation pulse. The longer measurement window improves the SNR due to higher signal. At high concentrations such as 30 ng/L the impact of the timing parameters is not evident due to the high europium signal, however, at low concentrations the SNR is improved as suggested. The data contains the cup variation as described above. The noise of the measurement and the SNR are dominated by the cup-to-cup variation as explained in the following. With one set of cups as presented here, division of the replicates into two equal sized groups, a calculation of the SNR for the two groups lead to slightly different results, where the behaviour of the SNR is not necessarily maintained. This confirms the conclusion that the cup-to-cup variation is larger than the effect of timing parameters on the SNR. Correspondingly, when increasing the excitation energy the improvement is not obtained because the cup-to-cup noise contribution dominates over the shot noise.

The SNR calculated for the LED based instruments configured with the standard timing parameters (pre-delay of 400 µs and measurement window of 400 µs) is shown in Fig. 4.14. The SNR is improved for the hsTnI assay 3 compared to the TnI assay 1 when measured with the LED based instruments, compared to Fig. 4.6. The SNR generally improves at lower

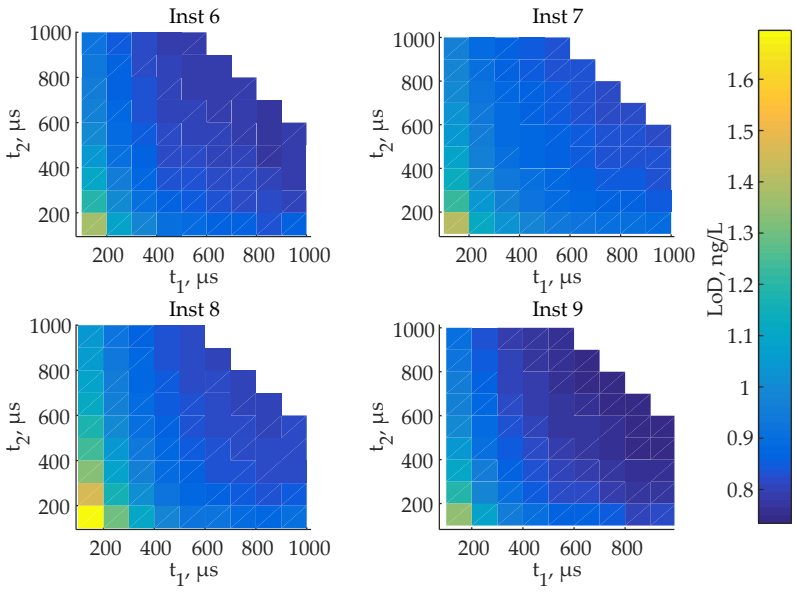


Figure 4.15: LoD calculated for four LED based instruments as a function of the pre-delay time $t_1$ and the duration of the measurement time window $t_2$.

concentrations. However, at a concentration of 30 ng/L the improvement is not seen supposedly due to high cup-to-cup variations.

The LoD was calculated according to Eq. 2.16 from the samples with low concentrations of 0.25; 0.5; 1 ng/L as shown in Fig. 4.15. The LoD is in the range of 0.8-1.2 ng/L and is optimum for the longer pre-delay time and the longer measurement time as discussed above. However, it did not exhibit a strong dependence on the parameters, excluding the case with the shortest both pre-delay time and measurement window. The LoD is higher than that obtained in Section 4.4, probably because the experiment was performed on the BSA-TSA samples, with the slightly different hsTnI assay 3 (two tracer antibodies vs. one tracer antibody) and without the two mentioned platform changes: larger sampling volume and accelerated shaking.

## 4.7 CONCLUSION

For the first time to our knowledge, a time-resolved fluorescence system based on a 340 nm LED was successfully employed for immunoassays detection. With *system 1*, a test with real immunoassay samples of the cardiac marker TnI (200 ng/L), showed comparable SNR for the LED and the Xenon flash lamp, respectively, for the same excitation pulse energy. A SNR of 35 (measurement time 3 s), equal to that of the flash lamp system, was obtained without overdriving the LED. The SNR can be further improved by increasing the LED current. Moreover, for constant excitation energy, the SNR can be improved by reducing the illumination area, having shorter excitation pulse width and shorter delay time, and possibly better spectral match with the europium chelate excitation spectrum. The signal-to-background was improved significantly when excited by the LED, expectedly due to the absence of the flash lamps afterglow and narrower emission spectrum of the LED.

With *system 2*, we have tested a novel LED excitation based immunoassay instrument intended for PoC use. The laboratory tests were performed with a standard TnI assay (assay 1) and a research prototype hsTnI assay (assay 2). The LoD was improved by a factor of 5, from 9.5 ng/L to 1.9 ng/L, for the standard TnI assay when measured with the LED based instrument, significantly outperforming the state-of-the-art flash lamp OU based instrument. The improvement was achieved primarily by optimizing the overlap between the UV illumination area and the chemically active area where the immunocomplexes are located. Including the LEDs small footprint, cheaper price, better efficiency and heat dissipation, we conclude that UV LEDs will likely soon replace Xenon flash lamp excitation in immunoassays time-resolved detection systems based on long lifetime fluorophores.

In the implementation of the novel research hsTnI assay with the LED based instrument we have obtained a detection limit of 0.22 ng/L measured on plasma, showing an improvement by a factor of 3 compared to the flash lamp based instrument. Using data for an existing hsTnI assay from an external manufacturer, we estimated the required value of LoD to be 0.43 ng/L in order to meet the hsTnI criteria. The combination of the LED excitation and the prototype hsTnI assay enabled the LoD of 0.22 ng/L, which is 49% below the estimated requirement. We believe our preliminary results are an important step in the development of the hsTnI assay in PoC testing and that the hsTnI criteria will soon be documented in PoC systems using LED excitation, ultimately leading to more accurate interpretation of clinical tests and earlier diagnosis and rule-out of acute myocardial infarction (AMI).

We suggested a model which includes the background and noise contributions to describe immunoassay detection. The model can be generally applied to lanthanide-based heterogeneous time-resolved fluoroimmunoassays. We showed that the temporal decay of the background in the system includes two exponential terms. We performed an optimization analysis of the LED based fluorescence immunoassay measurement system. The SNR can be improved by choosing the optimal pre-delay time to largely match that of the short background decay time (about hundreds of μs), whereas the long lifetime decay term originating from the non-specific binding of the tracer antibodies to the cups inner walls cannot be filtered. We also demonstrate that the cup-to-cup variation is a dominating noise contributor that is limiting the instrument performance. We analyzed and explained the SNR and S/B behaviour when the cup-to-cup variation is absent.

# 5

# PASSIVELY Q-SWITCHED SOLID STATE UV LASER

The objective of this part of the project is to develop a low repetition rate UV solid state laser emitting at 343 nm with sufficient pulse energy. The developed laser benefits from passive Q-switching operation, resulting in high energy pulses at low and at the same time controllable repetition rate. No active components and complex electronics are involved. The 343 nm laser is obtained by the third harmonic generation of a passively Q-switched Yb:YAG laser emitting at 1030 nm. The following two chapters are based on the developed UV laser source. In this chapter, the developed Yb:YAG laser, and consequently cascaded nonlinear conversion are discussed. In the next chapter, the results of the laser-induced fluorescence measurements of immunoassays are discussed.

## 5.1 PASSIVELY Q-SWITCHED SOLID STATE YB:YAG LASER AT 1030 NM

### 5.1.1 *Yb:YAG laser medium*

The Yb:YAG laser medium energy diagram is shown schematically in Fig. 5.1. A $Yb^{3+}$ ion has two Stark splitted manifolds: the ground $^2F_{7/2}$ state with four sub-levels, and the excited $^2F_{5/2}$ with three sub-levels. Because the lower energy states are very close to the ground state, the laser medium operates as a quasi-three-level laser. It can be pumped at the absorption bands of 940 nm or 968 nm. The absorption coefficient at 968 nm is higher, however the absorption spectrum bandwidth is significantly more narrow at this wavelength compared to the absorption band at 940 nm [73]. The Yb:YAG medium has a long upper level fluorescence lifetime (951 µs), large gain bandwidth, and low quantum defect. The long upper state lifetime potentially allows for storage of high energy and is especially beneficial for a quasi-three-level laser. The upper state lifetime is about four times longer than that of a Nd:YAG laser medium and the absorption bandwidth at 940 nm is 5 times wider than that for 808 nm of a Nd:YAG laser medium. The quantum defect for the absorption at 940 nm is by a factor of 3 smaller compared to that of Nd:YAG, i.e. 0.09 versus 0.32.

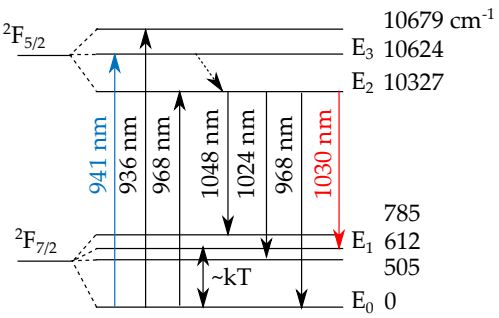


Figure 5.1: Schematic energy diagram of a Yb:YAG laser medium.

As previously mentioned, the energy diagram forms a quasi-three-level system. At room temperature, the lower states are populated, which causes the reabsorption of the laser emission and therefore reduces the laser gain. Thus, the population inversion is difficult to obtain which results in a high lasing threshold. The lasing transitions include 1024 nm, 1030 nm, and 1048 nm and terminate at different lower levels. In contrast to four-level lasers, the emission wavelength and the gain bandwidth depend on the excitation level and thus on the doping level and the cavity loss. The Boltzmann occupation factor of the lower level for the transition at 1030 nm is 0.046 at the room temperature. The thermal population of the lower level causes the reabsorption of the laser wavelength and therefore net population inversion is not easily obtained under low pump power. The Boltzmann occupation factor of the lower level of the transition at 1048 nm is 0.02. Thus, lasing at 1048 nm can be observed under low pump power. Moreover, a change of the cavity loss can result in a different laser wavelength. Although the emission cross-section is higher at 1030 nm than at 1048 nm, for low cavity loss, 1048 nm operation is favoured by the quasi-three-level nature (strong reabsorption at 1030 nm). In literature, a laser operation at 1050 nm [74], a dual wavelength laser at 1030 and 1049 nm [75], and a tunable laser in the range of 1023-1054 nm [76] were reported. The thermal load of the quasi-three-level structure limits the laser efficiency. However, the energy diagram of Yb:YAG medium also exhibits a few advantages. Firstly, the quantum defect is low, 0.087. Secondly, since there are no higher-lying energy levels, the problems of excited-state absorption and upconversion are eliminated.

For a laser medium operating as a quasi-three-level laser, it is critical to maintain the laser crystal temperature as low as possible. With higher temperature, the population of the lower laser levels increases, leading to increased reabsorption and thus reduction of the population inversion. Moreover, to mitigate the effect of the thermal lensing, it is critical to have good thermal contact between the laser crystal and the mount. The aspects of different mounting options have been investigated in [77].

Yb:YAG lasers have most often been pumped at 940 nm, although Yb:YAG lasers pumped at 968 nm have also been reported [78]. The potential reason is the lack of diode lasers at 968 nm compared to that at 940 nm and the difference in the absorption bandwidth.

### 5.1.2 *CW operation*

During the development and characterization of the Yb:YAG laser, a few conclusions were made regarding the laser operation which are not directly related to the objective of the thesis. Therefore, these results are reported in Appendix A.3 and only briefly discussed here.

In this work, the Yb:YAG laser is pumped at the 940 nm absorption band. The broad absorption band at 940 nm of the Yb:YAG medium conveniently absorbs possible wavelength fluctuations of the pump laser diode. Even though the central wavelength of the laser diode often varies in the range from 935 nm to 945 nm, it is not beneficial to temperature tune the pump diode spectrum. The decrease of the diode output power with increased temperature dominates over the temperature compensated spectrum of the

diode. For our experiments, the shifted pump wavelength is therefore accepted. This point will be discussed in more details later.

As discussed above, in a quasi-three-level laser the emission wavelength depends on the losses in the cavity. Thus, in a standard cavity the emission wavelength is a function of the output coupler reflection. In a continuous wave (CW) mode, the laser operates at 1058 nm, 1048 nm, and 1030 nm with the output coupler (OC) reflection of 0.998, 0.98 and 0.9, respectively. All OCs are curved mirrors with a radius of curvature (ROC) of 100 mm. The pump beam diameter is 210 µm in the laser crystal (LC). The slope efficiency and threshold as a function of the OC reflection are shown in Fig. A.3. With the OC reflection lower than 0.9, the laser operates at 1030 nm. The power output is 1.7 W and 0.8 W for OC reflections of 0.98 and 0.9, respectively, at an incident pump power of 7.4 W. The cavity length is 30 mm. With the OCs being plane mirrors with a reflection of 0.6, 0.7, and 0.8, the output power reaches 2.1 W, 2.1 W, and 1.9 W, respectively, at an incident pump power of 9.1 W. The cavity length is in this case 20 mm. The slope efficiency is 0.43, 0.43, and 0.39, and the lasing threshold is 3.0 W, 2.98 W, and 2.94 W for the OC reflection of 0.6, 0.7, and 0.8, respectively, with a cavity length of 15.5 mm. The slope efficiency and threshold as a function of the cavity length are shown in Fig. A.4. The nonsaturable intracavity round-trip dissipative optical loss is experimentally determined to be 3%.

The cavity was first built with a magnification of the pump lens focusing system of $-2$, resulting in the pump mode diameter of 210 µm in the laser crystal. The pump magnification was later increased to $-3.33$, corresponding to the pump mode diameter of 349.7 µm in the laser crystal. This was done due to damage of the saturable absorber (SA) crystals, which will be thoroughly discussed later. Correspondingly, the pump diameter is increased by a factor of 1.7, and consequently, the pump mode area is increased by a factor of 2.8.

With a pump mode diameter of 349.7 µm, an output power up to 0.5 W at an incident pump power of 8.3 W is obtained with an OC reflection of 0.8 (cavity length of 13 mm) and 0.9 (cavity length 30 mm). The slope efficiency is 0.20 and 0.21, and the lasing threshold is 5.7 W and 5.9 W for an OC reflection of 0.8 and 0.9, respectively. Compared to a pump magnification of $-2$, the slope efficiency decreased and the threshold increased nearly by a factor of 2 for the OC reflection of 0.8 (with the magnification of 2 it is 0.39 and 2.9 W, respectively). The CW operation with an OC reflection lower than 0.8 could not be obtained due to even higher lasing threshold, resulting in overheating of the laser crystal. It has been demonstrated that as small as possible pump mode volume is preferred even in a quasi-three-level system [79].

For the sake of compactness, following notations are introduced in this chapter. An OC with a reflection of 80% is denoted as R0.8 (R for reflection and 0.8 is the partial reflection). A pump lens focusing system with a magnification of $-2$ is denoted as M2 (M for magnification).

### 5.1.3 *Thermal lens analysis*

In a plane-parallel cavity, the combination of the thermal lens and the soft Gaussian aperture in the laser crystal determines the optical axis and the

laser mode size. Therefore, the thermal lens defines the stability of the laser operation and the laser mode size. We aim to investigate the thermal lensing in a Yb:YAG laser in the following.

The Yb:YAG laser medium has a positive thermo-optic coefficient which forms a positive thermal lens. The focal length of the thermal lens depends on the pump power and also on the intracavity laser power. We calculate the focal length theoretically and determine it experimentally in the following. The focal length of a thermal lens $f_{th}$ is calculated as:

$$f_{th} = \frac{2kA}{\frac{dn}{dT} P_{th}} \tag{5.1}$$

where $k$ is the thermal conductivity, $A$ is the area of the pump mode in the laser crystal, $\frac{dn}{dT}$ is the thermo-optic coefficient, and $P_{th}$ is the thermal power dissipated in the laser crystal. The thermal conductivity is 7.5 $\frac{W}{m \cdot K}$, determined for 10%Yb:YAG in [80], and $\frac{dn}{dT}$ is $9.86^{-6}$ $K^{-1}$ [81]. It should be noted that the exact material parameters are unknown thus introducing uncertainty in the calculations.

Besides the unknown material parameters, the thermal power is not easily determined. The thermal power is a fraction of the absorbed pump power, $P_{abs}$: $P_{th} = \eta_h \cdot P_{abs}$, where $\eta_{th}$ is the fractional thermal load. The latter is defined as:

$$\eta_h = 1 - \eta_p \left[ (1 - \eta_l)\eta_r \frac{\lambda_p}{\lambda_f} + \eta_l \frac{\lambda_p}{\lambda_l} \right] \tag{5.2}$$

where $\eta_p$ is the pump extraction efficiency, $\eta_l$ is the laser extraction efficiency, $\eta_r$ is the radiative quantum efficiency, $\lambda_p$ and $\lambda_l$ is the pump and laser wavelength, respectively. $\lambda_f$ is the fluorescence wavelength and is equal to 1007 nm [82]. The radiative quantum efficiency $\eta_r$ is

$$\eta_r = \frac{\tau_{nr}}{\tau_{nr} + \tau_{LC}} \tag{5.3}$$

where $\tau_{nr}$ is the nonradiative lifetime and $\tau_{LC}$ is the upper state lifetime. $\eta_r$ was experimentally determined in [82] to be 0.7, then the nonradiative lifetime is calculated to be 2.2 ms.

In some literature the fractional thermal load is defined to be equal to the quantum defect $\eta_q$ of the laser medium which is equal to 0.09 for Yb:YAG. However, this is only the case when both the pump efficiency, $\eta_p$, and the laser extraction efficiency, $\eta_l$, are equal to 1. The fractional thermal load is then $\eta_{th} = 1 - \frac{\lambda_l}{\lambda_p}$. In most cases, when measured experimentally, the fraction of the absorbed pump power is higher than defined by the quantum defect due to laser extraction efficiency, $\eta_l$ being smaller than 1. Therefore, in the following we aim to investigate the dependence of the thermal lens focal length on the laser extraction efficiency.

The laser extraction efficiency is defined as [83]:

$$\eta_l = \frac{Q_{stim}}{Q_{stim} + Q_{spont} + Q_{nr}} \tag{5.4}$$

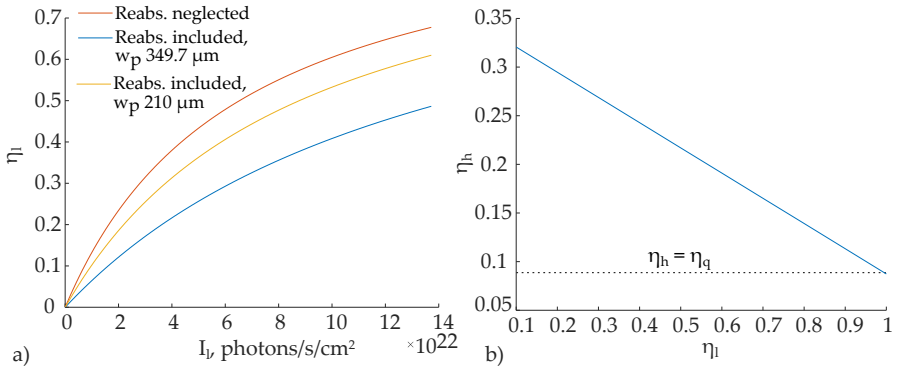


Figure 5.2: a) The laser extraction efficiency $\eta_l$ as a function of the intracavity laser intensity $I_l$, calculated considering the reabsorption at the lasing wavelength (blue and yellow curves) and neglecting the reabsorption (red curve); b) fractional thermal load $\eta_h$ as a function of the laser extraction efficiency.

where $Q_{stim}$ is the stimulated emission rate, $Q_{spont}$ is the spontaneous emission rate and $Q_{nr}$ is the nonradiative relaxation rate. $Q_{stim}$ is defined by the number of the stimulated photons emitted when an excited atom decayed from level 2, minus the number of the reabsorbed photons by the atoms in level 1: $Q_{stim} = \sigma_e N_2 I_l - \sigma_a N_1 I_l$, where $I_l$ is the intracavity intensity expressed in photons$\cdot s^{-1} cm^{-2}$, $\sigma_a$ is the absorption cross-section at the lasing wavelength, $\sigma_e$ is the emission cross-section at the lasing wavelength, $N_2$ and $N_1$ are the population of the upper and lower laser levels, respectively. In turn, $Q_{spont}$ and $Q_{nr}$ are defined as the number of photons spontaneously emitted and nonradiatively decayed from the level 2, respectively: $Q_{spont} = \frac{N_2}{\tau_{LC}}$ and $Q_{nr} = \frac{N_2}{\tau_{nr}}$. Combining the definitions into Eq. 5.4, one obtains:

$$\eta_l = \frac{I_l \left[(\sigma_a + \sigma_e)\frac{N_2}{N} - \sigma_a\right]}{I_l \left[(\sigma_a + \sigma_e)\frac{N_2}{N} - \sigma_a\right] + \frac{N_2}{N \cdot \tau_{LC}} + \frac{N_2}{N \cdot \tau_{nr}}} \tag{5.5}$$

where $N$ is the total population ($N = N_1 + N_2$). We use the theory for the quasi-three-level laser operation given in [84] in order to calculate the fraction of the upper laser level population $\frac{N_2}{N}$ in the steady state:

$$\frac{N_2}{N} = \frac{\sigma_{ap} I_p + \sigma_a I_l}{(\sigma_{ep} + \sigma_{ap}) I_p + (\sigma_e + \sigma_a) I_l + \frac{1}{\tau_{LC}}} \tag{5.6}$$

where $\sigma_{ap}$ is the absorption cross-section at the pump wavelength, $I_p$ is the intracavity pump intensity, and $\sigma_{ep}$ is the emission cross-section at the pump wavelength.

Eq. 5.5 takes into account the reabsorbtion at the laser wavelength, as described. When the reabsorption of the laser wavelength is neglected, as in the case of a four-level laser ($\sigma_a N_1 \ll \sigma_e N_2$), Eq. 5.5 is simplified to:

$$\eta_l = \frac{\sigma_e I_l}{\sigma_e I_l + \frac{1}{\eta_r \tau_{LC}}} \tag{5.7}$$

Both Eq. 5.5 and Eq. 5.7 describe the laser extraction efficiency which depends on the intracavity laser intensity $I_l$. In the following, the impact of

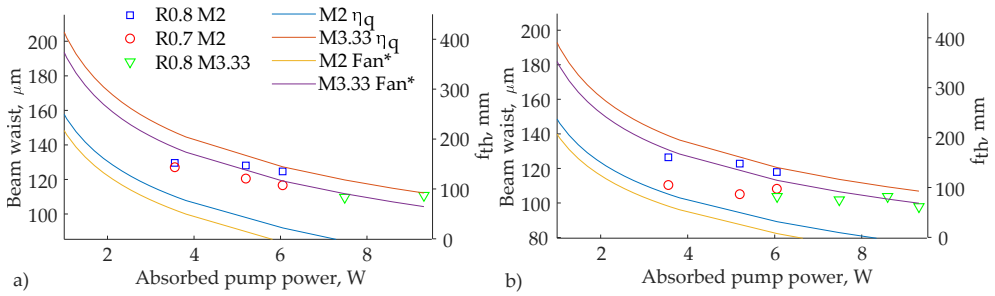


Figure 5.3: Beam waist and focal length of the thermal lens as a function of absorbed pump power for an output coupler reflection of 0.6 and 0.7 and cavity lengths of 20.0 mm (a) and 15.5 mm (b), respectively. The pump diameter is 210 μm (M2) or 349.7 μm (M3.33).
*Fractional thermal load from [85].

the reabsorption in a quasi-three-level laser is demonstrated. Figure 5.2(a) shows the laser extraction efficiency as a function of the intracavity laser intensity, calculated considering the reabsorption at the lasing wavelength (yellow and blue curves) and neglecting the reabsorption (red). The pump extraction efficiency $\eta_p$ is assumed to be 1. The parameters used in the calculation are given in Table 5.1. The higher the intracavity laser intensity, the closer the laser extraction efficiency to 1. $\eta_l$ decreases due to reabsorption and also depends on the pump mode size and the pump power, decreasing with larger pump mode size. The linear dependence of the fractional thermal load on the laser extraction efficiency is shown in Figure 5.2(b). The smaller the laser extraction efficiency, the larger the fractional thermal load is, resulting in the stronger thermal lens. Therefore, it is beneficial to operate several times above the lasing threshold, where the laser extraction efficiency is closer to 1 and the fractional thermal load approaches the quantum defect limit. The reabsorbtion loss should not be neglected for a quasi-three-level laser. Several values of the fractional thermal load have been reported in literature: 0.18 [80], 0.11 [85].

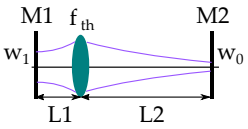


Figure 5.4: A plane-parallel cavity with a thermal lens.

In the following, we first calculate the beam waist and the focal length of the thermal lens theoretically, using the plane-parallel resonator geometry with an intracavity lens, and then measure the values experimentally. The theory of the plane-parallel laser geometry can be found in [86]. The beam waist and the focal length of the thermal lens as a function of the absorbed pump power are plotted in Fig. 5.3 (solid lines). These are calculated with Eq. 5.1 assuming the plane-parallel resonator geometry with an intracavity lens with the focal length $f_{th}$, as shown in Fig. 5.4. The values were calculated with the fractional thermal load equal to the quantum defect (denoted as $\eta_q$ in the figure) and the fractional thermal load reported by Fan [85]. The values are calculated for both a pump mode diameter of 210 μm and 349.7 μm, and for a cavity length of 20 mm (a) and 15.5 mm (b), respectively. Firstly, as seen comparing the lines for M2 and M3.33, the larger pump beam area results in larger laser beam waist, or weaker thermal lens. This result is obtained assuming that the fractional thermal load $\eta_h$ in Eq. 5.1 is constant. However, this is not the case as will be discussed in the next paragraph. Secondly, with the shorter cavity length, the beam waist is smaller. Finally, larger values of the fractional thermal load $\eta_h$ (yellow and purple) result in the smaller beam waist size. Even a relatively small difference of the

fractional thermal load used, e.g. 0.09 vs. 0.11 [85], results in a significant (tens of μm) change of the beam waist size. The largest beam waist for a given cavity, pump power and pump diameter, is limited by the quantum defect.

In the next step, we aim to determine the focal length of the thermal lens experimentally. The beam size is measured with a beam scanner at several z positions. From the far-field divergence angle, the beam waist is determined, which is located at the OC in a plane-parallel cavity. We calculate the cavity parameters of the plane-parallel cavity with a thermal lens located in the laser crystal [86], as shown in Fig. 5.4. When the beam size $w_0$ is known, the focal length of the thermal lens $f_{th}$ is calculated by solving the following equation [86]:

$$\left[\frac{w_0^2\pi\cdot(f_{th}-L1)}{\lambda_l L\cdot(f_{th}-L2)}\right]^2=\frac{f_{th}^2(f_{th}-L1)}{(f_{th}-L2)\cdot(f_{th}^2-[f_{th}-L2]\cdot[f_{th}-L1])} \tag{5.8}$$

where $w_0$ is the measured beam waist, L1 and L2 are the distances between the first plane mirror M1 and the thermal lens, and between the thermal lens and the second plane mirror M2, respectively, $\lambda_l$ is the lasing wavelength, and L is the total distance, $L = L1 + L2$.

The experimentally determined beam waist and the focal length of the thermal lens, calculated with Eq. 5.8, are shown in Fig. 5.3 as a function of the absorbed pump power for a cavity length of 20 mm (a) and 15.5 mm (b). The data is obtained in CW operation under continuous pumping. The absorbed pump power is determined under non-lasing conditions. Firstly, the beam waist decreases with both increased pump power and decreased cavity length, as expected. Secondly, the beam waist decreased with the lower output coupler reflection (compare R0.8 and R0.7), because in the latter case the intracavity laser density is lower for the same pump power and the threshold is higher, so that the laser operating point is closer to the threshold. Thus, the laser extraction efficiency decreases, and the fractional thermal load is higher, resulting in the stronger thermal lens. The beam waist decreases from 130 μm to 125 μm for an OC of R0.8, and from 127 μm to 117 μm for an OC of R0.7, for absorbed pump power in the range from 3.5 W to 6.0 W (cavity length of 20 mm). This corresponds to the thermal lens focal length ranging from 145 mm to 130 mm for an OC of R0.8 and from 140 mm to 108 mm for an OC of R0.7, in the same range of the absorbed pump power. Thirdly, the measured values for M2 are larger than calculated, which is not possible because the largest beam waist is determined by the quantum defect limit and cannot be larger. Therefore, the material parameters (k and $\frac{dn}{dT}$ in Eq. 5.1) are not precise. It is not trivial to determine analytically the absolute value of the thermal lens focal length due to the uncertainty of the material parameters. Fourthly, for the larger pump mode volume, M3.33, the measured beam waist does not increase as Eq. 5.1 dictates, but is in the same range as with M2. This is likely due to the larger thermal load for the larger pump size, as predicted in Fig. 5.2(a). The increased pump mode volume impacts the laser extraction efficiency significantly, resulting in the higher thermal load at the same pump power.

To conclude, although a Yb:YAG crystal is often cited for its small quantum defect resulting in smaller heating issues, however one should take into

consideration the increased thermal load due to the reabsorbtion and the nonradiative sites. The fractional thermal load can deviate from the quantum defect significantly. One should not assume the fractional thermal load to be constant when varying the pump mode size or pump power. This will result in a misleading calculation of the focal length of the thermal lens.

### 5.1.4 *Q-switched operation*

The passive Q-switched laser operation is obtained with a $Cr^{4+}$:YAG crystal as SA, which is selected due to the advantages such as low cost, relatively high damage threshold, and simplicity.

Passively Q-switched Yb:YAG lasers have been reported as both bulk lasers and microchip lasers, the latter being either in a standard resonator configuration (external) or in a microchip resonator configuration. However, high-power Yb:YAG lasers are mostly designed as composite microchip resonators [28]. They have high repetition frequency, high pulse energy, short cavity length, thus short pulse width and high peak power. Often the microchip laser crystals are grown to have an undoped Yb region in the front part of the crystal to overcome the mechanical surface deformation of the laser crystal due to the thermal effect, and to mitigate the thermal lensing effect. The Yb:YAG and $Cr^{4+}$:YAG crystals can be diffusion-bonded and have the same crystal orientation, at the same time forcing a linearly polarized output. The air gap between a laser crystal and a SA in a bulk laser significantly affects the laser performance [87].

In this work, a bulk passively Q-switched laser is developed. The bulk design was preferred due to its flexibility, i.e. easy replacement of the components. Moreover, diffusion-bonded composite crystals are considerably more expensive.

#### 5.1.4.1 *Experimental setup*

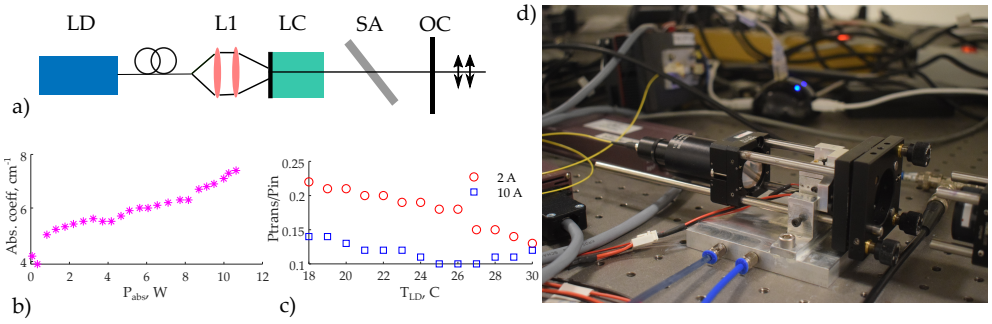


Figure 5.5: a) Experimental setup of the passively Q-switched Yb:YAG laser; b) absorption coefficient of the laser crystal at 940 nm as a function of absorbed pump power, measured under non-lasing conditions; c) the ratio of transmitted and incident pump power as a function of the laser diode temperature; d) photograph of the Q-switched laser.

The experimental setup of the passively Q-switched laser is shown schematically in Fig. 5.5(a) and as a photograph in Fig. 5.5(d). The pump diode (LD) is manufactured by Lumentum Operations LLC with a specified center wavelength of 940 nm. The fiber has a core diameter is 105 µm, a NA of

Table 5.1: Parameters of the passively Q-switched laser employing Yb:YAG as LC and $Cr^{4+}$:YAG as SA: absorption cross-section of ground and excited state of SA ($\sigma_{gSA}$ and $\sigma_{gSA}$), excited-state lifetime of SA and LC ($\tau_{SA}$ and $\tau_{LC}$), stimulated emission and absorption cross-section of LC at 1030 nm ($\sigma_e$ and $\sigma_a$), absorption coefficient of LC at 940 nm ($\alpha$), length of LC ($d_l$), nonsaturable intracavity round-trip dissipative optical loss (L), absorption and emission cross-section of LC at 940 nm ($\sigma_{ap}$ and $\sigma_{ep}$), averaged fluorescence wavelength ($\lambda_f$), radiative quantum efficiency ($\eta_r$), reflectivity of output coupler (R), cavity length ($l_c$), diameter of the pump beam in LC ($d_p$), inversion reduction factor ($\gamma$), and nonradiative lifetime ($\tau_{nr}$).

| Parameter | Value | Ref. | Parameter | Value | Ref. |
|---|---|---|---|---|---|
| $\sigma_{gSA}$, $cm^2$ | $3.2 \cdot 10^{-18}$ | [81] | $\sigma_e$, $cm^2$ | $2.3 \cdot 10^{-20}$ | [81] |
| $\sigma_{eSA}$, $cm^2$ | $4.5 \cdot 10^{-19}$ | [81] | $\sigma_a$, $cm^2$ | $0.1 \cdot 10^{-20}$ | [73] |
| $\tau_{SA}$, µs | 3.4 | [81] | $d_l$, mm | 3 | |
| $\tau_{LC}$, µs | 951 | [81] | R | 0.6 | |
| $\alpha$, $cm^{-1}$ (10 at.%) | 6 | Meas. | $l_c$, mm | 13 | |
| L | 0.03 | Meas. | $d_p$, µm | 210/349.7 | |
| $\sigma_{ap}$, $cm^2$ | $7.7 \cdot 10^{-21}$ | [81] | $\gamma$ | 2 | |
| $\lambda_f$, nm | 1007 | [82] | $\tau_{nr}$, ms | 2.2 | [82] |
| $\eta_r$ | 0.7 | [82] | $\sigma_{ep}$, $cm^2$ | $0.07 \cdot 10^{-20}$ | [73] |

0.15 and a power output of up to 10.6 W. The laser diode is operated at a constant temperature of 18°C. The light emitted from the pump diode is focused into the laser crystal with a magnification of either −2 or −3.33 (lens system L1), resulting in a pump beam diameter of 210 µm or 350 µm, respectively. The laser crystal (10%Yb:YAG) is manufactured by Castech Inc. and has a transverse dimension of 5x5 $mm^2$ and a thickness of 3 mm. The laser crystal is wrapped in indium foil to improve the thermal conductivity at the interface between the crystal and the heat sink. The laser crystal is coated: HR@1030 nm and HT@940 nm at the front surface facing the pump diode and AR@1030 nm at the intracavity surface. A temperature controller keeps the temperature of the laser crystal fixed at 15°C. For a quasi-three-level gain medium the temperature is highly relevant to control, as the population of the lower laser level increases with temperature thus reducing the laser efficiency. A $Cr^{4+}$:YAG crystal is employed as a saturable absorber enforcing Q-switched operation of the laser. The saturable absorber is placed approximately 6 mm after the laser crystal at Brewsters angle to enforce a linearly polarized light output. The OC is a partially reflective plane mirror. The cavity length is in total 13 mm (optical length).

A summary of the laser parameters is given in Table 5.1. The length of the Yb:YAG crystal is chosen so that it absorbs a minimum of 95% at 940 nm. The density of laser active ions for 10% doping is calculated to be $1.37 \cdot 10^{21}$ $cm^{-3}$. The absorption coefficient is determined experimentally under non-lasing conditions and is in the range from 0.53 $mm^{-1}$ to 0.74 $mm^{-1}$ for an incident pump power ranging from 1.77 W to 10.63 W, see Fig. 5.5(b). The central wavelength of the laser diode at room temperature is below 940 nm, but can be temperature tuned to reach 940 nm. Figure 5.5(c) shows the ratio of the transmitted pump power to the incident pump power as a function of

the laser diode temperature at constant laser diode current. At a current of 2 A, the ratio decreases with the laser diode temperature due to the spectral tuning. The central wavelength also depends on the laser diode current. There are two competing effects: firstly, the junction temperature increases with higher current, thus increasing the central wavelength, and secondly, increase in the electron density at the junction with higher current, thus decreasing the wavelength. Usually, the thermal effect dominates, resulting in longer wavelength with increasing the current. Thus, the normalized transmitted power is smaller at 10 A, compared to 2 A. Then, at the current of 10 A, the ratio of the transmitted power does not decrease significantly as at 2 A. In addition to that, the power output of a laser diode decreases with higher operating temperature. Therefore, in out system it is not beneficial to temperature tune the spectrum at a smaller current. In contrast, at higher current, the central wavelength of the laser diode increases, so temperature tuning is not needed.

The parameters of the employed SA crystals are discussed separately in in the following section.

#### 5.1.4.2 *Saturable absorbers*

The summary of the SA crystals employed for Q-switching in this work is shown in Table 5.2. The reason of the variety of employed SAs is the observed damage of the SAs, which is thoroughly discussed below. The total population density of the SA, $N_{s0}$ is calculated from the small signal transmission, $T_0$, the SA length, $d_{SA}$ and using the ground state absorption cross-section from [81]. $Cr^{4+}$:YAG crystals with a small signal transmission of 80% and 90% from three vendors were employed. All $Cr^{4+}$:YAG crystals were inserted under the Brewsters angle to enforce a linearly polarized output. Thus, the SA crystals were uncoated. In addition, $V^{3+}$:YAG crystals were also tested as SA for the reasons described later. $V^{3+}$:YAG crystals have an absorption cross-section of the ground and excited state of $3{\cdot}10^{-18}$ $cm^2$ and $1.4{\cdot}10^{-19}$ $cm^2$, respectively [88]. $V^{3+}$:YAG crystals have lower absorption at 1030 nm than $Cr^{4+}$:YAG and are not commonly used for 1 µm lasers, but rather for the lasers operating at 1.3 µm, where $Cr^{4+}$:YAG crystals cannot be employed.

In contrast to the CW operation, in the Q-switched configuration the laser always operates at 1030 nm. In the following, the results were obtained with a pump magnification of $-2$ (M2). With the SA from Casix, with $T_0$ of 90%, the obtained pulse energy is 130 µJ at a repetition rate of 2.8 kHz, resulting in the average power of 360 mW (pumped with 8.2 W), using the OC of R0.6. With the same SA but with the OC of R0.8, the measured pulse energy is 110 µJ at the repetition rate of 4.3 kHz, resulting in an average power of 470 mW (pumped with 7.9 W). With the SA from Altechna, with a $T_0$ of 80%, the obtained pulse energy is 250 µJ at a repetition rate of 2.2 kHz, corresponding to an average power of 530 mW (pumped with 8 W), using the OC of R0.8.

We used the model of a passively Q-switched Yb:YAG laser given in [89] to estimate the laser output parameters. The laser beam waist size in the model is calculated with CW theory (see Fig. 5.3). Under continuous pumping as employed here, the SA crystals were damaged so that it was not possible to experimentally determine the actual beam size. Therefore, the model results

Table 5.2: Summary of the $Cr^{4+}$:YAG crystals employed in passive Q-switching. The total population density of SA ($N_{s0}$) is calculated using the small signal transmission ($T_0$) and the SA length ($d_{SA}$). $S-D$ is the surface quality (scratch-dig). All uncoated.

| Nr. | $T_0$, % | Manufact. | Damag. | $d_{SA}$, mm | S-D | $N_{s0}$, $\cdot 10^{17}$ $cm^{-3}$ |
|---|---|---|---|---|---|---|
| 1 | 80 | Altechna | yes | 1.75 | 40-20 | 4.0 |
| 2 | 80 | Casix | yes | 1 | 20-10 | 7.0 |
| 3 | 90 | Casix | yes | 0.4 | 20-10 | 8.2 |
| 4 | 80 | FEE | no | 1.74 | 10-5 | 4.0 |
| 5 | 90 | FEE | no | 0.84 | 10-5 | 4.0 |
| 6* | 90 | Eksma | no | 1.0 | 20-10(?) | 3.5 |
| 7* | 95 | Eksma | no | 0.5 | 20-10(?) | 3.5 |

*$V^{3+}$:YAG

are used as estimates only. With the model the pulse energy is 199 µJ at 11 kHz, pumped with 7.4 W, employing the SA from Casix (90%) and the OC of R0.6. The model predicted a pulse energy of 283 µJ at 5.7 kHz, when pumped with 6.5 W.

The major challenge faced when operating in the Q-switched configuration was the damage of the SA crystals. After the first sign of damage, the pump size was increased by a factor of 2.8, changing the pump magnification from $-2$ to $-3.33$. It was done to limit the intracavity laser intensity and thus avoid the SA damage. In addition, the OC reflection was changed from R0.8 to to R0.6 to decrease the intracavity peak power. However, both SA crystals, from Altechna and Casix, with a $T_0$ of 80% and 90%, respectively, were still damaged in the Q-switched operation under continuous pumping, both using a magnification of M2 and M3.3. Therefore, in the following we aim to determine the intracavity peak power density and compare to the values reported in literature.

Only the laser cavity with $V^{3+}$:YAG could operate with CW pumping without damaging the SA, due to significantly lower pulse energies obtained. With $V^{3+}$:YAG, pulse energies up to 27 µJ are obtained, with a small signal transmission of 10% and an OC of R0.9, corresponding to 0.37 mW at 14 kHz, with an incident pump power of 7 W.

We calculated the intracavity peak power density for the 1030 nm laser based on the Gaussian effective area $A_{eff} = \frac{\pi w^2}{2}\frac{1}{cos\theta_B}$, where $\theta_B$ is the Brewsters angle. The beam area is calculated using the resonator geometry and the measurements of the thermal lens in the CW regime. It was later determined, that under high incident pump power, the laser beam in Q-switched operation is larger than calculated with CW condition. The data is shown in later sections. However, we still use the calculated beam waist values to determine the maximum intracavity peak power density and the maximum fluence. The values obtained in this work are shown in Table 5.3. As a result, with the SA from Altechna with the pulse energy of 250 µJ, the intracavity fluence is <7.0 J/$cm^2$, or the peak power density is <0.70 GW/$cm^2$, calculated for a laser beam radius of 99 µm (for a pump power of 7 W and pump magnification M2). The pulse width was 10 ns. With a pump magnification of M3.33, the fluence was <3.6 J/$cm^2$, and the peak

power density is <0.36 GW/cm$^2$, for a laser beam radius of 117 µm. For the SA from Casix with $T_0$ of 90% and an OC of R0.8, the fluence was <3.1 J/cm$^2$. The intracavity peak power density was <0.31 GW/cm$^2$.

The laser induced damage threshold (LIDT) of $Cr^{4+}$:YAG crystals is reported to be >500 MW/cm$^2$ (1064 nm, 10 ns) by most vendors, which corresponds to a fluence of 5 J/cm$^2$. As seen in Table 5.3, only in one case, i.e. with the SA from Altechna ($T_0$ of 80%) and the magnification M2, the calculated maximum values exceed the LIDT specified by the vendors. For the SA crystals from Casix, and the SA from Altechna but with M3.33, the peak power density and fluence are below the LIDT, but they yet were damaged. It is known that the LIDT depends on the laser parameters: it decreases with shorter wavelength and higher repetition rate, and increases with longer pulse width [86]. The LIDT is most often specified for 1064 nm and 10 ns. The wavelength change from 1064 nm to 1030 nm corresponds to the LIDT decrease only by 3%. The pulse width was measured to be slightly longer than 10 ns, which would increase the LIDT.

Table 5.3: Summary of high power passively Q-switched lasers employing $Cr^{4+}$:YAG crystals. The LIDT provided by crystal vendors is >0.5 GW/cm$^2$, or >5 J/cm$^2$ (1064 nm, 10 ns).

| Reference | Configuration | P, GW/cm$^2$ | Fluence, J/cm$^2$ | t | Dam. |
|---|---|---|---|---|---|
| [90] | Microchip reson. | 70 | 11.2 | ps | yes |
| [90] | Microchip ext. reson. | 4 | 100 | ns | yes |
| [91] | Microchip reson. | | 16 | ns | yes |
| [87] | Microchip reson. | 3 | 10.6 | ns | no |
| [28] | Microchip reson. | 20 | 31.8 | ns(?) | no |
| [81] | Thin disk ext. reson. | 0.05 | 1.5 | ns | yes |
| [29] | Bulk ext. reson. | 0.2 | 1.1 | ns | yes |
| [92][a] | Microchip ext. reson. | 0.2 | 2.7 | ns | no |
| | This work. Maximum values[b] | | | | |
| Altechna 80% M2; M3.33 | Bulk laser | <0.70; <0.36 | <7.0; <3.6 | ns | yes |
| Casix 90% M2; M3.33 | Bulk laser | <0.18; <0.09 | <1.8; <0.9 | ns | yes |
| FEE 90% M3.33 QCW pump | Bulk laser | 0.18[c] | 1.0[c] | ns | no |

[a] Laser beam area estimated.

[b] Laser beam area calculated for CW operation, with $\eta_h$ of 0.11. In reality the beam sizes are larger. Thus, the maximum values are shown here. For details, see text.

[c] Measured.

However, in literature, operation above the LIDT without damage is reported. Moreover, a few LIDT values are reported which are different from that specified by vendors. Table 5.3 summarizes some of the values reported in literature. The reported values are obtained mostly with microchip lasers, since high energy bulk lasers have not yet been reported (without damage). The highest reported pulse energy obtained with a bulk, passively

Q-switched Yb:YAG laser employing an undamaged $Cr^{4+}$:YAG is 63 µJ [93], which corresponds to an intracavity intensity that is significantly below the vendors LIDT level of $Cr^{4+}$:YAG. In [29], a high-power bulk passively Q-switched Yb:YAG laser, pumped with InGaAs QCW diodes of 120 W, is reported with an output energy up to 0.98 mJ, however with damage to the Cr:YAG. In the following, we investigate the conditions under which the SA crystals are damaged and aim to draw a few useful conclusions.

Firstly, the microchip resonator configuration, where the high-reflective and partially reflective coatings (serving as the laser mirrors) are directly applied onto the composite crystal surfaces avoiding air gaps in the cavity, increases the LIDT considerably, compared to the external resonator configuration. In a microchip resonator, the fluence of up to 31.8 $J/cm^2$ can be obtained without damage for ns pulses, respectively [28]. Thus, the values in our work cannot be directly compared to the values obtained with microchip resonators. Instead, we compare to the external resonator configuration. Secondly, the LIDT of 2 $GW/cm^2$ for the standard (external) resonator is reported in [90]. With the external resonator, a fluence up to 2.7 $J/cm^2$, or intensity of 0.2 $GW/cm^2$, was obtained without damage [92]. These values of the intracavity intensity and the fluence are similar to values in our work (except for the SA by Altechna with a $T_0$ of 80%, M2), however in the reference the $Cr^{4+}$:YAG crystals are not damaged. Finally, it is observed that the SA crystal from FEE, although resulting in about the same power density and intracavity fluence, is not damaged, unlike the SA by Casix under similar conditions. The intracavity peak power density and fluence are similar to those obtained in [81, 29] in an external resonator cavity, where the employed SAs are damaged. Therefore, we believe there is a direct correlation between the crystal surface quality and the LIDT. As seen in Table 5.2, the SA crystals by Altechna have the lowest surface quality compared to other SA crystals, 60/40 scratch-dig (S-D). The SA crystals with the best surface quality by FEE have 10-5 S-D, and no damage is observed.

Since the employed SA crystals are uncoated, the observed damage is not caused by any AR coatings. A coating usually has the lowest damage threshold, compared to surface and bulk damage. It is known that the surface damage has a significantly lower LIDT compared to bulk damage; by a factor of 5, according to [86]. We believe the SA crystals experienced the surface damage. Surface damage mechanism is explained in the following. Even after polishing, optical surfaces have residual scratches and imperfections on the surface. The surface damage happens in the proximity of these defect centers. The damage caused by polishing defects appears as small dots (pin-points) at the damaged surface [94]. The number of surface defects is defined by the surface quality, which is described by the scratch-dig parameter. Standard quality optics usually have scratch-dig of 80-50, precision quality optics have scratch-dig of 60-40, and high precision quality optics have scratch-dig of 20-10.

Photographs of the damaged $Cr^{4+}$:YAG crystal from Altechna are shown in Fig. 5.6. The photographs are taken by an external research institute, FEE GmbH. The damage pattern is replicated on both front (a) and rear (b) surfaces and appears like small dots. Figure 5.6(c) shows the polishing defects on the surfaces (green circles). As mentioned previously, most likely it was a surface damage experienced here. Moreover, it was determined by

FEE that the small signal transmission $T_0$ of the SA from Altechna is 72.6% at the Brewsters angle at 1030 nm, whereas the specified value is 80%. The lower small signal transmission of an SA results in higher intracavity pulse energy, increasing the damage probability.

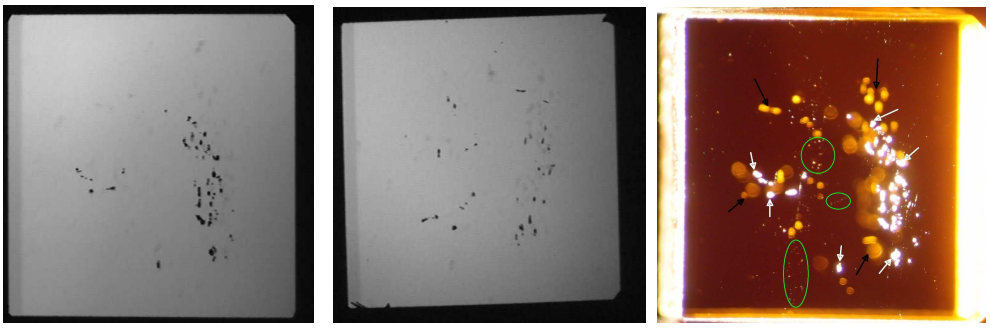

a) b) c)

Figure 5.6: Photographs of the damaged uncoated SA crystal $Cr^{4+}$:YAG manufactured by Altechna with a surface quality $S-D$ of 60/40: a) front surface; b) rear surface; c) white arrows: laser damages (white) on the top side, black arrows: laser damages (yellow) on the rear side, green circles: lots of points (faults) in the surface (photographs taken by FEE GmbH).

The SA crystals from Altechna were also damaged under pulsed pumping (with the OC of R0.8 and R0.6, M3.33), although in the pulsed pumping mode the thermal load is significantly smaller, resulting in a weaker thermal lens and thus larger laser beam. Only the SA crystals from Casix with $T_0$ of 90%, and from FEE with $T_0$ of both 80% and 90%, operated in a stable fashion under pulsed pumping.

To conclude, in addition to the dependence of LIDT on the laser parameters such as wavelength, pulse width, repetition rate, the LIDT also depends on additional parameters such as the resonator configuration and the surface quality. Thus, the LIDT should not be defined universally. For high-power lasers, the surface quality is an extremely relevant parameter. The lower the quality, the higher is the probability of surface damage. The recommended surface quality for high-power lasers is 10-5 S-D. Moreover, high-power lasers with intracavity intensities exceeding 0.18 GW/cm$^2$, or 1.0 J/cm$^2$ (1030 nm, 5 ns, 100 Hz) are recommended to be designed as microchip resonators with no air-crystal surface interface.

#### 5.1.4.3 *Results and discussion*

With the application of the lanthanide fluorescence in mind and considering the following requirements, we designed a final Yb:YAG passively Q-switched laser, operating in a stable fashion with high pulse energy. Figure 5.5(a) shows the experimental setup. In the following, important parameters of the designed laser are discussed.

1. Pump modulation is employed for several reasons. Firstly, the trigger pulse to the laser diode is simultaneously used to trigger the fluorescence measurement in a simple and elegant fashion. Secondly, the thermal effects are significantly lowered due to lower thermal load, although the obtained pulse energy is as high as with the CW pumping. Thus, the thermal lens is weaker which increases the laser beam size

in the SA and prevents damage. Thirdly, in order to achieve the low repetition rates required by the lanthanides long fluorescence lifetime, i.e. hundreds of Hz, the pump power has to be very low. In that case, the CW pumped, Q-switched laser operates very close to the threshold and thus unstable. This is avoided in our design. Besides, for CW pump the operation point close to the threshold increases the fractional thermal load, which results in stronger thermal lens and again potentially leads to damage of the SA. The lowest repetition rate using CW pumping was observed to be as low as 697 Hz with an average power of 180 mW, resulting in a pulse energy of 258 µJ (obtained with the OC of R0.6 and the SA from Casix with $T_0$ of 90%).

2. The SA $Cr^{4+}$:YAG crystal employed in the final design is manufactured by FEE GmbH, with the main advantage of the high surface quality of the crystal. Then, the crystal is designed for the small signal transmission of 90% when installed at the Brewsters angle and measures 5x5x1 $mm^3$. The SA with $T_0$ of 90% is selected due to the following. It is known that the higher the concentration of the SA, or the thicker the SA, the higher the pulse energy obtained. With $T_0$ of 80%, the pulse energy of 318 µJ was obtained, which corresponds to an average power of 35 mW at 110 Hz. However, laser operation was very unstable, probably due to the operation close to the threshold, just overcoming the level of losses.

3. The cavity length is as short as possible to promote a short pulse duration and thus higher peak power which is beneficial for nonlinear frequency conversion.

4. The larger pump beam diameter, 349.7 µm versus 210 µm, was chosen in order to avoid damage of the saturable absorber employed in the cavity. With M3.33, the Q-switched laser does not operate under continuous pumping due to too high thermal load.

5. The OC is a plane mirror with low reflection of 60% at 1030 nm, which decreases the intracavity power and increases the output power.

As discussed in Section 2.2, lanthanide based chelates have long fluorescence lifetime in the range of one millisecond. The system designed and developed in Chapter 4 operates at 250 Hz, which corresponds to a cycle time of 4 ms. The low repetition rate is dictated by the long fluorescence lifetime of the europium chelate used, of 1 ms. In our laser setup, the laser diode is externally triggered at a repetition rate in the range from 10 to 180 Hz and with a pulse width of 2 ms. The same electronic trigger signal can also be used for a detection circuit relevant for our target application. The diode pump energy is 21 mJ per pulse with a peak power of 10.6 W. At 100 Hz, the average power is then 2.12 W. An important feature is that the repetition rate of the Q-switched laser is controllable and dictated by the trigger circuit for the pump diode. We have therefore characterized the Yb:YAG laser operation as a function of repetition rate.

The generated spectra are measured with an optical spectrum analyzer (OSA) AQ6317B with a resolution of 50 pm. The pulse width (FWHM) is measured with a Melles Griot detector 13DAH001 with a bandwidth of 3

GHz and an oscilloscope WaveSurfer 104Xs with a bandwidth of 1 GHz. The optical spectrum of the passively Q-switched laser output is centered at 1029.94 nm with a full width at half maximum (FWHM) of 0.33 nm measured at a repetition rate of 100 Hz, as shown in Fig. 5.7(a). The linewidth is measured with no frequency selective element inserted in the cavity. Varying the repetition rate from 10 Hz to 180 Hz, the center wavelength is found to fluctuate in the range of 1029.94-1030.68 nm (shown in inset of Fig. 5.7(a), while the emission bandwidth remains constant. In the long term, the laser will benefit from a frequency selective element locking the output spectrum and center wavelength, e.g. an etalon or a volume Bragg grating.

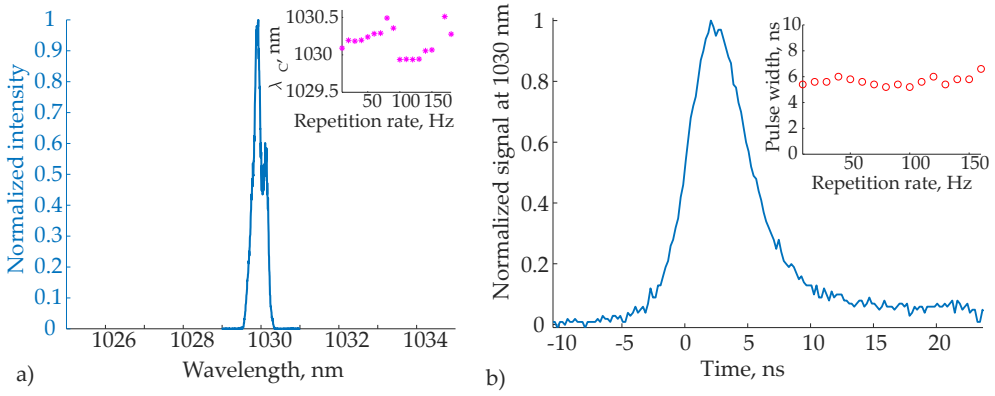


Figure 5.7: a) Spectrum of the 1030 nm output centered at 1029.94 nm with a FWHM of 0.33 nm measured at 100 Hz; inset: center wavelength as a function of repetition rate; b) pulse profile of the 1030 nm with a FWHM of 5.4 ns; inset: pulse width of the 1030 nm as a function of repetition rate.

The temporal pulse shape of the 1030 nm output is shown in Fig. 5.7(b). The FWHM is 5.4 ns. The peak power at 1030 nm is then in the range of 25 to 36 kW at 10 to 180 Hz assuming a Gaussian pulse shape. The pulse width fluctuates about 6.8% when changing the repetition rate, however, without any clear correlation to the repetition rate, see the inset in Fig. 5.7(b).

The pulse energy at 1030 nm monotonously increases from 142 µJ at 10 Hz to 204 µJ at 180 Hz, as shown in Fig. 5.8(a), dark blue circles. The pulse energy is calculated from measured average power. We believe the reason of the pulse energy growing with the repetition rate is the following. With increasing repetition rate, the thermal load increases and the crystal temperature rises because of higher incident pump energy. The stimulated emission cross-section of the laser medium decreases with temperature [95], which is experimentally confirmed in [95, 96, 97]. According to these references, higher population inversion is needed to reach the threshold, hence a pulse with higher energy is emitted. This explanation was also confirmed by measurement of the the delay time of the Q-switched pulse relative to the leading edge of the pump diode pulse: the delay time increases with higher repetition rate, thus with the higher thermal load, so that the Q-switched pulse is emitted later, which can be seen in Fig. 5.8(b). With the increased delay time, more pump energy is stored in the gain medium before the emission of the pulse, corresponding to larger pump energy threshold, resulting in larger pulse energy of the Q-switched pulse. Interestingly, starting approximately at a the repetition rate of 130 Hz the Q-switched pulse is emitted after the end of the pump diode pulse. Another effect which could reduce the pulse

energy, is the temperature dependence of the SA transmission. However, it has been demonstrated that this effect is negligible [98].

The upper lasing limit of our system is 250 Hz, which corresponds to an incident pump power of 5 W and a pump diode duty cycle of 50-60%. Operation at higher repetition frequencies is hampered by the thermal load on the laser crystal. Therefore, the Q-switched laser operation with continuous pumping cannot be obtained because of a too high thermal load. At the same time, there is no lower limit of the laser repetition rate. The system can emit single Q-switched pulses on demand using single pump pulses. Potentially, the repetition rate operation range can be extended by improving the thermal design of the system.

The interesting fact that a Q-switched pulse is also emitted after the pump pulse terminates, can be explained with the following. In a passively Q-switched laser, it takes time to build up a pulse from the spontaneous emission. The pulse build-up time depends on the pump power and gain efficiency. The pulse build-up times in a passively Q-switched systems were simulated in [99] and can reach several microseconds. Another suggestion is the thermal stabilization of the thermal lensing in the laser crystal. However, the complete understanding would require further investigation.

Interestingly, it is experimentally observed that the acceptable pump energy range is rather narrow. A slight increase of the pump energy above the pump energy threshold results in emission of double Q-switched pulses. The reason being that the employed saturable absorber has a long relaxation time so that is relaxes slowly [100].

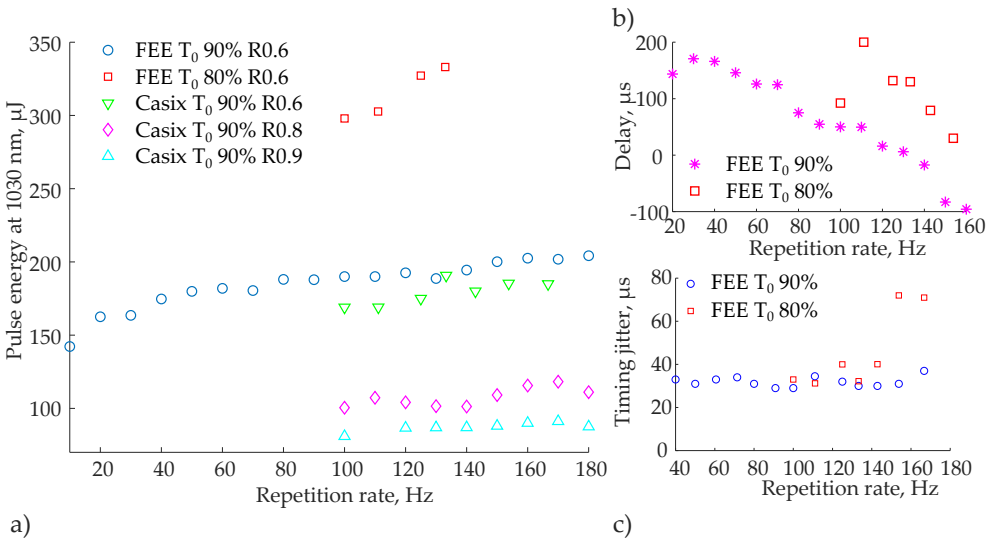


Figure 5.8: a) Pulse energy of the 1030 nm output as a function of repetition rate, employing following SA crystals: from FEE with $T_0$ of 90% and 80% (blue circles and red squares, respectively), from Casix with $T_0$ of 90% (green triangles), all with the OC of R0.6, M3.33; from Casix with $T_0$ of 90%, with the OC of R0.8 and R0.9 (magenta rhombs and light blue triangles), all M3.33; b) delay of the emitted Q-switched pulse relative to the negative edge of the pump pulse for SA from FEE with $T_0$ of 90% and T80%, respectively; c) timing jitter as a function of repetition rate for SA from FEE with $T_0$ of 90% and 80%, respectively.

Figure 5.8(a) also shows the pulse energy at 1030 nm with different SA crystals. With the SA from FEE with $T_0$ of 80%, the pulse energy increases

from 298 µJ to 333 µJ in the repetition rate range from 100 Hz to 133 Hz (red squares). The pulse energy for $T_0$ of 80% is higher than that with a $T_0$ of 90% approximately by a factor of 1.6. However, the laser operation was rather unstable, as described above. The timing jitter fluctuates considerably with the repetition rate, shown in Fig. 5.8(c). With the SA from Casix with a $T_0$ of 90% and using an OC of R0.6, the obtained pulse energy is only marginally inferior compared to that with SA from FEE with a $T_0$ of 90%. With higher OC reflection of R0.8 and R0.9, the obtained pulse energy is in the range from 101 µJ to 120 µJ and from 81 µJ to 91 µJ, respectively.

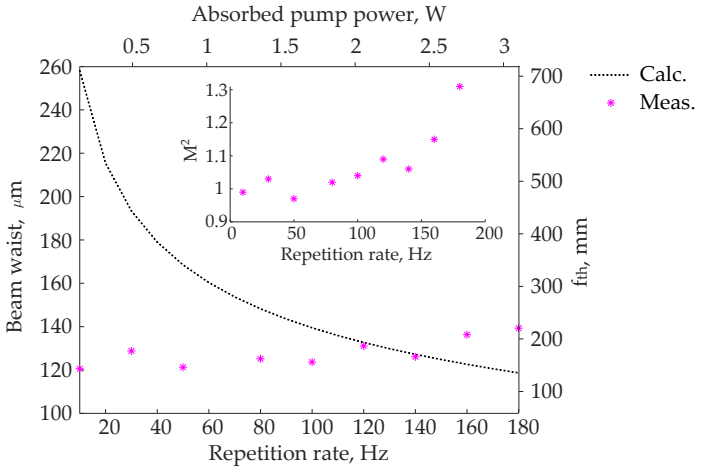


Figure 5.9: Laser beam waist and focal length of the thermal lens as a function of the repetition rate and absorbed pump power, measured (magenta dots) and calculated theoretically with constant fractional thermal load (dotted curve). The inset figure shows the measured $M^2$ value as a function of the repetition rate.

The beam waist size as a function of repetition rate is measured in the Q-switched regime with a 4f lens setup using the knife-edge method, shown in Fig. 5.9. Moreover, the beam quality parameter, $M^2$ is determined by measuring the beam size at several axial positions and calculating the far field divergence angle. Interestingly, the beam waist does not change significantly and is in the range from 121 µm at 10 Hz to 139 µm at 180 Hz. The beam waist is not larger at low repetition rates, but smaller. Then, the beam waist slightly increases at higher repetition rates. The beam waist and thermal lens calculated theoretically are shown in Fig. 5.9, dotted black curve. The curve is explained in the following. At a repetition rate in the range from 10 to 180 Hz, the laser diode duty cycle changes from 0.02 to 0.36, corresponding to an absorbed pump power in the range from 0.1 W to 3 W (with constant pump pulse duration). Thus, using Eq. 5.1 with a constant fractional thermal load, the beam waist is significantly larger at very low repetition rates due to small pump power, as predicted by the resonator geometry with an intracavity lens. However, this is not confirmed experimentally. We believe, this is because the fractional thermal load decreases with increasing repetition rate. The fractional thermal load is a function of the laser extraction efficiency, which increases at higher pump power and higher repetition rates. Thus, the fractional thermal load increases with decreasing repetition rate. This means, that the fractional thermal load is very high at low pump power, resulting in strong thermal lens. The thermal lens

actually is weaker for higher pump power. At the same time, the beam quality, $M^2$ decreases with higher thermal load, from nearly 1 at 10 Hz to 1.3 at 180 Hz. Interestingly, it was reported that in passively Q-switched lasers based on a laser medium with higher lying energy levels (above the upper energy level) and thus experiencing energy-transfer upconversion (ETU), the fractional thermal load increases with decreasing repetition rate [101]. An example of such a medium is the Nd:YAG crystal. The ETU process reduces the population inversion and leads to a loss that increases the temperature of the crystal. The Yb:YAG laser medium does not have ETU loss due to absence of higher energy levels, above the upper laser level. However, in a quasi-three-level laser, the reabsorption increases the threshold and impacts the thermal load significantly, as discussed in Section 5.1.3.

For pump-modulated Q-switched operation, the laser extraction efficiency depends not only on the laser operating point, but in addition on the pump pulse duration. In turn, the pump efficiency is also a function of the ratio between the pump pulse duration and the upper state lifetime of the laser crystal. For good pump efficiency, the ratio has to be lower than 0.2 [100]. However, in this work the long pump pulse duration (2 ms) is dictated by the laser diode current, limited to 12 A, and the laser threshold energy.

## 5.2 THIRD HARMONIC GENERATION

The laser at 343 nm is obtained by third harmonic generation of the 1030 nm emission of the Yb:YAG passively Q-switched laser. The third harmonic is obtained by a cascaded nonlinear process: first, second harmonic generation, and secondly, sum frequency generation. As discussed in Chapter 1, passively Q-switched lasers at 343 nm lasers have not yet been reported. The existing lasers at 343 nm are obtained with mode-locked solid state lasers or laser amplifiers. Therefore, the objective of this section of the thesis is to develop, investigate and characterize cascaded nonlinear generation of 343 nm with a passively Q-switched solid-state laser. We aim to achieve good conversion efficiency and stable operation at 343 nm.

### 5.2.1 *The model*

The fundamentals of nonlinear frequency conversion processes are not given here and can be found for example in [102, 103, 104]. Instead, we present a mathematical description of the model employed for the calculations. The derivation of the model is also found in the mentioned literature. Here, the starting point is as follows. In the first stage, a single-frequency (monochromatic) laser with frequency $\omega_1$ propagates through the first nonlinear crystal and is partially converted to the second harmonic generation (SHG) field with frequency $\omega_2$. In the second nonlinear crystal, the interacting fields with frequencies $\omega_1$ and $\omega_2$, respectively, generate the new field with the resulting frequency $\omega_3$ (i.e. 343 nm). The nonlinear crystals are optical crystals displaying a second-order nonlinear polarization response to applied electromagnetic fields. The crystals nonlinearity is characterized by the second-order susceptibility tensor. The process is depicted schematically in Fig. 5.10. For these processes, the energy and momentum conservation laws

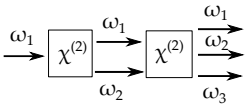


Figure 5.10: Scheme of the cascaded nonlinear process.

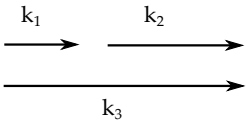


Figure 5.11: The momentum conservation.

are valid. The energy conservation law states that $\hbar\omega_3 = \hbar\omega_1 + \hbar\omega_2$. Thus, for the first process, SHG: $\omega_2 = 2\omega_1$, and for the second, sum frequency generation (SFG): $\omega_3 = \omega_1 + \omega_2 = 3\omega_1$. The momentum conservation law for collinear interaction states $\hbar k_3 = \hbar k_1 + \hbar k_2$ and is depicted in Fig. 5.11. The momentum conservation corresponds to the phase matching condition which is discussed later.

The numerical model used to predict the SHG and THG conversion efficiencies is based on the coupled wave theory which is described below [102]. The field amplitudes vary slowly with distance and time. The interacting fields are sufficiently narrow to be treated as monochromatic. The Rayleigh range of 1030 nm laser beam is 73 mm in free space (with the beam waist of 123.7 µm, measured at 100 Hz and magnified by 1.25) and 117 mm in an LBO crystal. The SHG beam is focused to have the same Rayleigh range. Thus, the nonlinear crystal lengths, 15 mm and 20 mm, are much shorter than the confocal parameter (twice the Rayleigh length). Therefore, the plane wave approximation is valid. For focused beams, the divergence should be taken into account, which increases the phase mismatch. Thus, there can be an optimum of the focusing [105]. Using the plane wave approximation (large beam size), and considering quasi-stationary fields (long temporal pulses) we calculate SHG and SFG power conversion efficiencies by integration of temporal pulses. Furthermore, the beam walk-off and the fundamental wave depletion are included in the SFG calculations. The measured values of beam size, peak power and pulse duration of the fundamental 1030 nm beam are used as input parameters in the model.

The coupled wave theory describes the energy flow between the interacting fields:

$$\begin{aligned}
\frac{da_{\omega_1}}{dz} &= iKga_{\omega_3}a^*_{\omega_2}exp(i\Delta kz) - \frac{\alpha_1 a_{\omega_1}}{2} \\
\frac{da_{\omega_2}}{dz} &= iKga_{\omega_3}a^*_{\omega_1}exp(i\Delta kz) - \frac{\alpha_2 a_{\omega_2}}{2} \\
\frac{da_{\omega_3}}{dz} &= iKga_{\omega_1}a_{\omega_2}exp(-i\Delta kz) - \frac{\alpha_3 a_{\omega_3}}{2}
\end{aligned} \tag{5.9}$$

where $a_{\omega_1}$, $a_{\omega_2}$, and $a_{\omega_3}$ are variables equal to the square root of the photon flux $\phi_{\omega_i}$ at the light frequency $\omega_i$, so that $|a_{\omega_i}|^2 = \phi_{\omega_i}$, $i = 1..3$; K is the prefactor defined in [102], g is the gain parameter defined as $g = \epsilon_0\chi^{(2)}_{eff}\sqrt{\frac{1}{2}\eta^3\hbar\omega_1\omega_2\omega_3}$, $\chi^{(2)}_{eff}$ is the second-order effective susceptibility, $\eta$ is the impedance parameter $\eta = \sqrt{\frac{\mu}{\epsilon}}$; $\Delta k$ is the phase mismatch $\Delta k = k_3 - (k_1 + k_2)$, and $\alpha_1$, $\alpha_2$ and $\alpha_3$ are the absorption coefficients of the nonlinear medium at the light frequencies $\omega_1$, $\omega_2$ and $\omega_3$. K is 1/2 for the SHG and 1 for SFG.

The variables $a_{\omega_i}$, where $i = 1..3$, are related to the power $P_i$ as:

$$a_{\omega_i} = \sqrt{\frac{2P_i}{\omega_i\hbar\pi w_i^2}} \tag{5.10}$$

where $w_i$ is the beam size of the field with frequency $\omega_i$.

For the SHG process, the first two fields are identical, so that only two frequencies take part in the interaction. The coupled wave equations in Eq. 5.9 are then reduced to two coupled equations.

The temporal distribution of the interacting fields is included as follows. The temporal shape of the fields is approximated by a discrete, step-wise Gaussian shape with a measured pulse width (FWHM). For each step the conversion efficiency is calculated with the coupled wave equations. The temporal shape of a Gaussian pulse is defined as

$$P_i(t) = P_{0i} e^{\left(\frac{-4\ln 2 \cdot t^2}{\tau_i}\right)} \tag{5.11}$$

where $P_{0i}$ is the amplitude of the pulse, and $\tau_i$ is the pulse width (FWHM). The temporal Gaussian fields are then included in Eq. 5.9. Then, the fields are integrated over time.

For the SFG, we introduce a walk-off factor $I_b(z)|_{w_0}$ as a multiplication factor into the coupled wave equations in Eq. 5.9. The walk-off factor is calculated as the spatial convolution of the interacting beams $I_{\omega_1}(x, y, z)$ and $I_{\omega_2}(x, y, z)$, whereas the latter, the 515 nm laser beam, $I_{\omega_2}(x, y, z)$ is translated in the transverse direction (e-polarized). In Eq. 5.9, the 515 nm field $a_{\omega_2}$ is multiplied by the z-dependent walk-off factor:

$$I_b(z)|_{w_0} = \iint I_1(s, t, z) I_2(s - x, t - y, z) ds dt. \tag{5.12}$$

The walk-off factor is defined at one fundamental beam size $w_0$.

The SHG conversion efficiency is defined as the power of the generated field, $P_2$ relative to the input field, $P_1$: $\eta_{SHG} = \frac{P_2}{P_1}$. Similarly, the third harmonic generation (THG) conversion efficiency is defined as the power of the generated field, $P_3$ relative to the input field, $P_1$: $\eta_{THG} = \frac{P_3}{P_1}$.

### 5.2.2 *Crystals and phase matching*

Since the interacting fields are collinear (scalar phase matching), we treat the wave vectors as scalar quantities. The phase matching condition has to be fulfilled for efficient nonlinear conversion. There are several methods to achieve phase matching: birefringent, non-critical, and quasi-phase matching (QPM). Birefringent phase-matching is achieved using the dependence of the materials extraordinary refractive index on the direction of propagation in combination with the polarization directions of the interacting fields. Since the phase matching in this case depends on the angle of propagation, it is also called critical phase matching. In the non-critical phase matching (NCPM), the interacting fields propagate along a principal axis of the crystal and the phase matching is achieved through the temperature dependency of the refractive indices. In quasi-phase matching, a high voltage field is applied to a nonlinear crystal to create a periodic (sometimes aperiodic) structure with alternating dipole directions, thus compensating for the accumulated phase mismatch. Quasi-phase matching is sometimes called type 0 phase matching, because all interacting fields are polarized in one direction.

Critical phase matching is commonly divided into two schemes. In a type I phase matching scheme, the input fields have the same polarization and

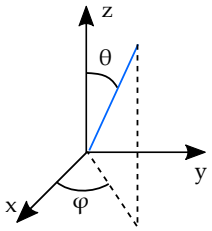


Figure 5.12: Coordinate system of a uniaxial crystal.

are polarized orthogonal to the generated field (oo-e or ee-o, o and e is for ordinary and extraordinary refractive index, respectively). In a type II phase matching scheme, the input beams are polarized orthogonal to each other (oe-o, oe-e). For critical phase matching, the extraordinarily polarized interacting fields experience walk-off, which can reduce the conversion efficiency significantly. In the case of perfect phase matching, $\Delta k = 0$. For SHG, we have $\Delta k = k_2 - 2k_1$. For SFG, $\Delta k = k_3 - (k_1 + k_2)$.

In an anisotropic crystal, the propagation of a light wave is defined by two angles, the polar angle, $\theta$ and azimuthal angle, $\phi$. The coordinate system of a uniaxial crystal is shown in Fig. 5.12. The geometry of a biaxial anisotropic crystal is much more complicated than for its uniaxial counterpart [106]. A thorough discussion of a biaxial crystal geometry with mm2 group (LBO, KTP) can be found in [107].

The most relevant parameters when selecting a nonlinear crystal for an application include: nonlinearity coefficient, damage threshold, and acceptance bandwidths (spectral, angular, and temperature). The acceptance bandwidths are dictated by the material parameters and define the tolerance of the phase matching condition, i.e. angle acceptance bandwidths limit the maximum focusing in a nonlinear crystal. A summary of parameters of several nonlinear crystals for SHG is shown in Table 5.4. It includes LBO in a NCPM configuration, KTP for type II interaction, and 5%MgO:$LiNbO_3$; the latter can be employed as bulk crystal (NCPM) and periodically poled (PP). Firstly, a PP MgO:$LiNbO_3$ crystal (PPLN) can be employed for a quasi-phase matching scheme. In this case, the highest nonlinear coefficient, $d_{33} = 25$ pm/V is accessed, when all interacting fields are polarized in one direction. The $d_{eff}$ is then $(2/\pi d_{33}) = 16$ pm/V. The required poling period would be about 6.3 µm. The additional advantages include the use at room temperature and with no walk-off. The laser beams polarized in one direction can then be phase matched in the second crystal with a type I scheme. The major drawbacks of PPLN crystals are cost and lower damage threshold compared to bulk MgO:$LiNbO_3$. A PPLN crystal damage was reported with 100 MW/cm$^2$, or 2 J/cm$^2$, of 1064 nm, 10 ns pulses [108]. In contrast, the LIDT of the bulk crystal is >600 MW/cm$^2$ [109]. Therefore, a PPLN crystal cannot be used for the high power Q-switched laser. Secondly, a KTP crystal used in a type II configuration (o-oe) has high $d_{eff}$ of 1.9 pm/V. However, the phase matching configuration dictates that the 1030 nm field has to be polarized at 45°. This introduces losses because a part of the 1030 nm cannot be used in the second nonlinear stage. Moreover, the walk-off is present. Thirdly, a bulk 5%MgO:$LiNbO_3$ has a high nonlinear coefficient of 4.65 pm/V, high damage threshold, and can be operated in a noncritical phase matching scheme at room temperature, thus experiencing no walk-off. No walk-off is a significant advantage for the subsequent conversion in the second nonlinear stage. Moreover, the crystal is cost-effective and does not require an oven, only a TEC plate. The two nonlinear crystals, for SHG and SFG, respectively, can be combined at one common TEC plate kept at room temperature, resulting in a compact system. The fundamental beam (1030 nm) can then be focused into both crystals simultaneously. No relay lenses are needed between the nonlinear crystals. The mentioned arguments make the bulk 5%MgO:$LiNbO_3$ our optimal crystal chosen for the SHG of 1030 nm.

Table 5.4: Summary of crystal parameters for the SHG of 1030 nm: orientation angles (θ, ϕ), phase matching temperature ($T_{PM}$), effective nonlinear coefficient ($d_{eff}$), and walk-off angle (ρ).

| Parameter | LBO | KTP | 5%MgO:$LiNbO_3$ | |
|---|---|---|---|---|
| | | Flux-gr. | Bulk | PP |
| Configuration | NCPM | Type II | NCPM | Type 0 |
| | oo-e | oe-o | oo-e | ee-e |
| Orientation | along x | YZ | | |
| θ, deg | 90 | 75.6 | 90 | 90 |
| ϕ, deg | 0 | 90 | 0 | 0 |
| $T_{PM}$, °C | 193 | 20 | 24.2 | 20 |
| LIDT, GW/$cm^2$ | >1 at 1064 nm | 0.9-1.0 [110] | 0.6 [109] | <0.1 [108] |
| (1064 nm, 10 ns) | >0.24 at 532 nm | | | |
| | >0.2 at 355 nm [111] | | | |
| | 25 [112] | | | |
| Fluence, J/$cm^2$ | | | | <2 [108] |
| (1064 nm, 10 ns) | | | | |
| $d_{eff}$, pm/V | 0.85 [113] | 1.4 [114] | 4.65 [115] | 16 |
| ρ, deg | - | 1.8 [106] | - | |
| Δθ; Δϕ, deg·cm | 3.54; 2.57 [116] | 0.11 [117] | 0.063 [109] | |
| ΔT, °C·cm | 3.9 [116] | | | |

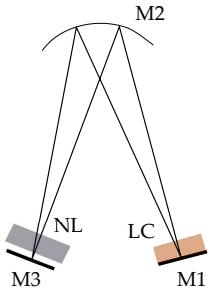


Figure 5.13: The intracavity setup: LC - Nd:YAG, M1 - HR@1064 nm, M2 - HR 99.9% @ 1064 nm, M3 - HR @ 1064 nm & 532 nm, NL - MgO:$LiNbO_3$.

However, during the experiment employing a 5%MgO:$LiNbO_3$ crystal, an insurmountable challenge is encountered. It is known that the doping level of MgO influences the phase matching temperature significantly. Two nominal 5%MgO:$LiNbO_3$ crystals from different vendors (an unknown vendor and Lambda Photonics) are tested with the developed Q-switched 1030 nm laser in a single pass and with a CW Nd:YAG laser at 1064 nm in an intracavity setup. The latter is shown in Fig. 5.13. For crystal 1, the phase matching temperature for the 1064 nm beam is experimentally determined to be 70°C. However, the phase-matching temperature for the 1030 nm laser with crystal 1, and for both the 1030 nm and 1064 nm beams with crystal 2 is not found within the temperature range of 14°C-100°C.

In addition, there is a discrepancy of the Sellmeier coefficients for crystal 5%MgO:$LiNbO_3$ reported in literature. The phase-matching temperature is calculated using the temperature-dependent Sellmeier coefficients from Gayer [118] and with the SNLO software [119]. In SNLO, the Sellmeier coefficients for 5%MgO:$LiNbO_3$ are from Zelmon [120]. The thermal coefficients are said to be from [121], however, no thermal data is found in that reference. Thus, the temperature dependence in the SNLO software is based on an unknown source. Table 5.5 summarizes the results. According to [118], the phase-matching temperature $T_{PM}$ of 5%MgO:$LiNbO_3$ is at 52.9°C and 24.2°C for the SHG at 1064 nm and 1030 nm, correspondingly. According to [119], the phase-matching temperature is 110°C and 23°C for the SHG at 1064 nm and 1030 nm, correspondingly. To the authors best knowledge, there are no reports on bulk MgO:$LiNbO_3$ used for the conversion of 1030 nm (only PPLN). Considering that the difference in the phase matching tem-

peratures for the 1064 nm and 1030 nm is 87°C [119], the phase matching temperature of crystal 1 for 1030 nm is probably below 0°C.

Table 5.5: Phase matching temperature ($T_{PM}$) for 5%MgO:$LiNbO_3$ crystal: 1) calculated based on different sources; 2) measured.

| Ref. | $T_{PM}$ for 1064 nm, °C | $T_{PM}$ for 1030 nm, °C |
|---|---|---|
| Calculated | | |
| [119] | 110 | 23 |
| [118] | 52.9 | 24.2 |
| This work. Experimental 5%MgO:$LiNbO_3$ | | |
| Crystal 1 | 70 | None* |
| Crystal 2 | None* | None* |
| Experimental 5%MgO:$LiNbO_3$ | | |
| [109] | 107 | |

*Not observed in the temperature range of 14°C-100°C.

In the following, we explain how the growth of MgO:$LiNbO_3$ influences the phase matching temperature and why it is important. The growth process of MgO:$LiNbO_3$ crystals is by no means an easy task. Most grown $LiNbO_3$ crystal are congruent, which means the melt and solid phases are in the same position. A stoichiometric $LiNbO_3$ crystal has one Li ion for each Nb ion. However, congruent crystals are deficient in lithium and typically have 48.6%-48.7% of $Li_2O$ which corresponds to the Li to Nb ratio of 0.94. They are grown by means of the Czochralski technique. If required, a stoichiometric $LiNbO_3$ can be grown by a continuous refreshing of the melt with lithium. For any other than congruently grown crystal, the melt and solid concentrations differ. The phase matching temperature depends both on the $Li_2O$ content and the MgO content. Figure 5.14 shows the dependence of $T_{PM}$ for 1064 nm with MgO in the range of 4.5-9%, constructed based on [122]. The $Li_2O$ content varies from 48.5% to 48.9%, however the dependence is not strong, so that the curves overlap. In turn, the phase matching temperature decreases from 116°C to 10°C with the MgO content in the range from 4.8% to 9%. With the MgO content below 3%, the phase-matching temperature decreases [122]. For a congruent $LiNbO_3$ crystal with no MgO, the $T_{PM}$ is at −66°C [123]. Therefore, a nonlinear crystal requires high precision of the MgO doping level, in order to obtain the phase matching temperature in the required range. However, it was communicated by a few crystal vendors that it is not possible to control the doping level of MgO with the required precision. Caused by the growth technique, a grown crystal might have a MgO content that is different in the front part and the rear part of the crystal, resulting in an unpredictable modification of the phase matching temperature.

To conclude, the growth a MgO:$LiNbO_3$ crystal with the required doping level and thus required $T_{PM}$ is very difficult to achieve. The phase matching temperature depends on the melt stoichiometry and the MgO doping level, thus special care should be taken when selecting a MgO:$LiNbO_3$ crystal. As mentioned, bulk MgO:$LiNbO_3$ has not been reported for the SHG of 1030 nm (only PPLN). At the same time, LBO in the NCPM scheme has been reported often for this application [75, 124, 125, 126].

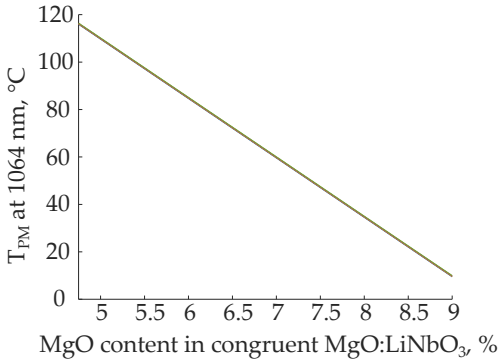


Figure 5.14: Non-critical phase matching temperature of 1064 nm in a congruent MgO:$LiNbO_3$ crystal as a function of the MgO content. The $Li_2O$ content varies in the range from 48.5% to 48.9%, curves overlap. Constructed based on data from [122].

Thus, an LBO crystal in the NCPM configuration is the preferred choice for SHG of 1030 nm. LBO has a rather low nonlinear coefficient of 0.85 pm/V [113], however sufficient conversion efficiency can be obtained with a long crystal benefiting from relatively large acceptance bandwidths. The angular acceptance bandwidths are 3.54 deg·cm and 2.57 deg·cm [116], respectively, and the temperature bandwidth is 3.9 °C·cm [116]. The temperature bandwidth has also been reported: 10.1°C·cm [127] and 6.2°C·cm [128]. The $d_{eff}$ is calculated as follows [107]: for the XY plane, and oo-e interaction, $d_{ooe} = d_{32}\cos\phi$, where $d_{32}$ is 0.85 pm/V [113]. The advantages of LBO include no walk-off due to the NCPM configuration and high damage threshold. However, the usage of an additional lens system between the nonlinear crystals is now necessary since the first LBO crystal has to be placed in an oven to maintain a temperature of 193°C.

Moving on to SFG step, we consider the second nonlinear crystal. A comparative summary of potential crystals for the SFG of 1030 nm and 515 nm is shown in Table 5.6. Based on the selection of LBO (NCPM) for the SHG, the SFG crystal phase matching scheme is required to be type II, in order to avoid the insertion of extra polarizing components. LBO crystal was chosen, due to significantly larger angular bandwidths and a smaller walk-off angle. Moreover, it has high damage threshold, and can be operated at room temperature. The $d_{eff}$ for YZ plane, oe-o interaction, is calculated as [107]: $d_{oeo} = d_{31}\cos\theta$, where $d_{31}$ is 0.67 pm/V [113]. LBO absorption coefficients $\alpha_1$, $\alpha_2$ and $\alpha_3$ are 0.1 $m^{-1}$, 0.3 $m^{-1}$, and 3.1 $m^{-1}$ at 1030 nm, 515 nm and 343 nm, respectively [111].

It was reported that acceptance bandwidths in nonlinear crystals can be increased by a walk-off compensation, i.e. combining crystals with opposite birefringence-induced walk-off directions [132]. This in turn can result in an improved conversion efficiency. In this work, we attempted to use the LBO crystals with lengths of 10 mm and 20 mm to implement the walk-off compensation. However, it was not possible to obtain positive results due to limited mechanical stability of our system. For the walk-off compensation, better mechanical mounts are required with more precise position control.

Recently, novel ferroelectric structures have been developed: PP-LBGO in QPM configuration for the SHG stage to generate 355 nm [133], and mono-

Table 5.6: Summary of crystal parameters for the SFG of 1030 nm and 515 nm: orientation angles ($\theta$, $\phi$), effective nonlinear coefficient ($d_{eff}$), walk-off angle ($\rho$). All at the room temperature.

| Parameter | LBO | | BiBO | BBO | |
|---|---|---|---|---|---|
| Conf. | type I | type II | type I | type I | type II |
| | oo-e | oe-o | ee-o | oo-e | oe-e |
| Orient. | XY | YZ | YZ | | |
| $\theta$, deg | 90 | 50.1 | 143.44 | 32.25 | 38.2 |
| $\phi$, deg | 40.1 | 90 | 90 | 90 | 90 |
| $\rho$, deg | 0.99 [112] | 0.54 [112] | 3.8 [129] | 4.1 [112] | 4.5 [112] |
| $d_{eff}$, pm/V | 0.67 [127] | 0.53 [113] | 3.1 [129] | 1.57 [127] | 1.41 [127] |
| LIDT, GW/cm$^2$ (10 ns) | See Table 5.4 | | 4.7 [129] (0.0035 ns) | 15.6 [112] | |
| Ang. band., deg·cm | $\Delta\theta$, $\Delta\phi$ | $\Delta\theta$, $\Delta\phi$ | $\Delta\theta$ | $\Delta\theta$ | $\Delta\theta$ |
| | | 0.18 [Calc.] | 0.014 [Calc.] | | |
| | 5.4, 0.1 [112] | 0.31, 6.1 [112] | 0.034 [129] | 0.02 [112] | 0.02 [112] |
| | | 0.29, 4.87 [130] | | | |
| $\Delta T$, °C·cm | 3.8 [128] | 3.7 [128] | 1.1 [129] | 15.5 [131] | 13.3 [131] |

lithic UV generation in a single device using PPMgSLT [134]. This design promotes a compact and elegant system.

### 5.2.3 *Optical setup*

The experimental setup is shown in Fig. 5.15. The second harmonic and the sum frequency generation is obtained with LBO crystals. The infrared beam is magnified by a factor of 1.25 or 2 when focused into the LBO1 crystal (L2). The second harmonic (515 nm) is obtained with a 15 mm long LBO crystal kept at 193°C (LBO1) using NCPM scheme. For the SFG stage both the 1030 nm and 515 nm laser beams, respectively, are focused in the center of a 20 mm long LBO crystal kept at 18°C (LBO2). The 1030 nm and 515 nm beams are designed to have the same Rayleigh range using a magnification of $-1$. Achromatic lenses are used to compensate for the focal shift (L3). The SFG crystal is cut for type II critical phase matching. The crystals orientations are shown in Fig. 5.16. The lens L4 collimates the UV beam. The prism P is placed at Brewsters angle for 343 nm beam.

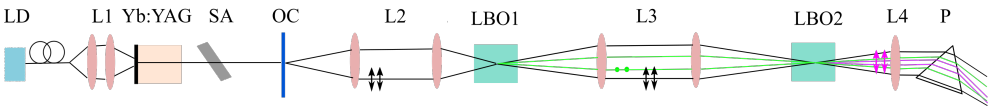


Figure 5.15: Experimental setup including the diode laser (LD), the Yb:YAG laser crystal, the $Cr^{4+}$:YAG saturable absorber (SA), the laser output mirror (OC), lens systems (L1-L4), two LBO crystals and a dispersive prism (P).

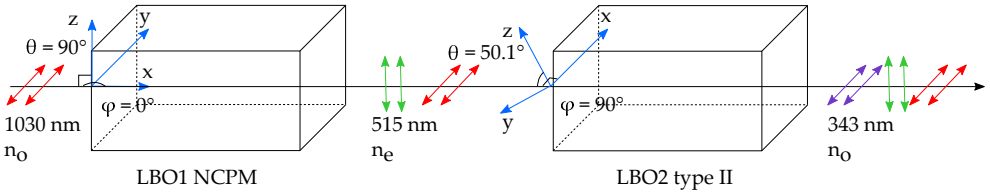


Figure 5.16: Cascaded third harmonic generation of 343 nm with two nonlinear crystals: LBO1 in a NCPM configuration (SHG) and LBO2 in type II configuration (SFG).

### 5.2.4 *Results and discussion*

The calculated SHG conversion efficiency as a function of wavelength is shown in Fig. 5.17(a). For the calculation we used a 15 mm long NCPM LBO crystal at 193°C and a beam radius of 123.7 µm, measured at 100 Hz, see Fig. 5.9. For comparison, the spectrum of the 1030 nm beam is also plotted. The calculated spectral acceptance bandwidth is 1.8 nm which is about five times wider than the bandwidth of the laser emission.

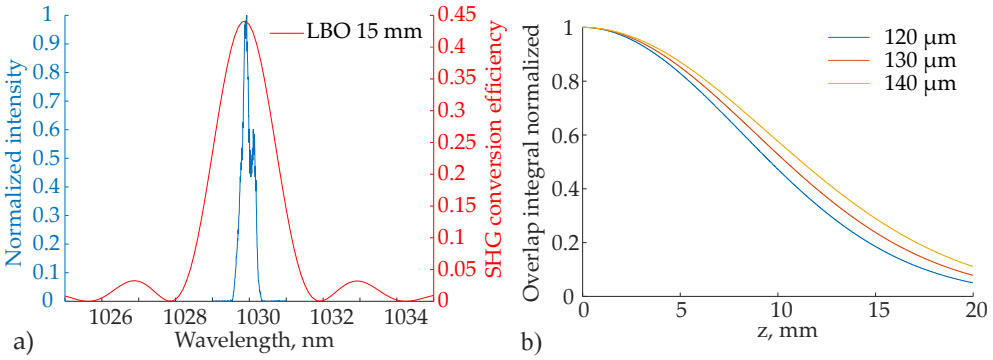


Figure 5.17: a) The calculated conversion efficiency as a function of wavelength with the spectral acceptance bandwidth of 1.8 nm; b) the overlap integral of two Gaussian beams with one of them experiencing walk-off as a function of crystal length. Calculated for LBO crystal of 20 mm, fundamental beam radius of 156 µm, and walk-off angle of 9 mrad.

The optical spectrum of the 515 nm output is centered at 515.28 nm with a FWHM of 0.27 nm, see Fig. 5.18(a). The spectral bandwidth of the 1030 nm and 515 nm beams is rather stable with the repetition rate, see Fig. 5.18(a), inset, although the central wavelength fluctuates. The temporal pulse of the 515 nm output (FWHM of 3.2 ns) is shown in Fig. 5.18(b).

Although the infrared laser operates up to 250 Hz, the harmonic generation is measured only up to 180 Hz. At higher repetition rates, damage of the achromatic lenses L3 is observed. The pulse energy of the 515 nm output increases from 68 µJ at 20 Hz to 87 µJ at 180 Hz. The measured SHG power conversion efficiency exhibits rather constant behaviour in the range of 40-45%, see Fig. 5.19(a), red squares. The pulse energy increase corresponds to the pulse energy increase of the 1030 nm beam. It should be noted, that the SHG crystal angle was slightly readjusted to compensate for the fluctuating center wavelength of the infrared laser for different repetition rates, as shown earlier in the report. See inset in Fig. 5.7(a). The SHG conversion efficiency is calculated to be 44% at 100 Hz and does not change with the repetition rate, see Fig. 5.19(a), magenta dots. We believe this is because

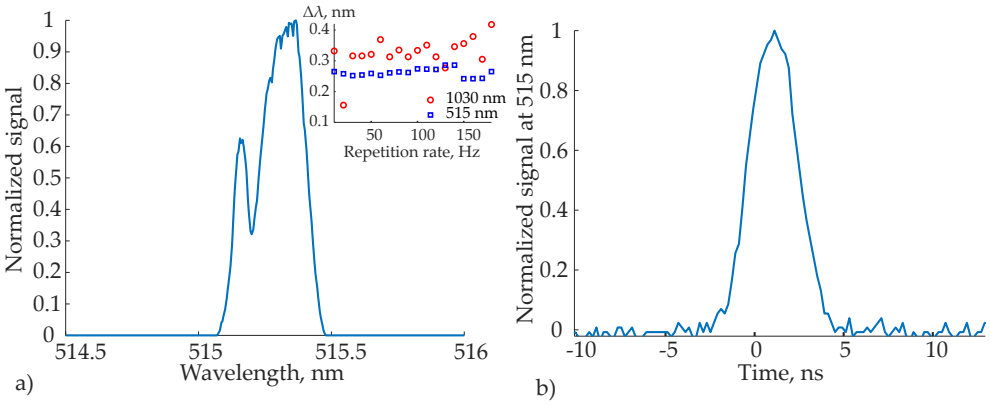


Figure 5.18: a) Spectrum of the 515 nm output centered at 515.28 nm with a FWHM of 0.27 nm; inset: spectral bandwidth of 1030 nm and 515 nm as a function of repetition rate; b) pulse waveform of the 515 nm output with a FWHM of 3.2 ns.

the temporal shape of the fundamental field, 1030 nm, starts to saturate, the beam size remains constant as a function of the repetition rate. The pulse at 1030 nm has a FWHM of 5.4 ns in the model, as measured experimentally. Figure 5.20(a) shows the modeled temporal shapes of the 1030 nm beam before the first crystal LBO1 ($P1_0$, orange), after the first crystal ($P1_1$, yellow), after the second crystal LBO2 ($P1_2$, blue), and the 515 nm beam before the second crystal LBO1 ($P2_1$). It is seen that the 1030 nm beam starts to saturate after the first crystal, LBO1. If the 1030 nm beam size is smaller, the 1030 nm field will saturate in the center, resulting in reduced SFG conversion efficiency. The refractive indices are calculated as in [128] with the temperature dependence found in [127]. The effective nonlinear coefficients are taken from [113]. The calculated temperature acceptance bandwidth is 2.5°C and the angular acceptance bandwidth $\Delta\phi$ is 2°.

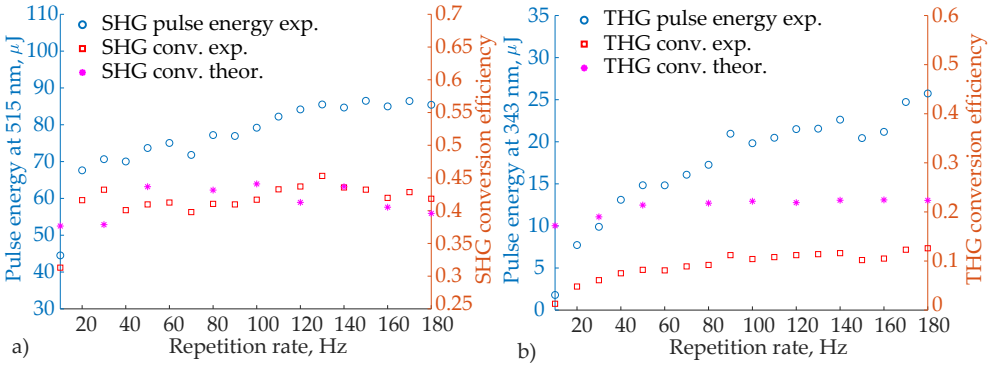


Figure 5.19: a) Pulse energy at the 515 nm output (blue circles), measured (red squares) and theoretically calculated (magenta dots) SHG conversion efficiency as a function of repetition rate; b) pulse energy of the 343 nm output (blue circles), measured (red squares), theoretically calculated (magenta dots) THG conversion efficiency as a function of repetition rate. Magnification M1.25.

The pulse energy of the 343 nm laser increases from 2 μJ at a repetition rate of 10 Hz to 26 μJ at 180 Hz, shown in Fig. 5.19(b). The measured THG conversion efficiency (IR-UV) increases from 1 to 13%. We explain the low conversion efficiency at lower repetition rates as follows. The SHG crys-

tal was not readjusted during the measurement of the SFG measurements. Only the SFG crystal was slightly readjusted to compensate for the center wavelength fluctuations. Thus, the phase matching in the first crystal, LBO1 might be not optimal. The theoretically predicted IR-UV conversion efficiency is in the range from 17% to 22% at a repetition rate from 10 to 180 Hz. The conversion efficiency is 22% at 100 Hz, which is by a factor of 2 higher than measured. This is probably due to a misaligned spatial overlap of the interacting beams, or uncertainty of the nonlinear coefficients. In addition, the beam walk-off is not treated in a precise manner. Figure 5.17(b) shows the calculated overlap integral of two interacting Gaussian beams, 1030 nm and 515 nm. The spatial overlap integral is calculated for different beam sizes of the 1030 nm beam and decreases as the fields propagate through the crystal. The smaller the beam waist, the smaller the overlap is. An additional factor reducing the efficiency can be the angular acceptance bandwidth of the second nonlinear crystal, LBO2. The measured far field angle $\theta_{1/2}$ of the 1030 nm beam is shown in Fig. 5.20(b) as a function of repetition rate. Magnified by a factor of 1.25 (M1.25), the half-angles exceed the acceptance bandwidth of LBO2 (0.075 deg, orange solid line), thus reducing the conversion efficiency.

The temperature acceptance bandwidth is calculated to be 3.1°C and the angular acceptance bandwidth, $\Delta\theta$ is 0.08°. Figure 5.23(a) presents the measured temporal profile of the THG pulse having a FWHM of 2.3 ns. The optical spectrum of the 343 nm output is not measured since it was beyond the spectral range of the OSA available. However, the spectrum of the 343 nm beam results from a convolution of the two interacting beams, 1030 nm and 515 nm. Thus, the FWHM of the UV spectrum is below 0.2 nm.

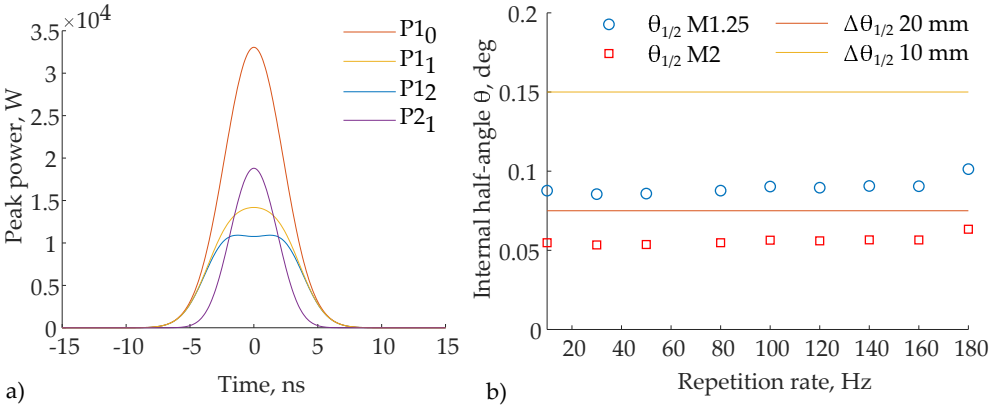


Figure 5.20: a) Calculated temporal shapes of the 1030 nm beam before the first crystal LBO1 ($P1_0$, orange), after the first crystal ($P1_1$, yellow), after the second crystal LBO2 ($P1_2$, blue), and the 515 nm beam before the second crystal LBO1 ($P2_1$). At 100 Hz, beam waist of the 1030 nm is 155 µm in the LBO1 crystal. b) Internal half-angle in LBO of the 1030 nm beam as a function of repetition rate, based on the measured values, magnified by 1.25 (blue circles) and 2 (red squares). Half-angle acceptance bandwidths for LBO crystal of 10 mm (yellow) and 20 mm (orange) are shown.

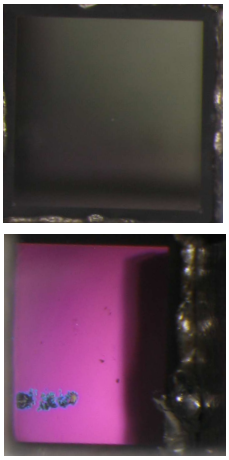

Figure 5.21: Undamaged front surface (above) and damaged rear surface (below) of the LBO1 crystal.

Unluckily, during the experiment damage of the first nonlinear crystal, LBO1 was observed, shown in Fig. 5.21. Most likely, the AR coating was damaged. To avoid further damage, magnification of the 1030 nm beam in

the nonlinear crystal was increased from −1.25 to −2. After that damage was not visual on the surface.

Figure 5.22(a) shows the measured pulse energy (blue circles) of the 515 nm beam using a magnification of −2. The pulse energy, thus the SHG conversion efficiency decreased by nearly factor of 2 compared to the magnification of −1.25. The pulse energy increases in the range of 29 µJ to 50 µJ, and the conversion efficiency (red squares) is rather constant, at 22%. The theoretically calculated SHG conversion efficiency matches very well the measured values.

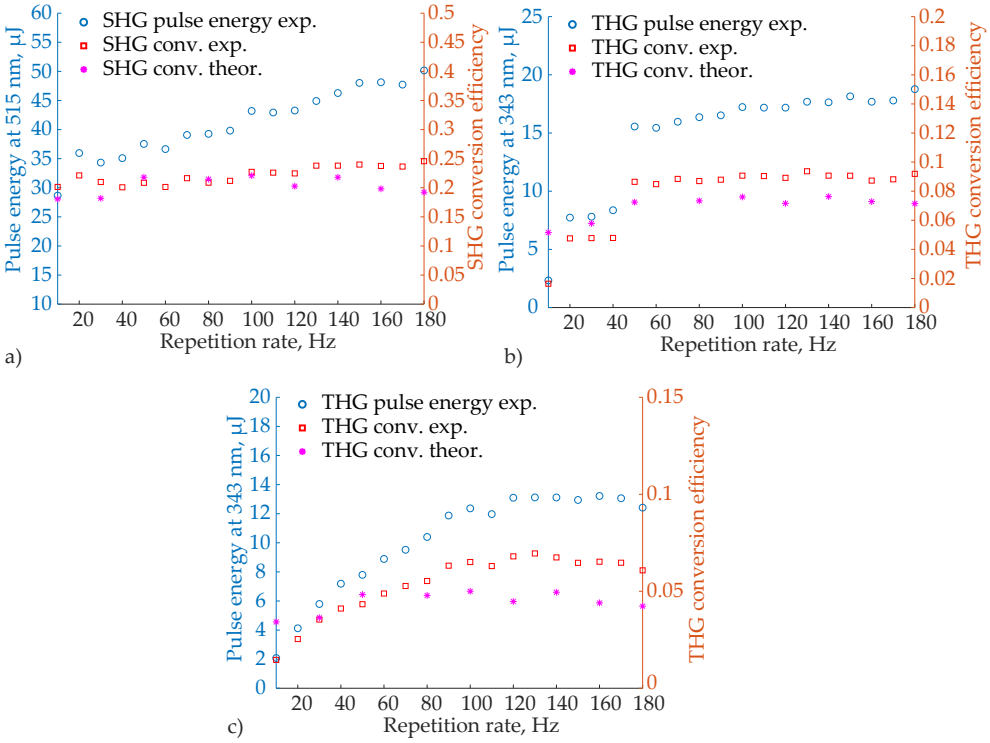


Figure 5.22: a) Pulse energy (blue circles) at the 515 nm output, measured (red squares) and modeled (magenta dots) SHG conversion efficiency, as a function of repetition rate; b) and c) pulse energy (blue circles) of the 343 nm output, measured (red squares) and modeled (magenta dots) THG conversion efficiency, with $LBO_2$ crystal of 20 mm and 10 mm, respectively. Magnification M2.

In turn, the pulse energy of the 343 nm decreased only about by 15%, shown in Fig. 5.22(b). The jumps in the pulse energy are explained by spectral fluctuations of the input beams. The THG conversion efficiency was 9% at 100 Hz, versus 10% with magnification of −1.25. Interestingly, the discrepancy by a factor of 2 between the measured and calculated values in Fig. 5.19(b) is absent in this case. The possible reason is that the far field angles were decreased according to the magnification and are within the angular acceptance bandwidth $\Delta\theta_{1/2}$, see Fig. 5.20(b).

Figure 5.22(c) shows the pulse energy at 343 nm and the THG conversion efficiency measured with the $LBO_2$ crystal of 10 mm. The 343 nm pulse energy is in the range from 2 µJ to 12 µJ (blue circles), and the measured THG conversion efficiency is in the range of 1% to 6% at repetition rate from 10 Hz to 180 Hz. The calculated THG conversion efficiencies is below the

measured values probably due to uncertainty of the nonlinear coefficients, as mentioned before.

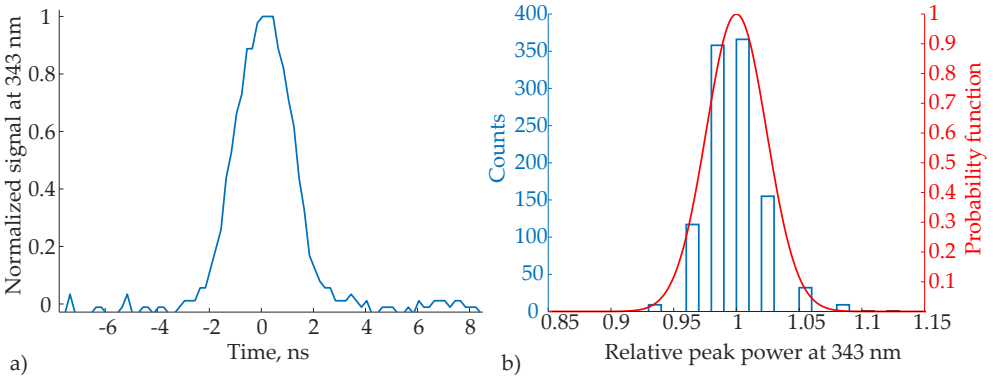


Figure 5.23: a) Pulse waveform of the 343 nm output with a FWHM of 2.3 ns; b) peak power distribution of the 343 nm laser output with a pulse-to-pulse amplitude fluctuation of 2.4% measured with 1048 pulses.

After the collimating lens, L4, the UV beam is measured using the knife-edge method (data shown later). The beam is elliptic with radii of $w_x$ = 1.54 mm and $w_y$ = 0.95 mm, respectively, where $w_x$ and $w_y$ are the $1/e^2$ radii measured. The ellipticity is 1.5. It was observed using a CMOS camera that when changing the LBO2 crystal from 10 mm to 20 mm, the UV beam maintains the same $w_y$, however $w_x$ increases. This means that the elliptic shape of the UV beam is dominated by the beam walk-off effect.

## 5.3 TIMING JITTER AND PEAK POWER FLUCTUATIONS OF THE PASSIVELY Q-SWITCHED LASER

The developed passively Q-switched laser at 343 nm will later be employed in time-resolved measurements for immunoassays. For this measurement technique, excitation and detection are separated in time to avoid fast background fluorescence and exploiting the long lifetime of fluorophores. As discussed in Chapter 2, for immunoassay diagnostics the detection of extremely low light levels is required, and measurements of very low analyte concentrations are of interest. At these low light levels, any noise sources and instabilities are relevant. Timing jitter and peak power fluctuation of the excitation light source contribute as noise sources to the fluorescence measurements. Therefore, in the following section we discuss the different noise sources from the laser source: the timing jitter and peak power fluctuation. We aim to estimate the impact of these noise sources on the fluorescence measurements.

The timing jitter of the 1030 nm pulses was measured relative to the negative edge of the pump pulse, and does not change significantly with the repetition rate, as shown in Fig. 5.8(c). The timing jitter was on average 32.5 µs. Interestingly, the Q-switched pulse moves towards the end of the pump pulse and eventually is emitted after the pump pulse, whereas the timing jitter is nearly the same.

The 1030 nm pulse-to-pulse peak power fluctuation was 1.6% calculated from 1014 measured optical pulses. The histogram and normal distribution curve are shown in Fig. 5.24(a). The Q-switched pulse is emitted approxi-

mately 1.9 ms after the positive edge of the pump pulse (operating at 100 Hz). The timing jitter of the 1030 nm pulses is 32.6 µs which is 0.3% relative to the cycle duration of 10 ms. The 1030 nm timing jitter is measured as the standard deviation of the delay time distribution of 1075 optical pulses, plotted in Fig. 5.24(b). Since the Q-switched pulse is emitted only about 100 µs before the end of the pump pulse, the pulse width fluctuation of the pump is also measured. The standard deviation of the pump pulse width is 2.5 µs. The fall time is 21.5 µs, calculated from an average of 1000 pulses, with a standard deviation of 114 ns. The timing jitter of a passively Q-switched system is fundamentally limited by the spontaneous emission noise [135]. Additional factors include pump pulse fluctuations, resonator mode fluctuations, and temperature fluctuations of the laser medium and consequently the emission wavelength [136, 137, 138, 139]. A few methods of reducing timing jitter of passive Q-switched lasers have been suggested, such as the use of composite pump pulses [137] and bleaching the saturable absorber [138]. In our system, the diode pump pulse amplitude fluctuation was measured to be very low (0.06%).

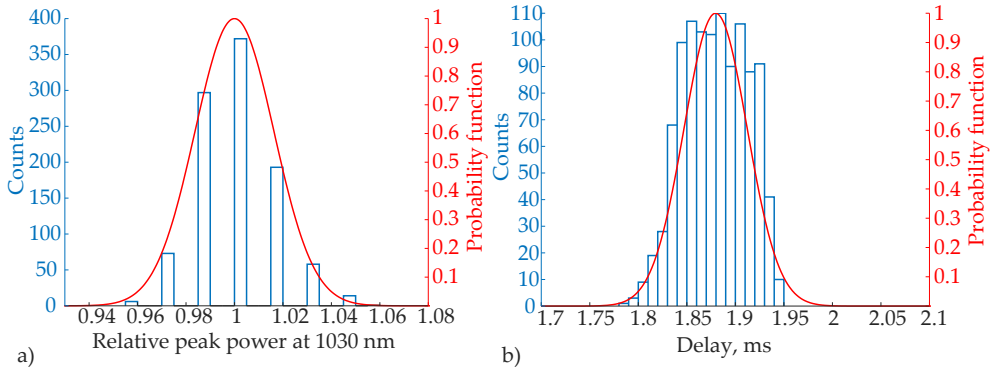


Figure 5.24: a) Peak power distribution of 1030 nm pulses (1000 measurements). The pulse-to-pulse amplitude fluctuation is 1.6%. b) Distribution of delay time of the Q-switched pulse relative to the positive edge of the pump pulse, 1075 measurements, the average value is 1.9 ms, standard deviation is 32.6 µs (variation 1.7%).

The distribution of the 343 pulse peak power values was measured using 1048 pulses, as shown in Fig. 5.23(b). The pulse-to-pulse peak power fluctuation is 2.4%. The accuracy of the peak power measurement is limited by the rise time of the detector. The peak power fluctuation reflects the pulse-to-pulse energy fluctuation as the pulse width does not change at fixed repetition rate.

As mentioned before, the obtained cycle duration of 10 ms matches the decay lifetime of lanthanides which are often used in time-resolved fluorescence spectroscopy. As mentioned, the measured timing jitter is only 0.3% relative to the cycle of the measurement (10 ms) and 3.2% relative to a typical lifetime of europium (1 ms). We calculated the impact of the timing jitter on the collected signal from a fluorophore with a decay lifetime of 1 ms. The timing jitter of 32 µs results in a fluctuation in the range of ±3% of the emitted fluorescence signal, within one standard deviation and ±7% within two standard deviations. Depending on the exact application this noise source can be neglected. For example, in Chapter 4 we show that in a state-of-the-art immunoassay measurement system, the variation from sam-

ple to sample can be up to 6%, and from system to system up to 11%. We note that the noise can be further reduced by signal averaging. For applications requiring higher sensitivity, or when employing short (nanosecond) lifetime fluorophores, the timing jitter noise factor can be avoided by optically triggering the detection circuit. With a peak power fluctuation of 2.4% the collected signal changes within 2.4% as well.

## 5.4 CONCLUSION

A low repetition rate, simple and cost-effective 343 nm solid-state laser source is developed through THG of a passively Q-switched diode-pumped Yb:YAG laser source. At 343 nm, pulse energy of 20 μJ, pulse width of 2.3 ns and operation at a repetition rate of 100 Hz is obtained. The converted light is generated from pulse energy of 190 μJ (1030 nm) and pulse width of 5.4 ns. The conversion efficiency is 10.4% at 100 Hz which is comparable to that obtained with mode locked lasers. The UV laser emits pulses on demand and can be electronically synchronized with a detection circuit. The low repetition rate matches particularly the millisecond scale lifetime of lanthanide fluorophores, targeting applications in fluoroimmunoassays and time-resolved fluorescence spectroscopy. The 343 nm output targets the excitation peak of the lanthanides. To the authors knowledge, this is the first demonstration of 343 nm passively Q-switched solid-state laser.

In addition, the obtained timing jitter can be neglected when using for long fluorescence lifetime (about 1 ms) fluorophores, i.e. lanthanides widely used in fluoroimmunoassays. The timing jitter, however, can be avoided by implementing an optical feedback system. The UV pulse-to-pulse peak power fluctuation is 2.4%. The impact of these noise sources can be further decreased by signal averaging. High spatial beam quality and narrow spectral emission of the laser will allow for further decrease of the unwanted background contributions in fluoroimmunoassay measurements.

# 6

# LASER INDUCED TIME-RESOLVED FLUORESCENCE MEASUREMENTS OF TROPONIN I

In this chapter, we report on the laser-induced time-resolved fluorescence measurements for immunoassays, where the developed laser at 343 nm is used as an excitation source. Only the high-sensitivity troponin I (hsTnI), assay 2 was used in the experiments since it has the highest sensitivity and the best spectral overlap with the laser emission wavelength. In the following, the aim is to investigate the performance of the laser excitation compared to LED excitation.

## 6.1 EXPERIMENTAL SETUP

The experimental setup is shown in Fig. 6.1. The laser setup before the prism P is the same as in Fig. 5.15. The prism is used to spatially separate the 343 nm laser beam from the other interacting laser beams. The prism is inserted at Brewsters angle for the 343 nm beam to minimize the reflection loss. The laser beam was attenuated using a half wave plate (WP) for 343 nm combined with a polarizing beam splitter (PBS). The mirror M3 is a scanning mirror, which is placed in a mount AG-M050N-S from Newport. It is controlled by a piezo-motor Agilis AG-UC2-UC8 also from Newport. The lens system L5 consists of two cylindrical lenses working as a Galilean telescope and is used to circularize the 343 nm laser beam. Then the laser beam enters the optical unit. The optical unit housing and the fluorescence optical system are the same as in the previous experiments (Chapter 4). The excitation path is modified as in the following. When the focusing lens L6 is absent, the sample is illuminated by a collimated UV beam. With the focusing lens L6 inserted, the laser beam is focused at the bottom of the cup. The inset photograph in Fig. 6.1 shows the beam scanning system.

The laser emission is synchronized with the detection unit by the FPGA, see Fig. 3.6. After each FPGA trigger pulse, one Q-switched pulse is emitted. The trigger pulse train from the FPGA defines the repetition rate of the Q-switched laser and the measurement.

The main differences between laser, the light emitting diode (LED) and flash lamp excitation are summarized in Table 6.1. Firstly, the laser emission spectrum is narrower by a factor of 50 and 240, compared to the LED and the flash lamp, respectively. The spectral overlap is calculated for assay 2 and is normalized for the largest overlap from the laser excitation. The spectral overlap is decreased by 17% and by 35% for the LED and filtered flash lamp excitation, respectively. Secondly, the laser emission exhibits significantly shorter pulse width and correspondingly higher peak power: by 5 and 2 orders of magnitude for the LED and the flash lamp, respectively. Thirdly, the laser beam is spatially coherent and thus has a Gaussian profile in a test cup, while the LED and the flash lamp are spatially incoherent and approach a top-hat distribution, see Fig. 3.4 and 3.5. Finally, the laser beam is linearly

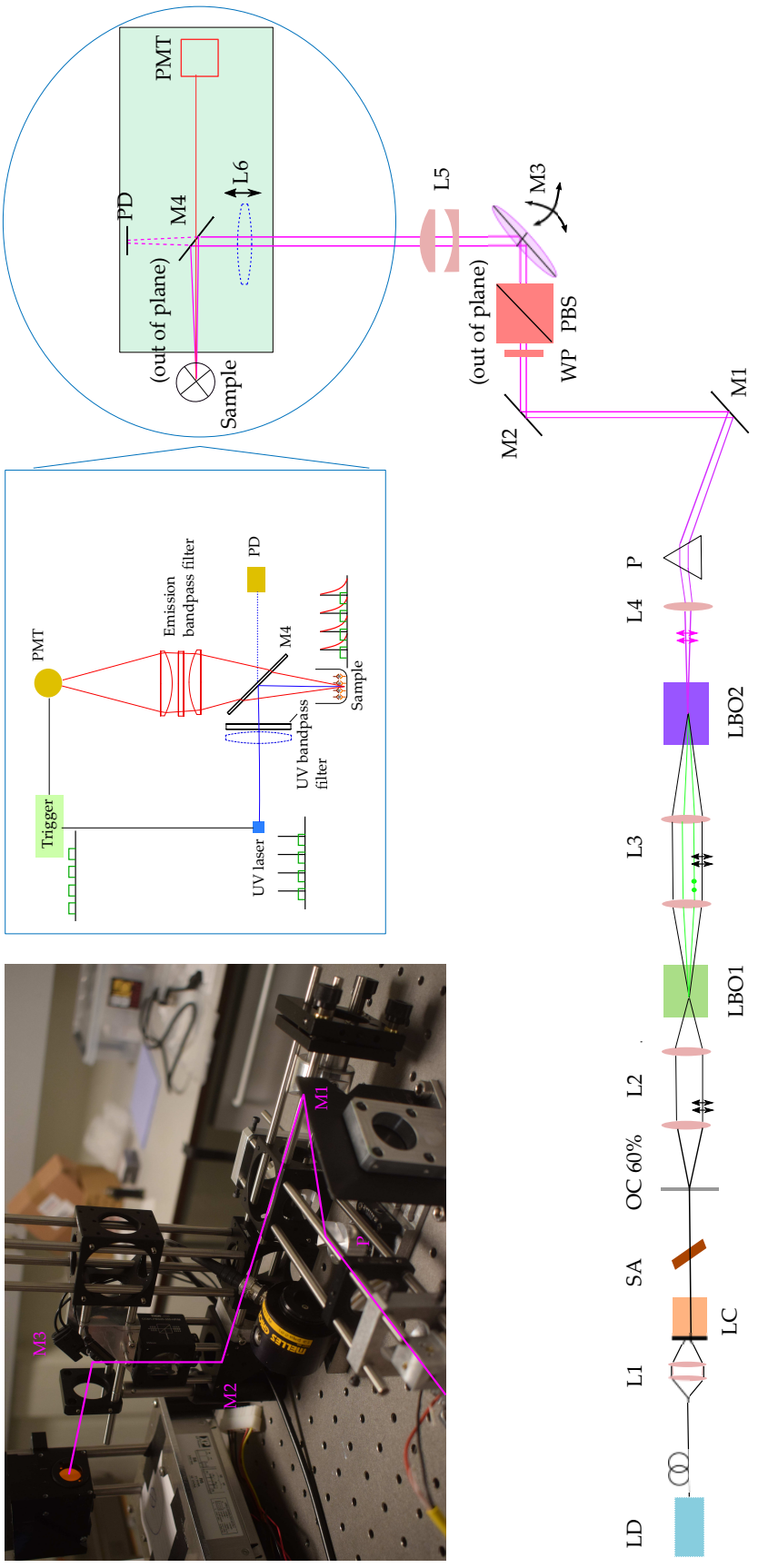


Figure 6.1: Experimental setup of laser based fluorescence system: LD - laser diode, L1-L6 - lens systems, LC - laser crystal, SA - saturable absorber, OC - output coupler, LBO1 and LBO2 - nonlinear crystals, P - prism, M1-M4 - mirrors, WP - half wave plate at 343 nm, PBS - polarizing beam splitter, PMT - photomultiplier tube, PD - photodiode.

polarized. However, the impact of the polarization on the fluorescence is unknown.

Table 6.1: Summary of the most relevant parameters of the employed light sources: spectral bandwidth, FWHM ($\Delta\lambda$), normalized spectral overlap with assay 2, pulse width ($\tau_p$), spatial coherence and linear polarization.

| Light source | $\Delta\lambda$, nm | Spectral overlap | $\tau_p$ | Spatial coh. | Polarization |
|---|---|---|---|---|---|
| Laser | 0.2 | 1 | 2.3 ns | yes | yes |
| LED | 10 | 0.83 | 200 µs | no | no |
| Flash lamp (filtered) | 48 | 0.65 | 200 ns | no | no |

With these differences in mind, we performed laser induced fluorescence measurements in immunoassays.

## 6.2 PHOTOBLEACHING STUDY

The photobleaching study performed in Section 4.5 was repeated using the laser excitation. The reason being that the peak power of the laser excitation pulse is by 5 orders of magnitude ($10^5$) higher compared to that of the LED excitation. We investigated if the considerably higher peak power affects the photobleaching rates. The laser energy density is calculated using the effective area $A_{eff}$ that is equal to that of a Gaussian elliptic with beam radii $w_x$ and $w_y$.

Figure 6.2 shows the normalized fluorescence signal from sample cups (LQC1) measured with hsTnI (assay 2) with a concentration of 30 ng/L and blank cups (AB) as a function of laser excitation energy density. Data previously measured with the LED system (shown in Fig. 4.9) is also plotted here for comparison. The laser exposure level was 1.8 kW/mm$^2$. The measured data were fitted to double exponential functions.

Photobleaching rate constants are shown in Table 6.2. The sample cups are bleached approximately with the same rate when excited by the laser compared to the LED. However, the blank cups are bleached significantly faster with the LED excitation, compared to the laser for the same excitation energy density. At the same time, it was shown in Fig. 4.9 that blank cups generally exhibit high variation. Photobleaching of several blank cups were measured in Fig. 4.9 and the corresponding photobleaching constants differed by 13% and 28% for $j_{b1}$ and $j_{b2}$, respectively, see Table 4.8. The difference between the photobleaching constants here is larger than the variation reported in Table 4.8. The reason is unknown.

## 6.3 HIGH-SENSITIVITY TROPONIN I MEASUREMENT

The procedure is described in the following. The test cups were first processed by a Radiometer AQT90 FLEX immunoassay (IA) analyzer. The analyzer employs the LED based excitation optical unit, developed in Chapter 4. The excitation system was *system 2*. The fluorescence optical system was improved by increasing the acceptance angle of the first lens in the emission optics, which is facing the sample. The theoretical improvement of the

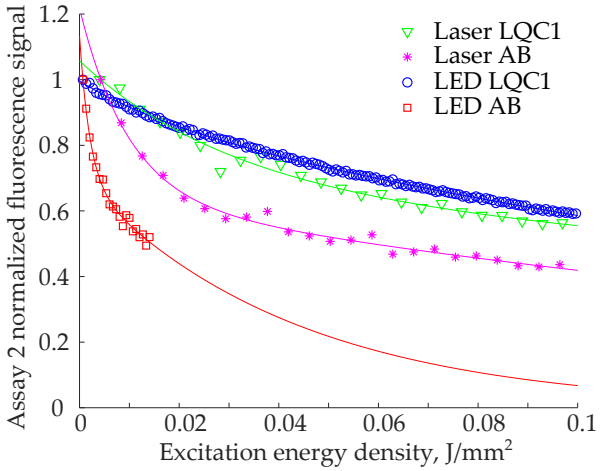


Figure 6.2: Normalized fluorescence signal as a function of excitation energy density showing photobleaching of: sample cup processed with 30 ng/L, measured with hsTnI (assay 2); blank cup processed with assay buffer. The data were fitted to double exponential functions. Laser exposure level is 1.8 kW/mm$^2$.

Table 6.2: Photobleaching rate constants of test cups with a hsTnI concentration of 30 ng/L (LQC1), blank cup (AB) obtained by curve fitting for replicates measured with assay 2. The exposure level corresponds to 1.8 kW/mm$^2$.

| | Laser | | LED | |
|---|---|---|---|---|
| | LQC1 | AB | LQC1 | AB |
| $j_{b1}$, mJ/mm$^2$ | 30.0 | 9.8 | 17.7 | 2.0 |
| 95% CI | [26.0; 35.5] | [8.0; 12.6] | [15.2; 21.1] | [1.5; 3.2] |
| $j_{b2}$, mJ/mm$^2$ | 460.5 | 236.6 | 233.2 | 42.7 |
| 95% CI | [427.2; 499.3] | [198.9; 292.0] | [226.2; 240.6] | [30.7; 70.4] |

collected fluorescence signal is 90% compared to the old system. In the analyzer, the test cups were exposed to 5x1000 cycles of light pulses with a pulse energy of 10.7 µJ each, corresponding to a LED current of 1200 mA and a pulse width of 200 µs. The sample cups are processed with LQC samples. The blank cups are processed with assay buffer (AB). After processing, the cups were removed from the analyzer and transported to Risø campus facilities.

The test cups were then measured by the laser excited time-resolved fluorescence system. The laser beam size was determined with a knife-edge method, measured after mirror M3 in the sample plane. The beam was collimated by the L4 lens. The cylindrical lenses L5 were not inserted. The experimental data and corresponding Gaussian fitting curves are shown in Fig. 6.3(a). The determined beam radii, $w_x$ and $w_y$ are 1.54 mm and 0.95 mm, respectively. This corresponds to an ellipticity of 1.6. The effective area $A_{eff}$ of the laser beam is calculated for a Gaussian elliptic beam with beam radii $w_x$ and $w_y$, respectively:

$$A_{eff} = \frac{\pi w_x w_y}{2} \tag{6.1}$$

The effective beam area is 2.3 $mm^2$, which is by a factor of 7 smaller than the LED illumination area.

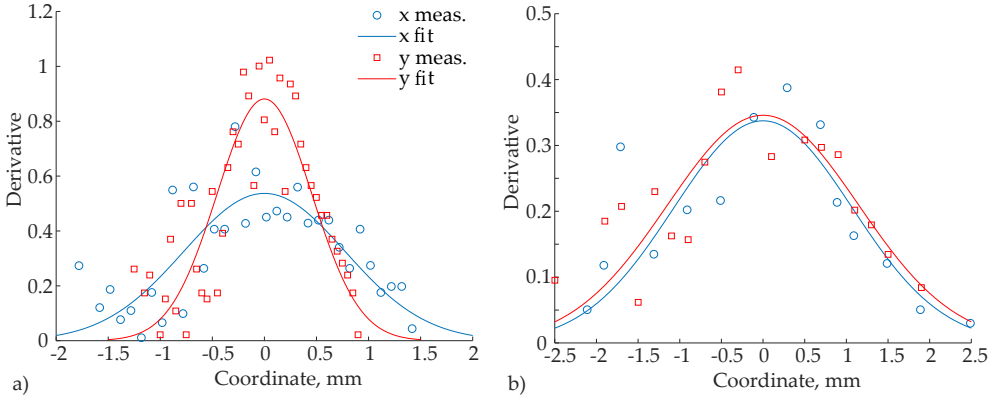


Figure 6.3: Intensity profiles of the laser beam at 343 nm: a) collimated, with the beam radii $w_x$ and $w_y$ of 1.54 mm and 0.95 mm, respectively; the effective area was 2.3 $mm^2$; b) shaped with the cylindrical lenses L5, with beam radii $w_x$ and $w_y$ of 2.05 mm and 2.26 mm, respectively; the effective area was 7.3 $mm^2$. The dots are measured values using the knife-edge method, solid lines are Gaussian fits.

Table 6.3 shows the measurement parameters and the statistical data. 9 replicates of the sample cups were processed with LQC1 with a concentration of 30 ng/L. 12 replicates of blank cups were processed with AB. The data from the analyzer was divided by a factor of 5, so that only 1000 cycles were taken into account. This was done in order to avoid bleaching effects, which would impact the measurements if the samples were exposed to extra 5000 cycles during the laser excitation measurement. Instead, only 1000 cycles are compared. The timing of the laser and LED were equal: pre-delay time of 300 µs, and a measurement window of 1600 µs. The repetition rate of the laser based system was 100 or 90 Hz and not higher in order to avoid damage of the achromatic lenses, L3. The laser measurements are performed with a magnification of the 1030 nm laser beam in the LBO1 crystal equal to −1.25 (lens system L2).

Following conclusions are drawn from Table 6.3. Firstly, the fluorescence signal of the sample cups (LQC1) is decreased only by 4% using laser excitation, compared to the LED instrument. At the same time, the short pulse width of the laser should increase the signal by 10% (with equal pulse energy and area), see Fig. 3.10(b). The better spectral overlap should increase the fluorescence signal by 17%, see Table 6.1. Total expected improvement was 27%, for the same excitation energy. The specific signal per unit area, $\frac{S_f}{A_{eff}}$, is 20492 counts/$mm^2$ and 3116 counts/$mm^2$ for the laser and LED excitation, respectively. So, the illumination area decreased by a factor of 7, and the specific signal per unit area increased by a similar factor of 6.5 using laser excitation, compared to LED. Therefore, the fluorophores are not saturated by laser excitation, and the fluorophores distribution is rather uniform. The improvement of 27% predicted by the temporal and spectral parameters was not observed.

Secondly, the blank signal (AB cups) increased by 56% using laser excitation. As discussed in Section 4.6, the fluorescence decay of a blank cup consists of two exponential decays, with decay constants of 1049 µs and 124

Table 6.3: Statistical data of test cups of assay 2, processed with a sample LQC1 with a concentration of 30 ng/L, and with AB (0 ng/L), measured with the laser based unit and the LED based IA analyzer.

| Parameter | Laser system | LED based AQT90 |
|---|---|---|
| $A_{eff}$, mm$^2$ | 2.3 | 16 |
| Ellipticity | 1.6 | |
| Number of pulses | 1000 | 1000* |
| Average power, mW | 1.05 | 2.68 |
| Frequency, Hz | 100 | 250 |
| Pulse energy, µJ | 10.5 | 10.7 |
| Pulse width | 2.3 ns | 200 µs |
| | LQC1 sample | |
| $\mu_S$, counts | 49395.9 | 51314.0 |
| $\sigma_S$, counts | 5138.6 | 2939.3 |
| $CV_S$ | 0.10 | 0.06 |
| $\frac{S_f}{A_{eff}}$, counts/mm$^2$ | 20492 | 3116 |
| | AB sample | |
| $\mu_B$, counts | 2263.9 | 1450.8 |
| $\sigma_B$, counts | 590.8 | 174.0 |
| $CV_B$ | 0.26 | 0.12 |
| $\frac{\mu_B}{A_{eff}}$, counts/mm$^2$ | 984 | 91 |
| SNR | 9.1 | 16.9 |
| S/B | 20.8 | 34.4 |

*data divided by 5

µs, respectively, see Fig. 4.12 and Table 4.10. For the longer decay time, the fluorescence signal increase when excited by the laser is by 10%, compared to LED excitation, as previously discussed, see Fig. 3.10. For the shorter decay of 124 µs, the fluorescence signal increases by 50% when excited by the laser, compared to the LED excitation. Moreover, the background signal per unit area ($\frac{\mu_B}{A_{eff}}$) was 984 counts/mm$^2$ and 91 counts/mm$^2$ using laser and LED excitation, respectively. So, the background signal per unit area increased by a factor of 11 which is significantly larger than the illumination area scaling (7).

Finally and most importantly, the variation of both sample cups and blank cups ($CV_S$ and $CV_B$), is significantly higher when excited by the laser: by 67% and by 116%, respectively. Consequently, with laser excitation the SNR and S/B decreased by a factor of 1.9 and 1.7, respectively. We believe that there are two main reasons for the increased variation and hence the decreased performance: the pulse energy fluctuation of the laser; and the non-symmetrical illumination area of the laser. It was experienced that the laser operated in an unstable fashion during the measurement, probably due to the damage of the LBO1 crystal. This was discussed in Section 5.2. We observed the values measured by a reference photodiode, PD, see Fig. 6.1. The reference photodiode is placed opposite to the UV light source and measures the corresponding excitation average power, which is transmitted through the dichroic mirror, M4. The variation of the reference photodiode values

was 5% and 21% for the measurements of LQC1 and AB cups, respectively. However, there was no direct correlation between the reference photodiode readings and the measured fluorescence signal for individual test cups. For this reason, the fluctuation of the reference photodiode readings for individual test cups was not taken into account in the post-processing of the fluorescence signal data. To eliminate these sources of variation, two changes were performed in the next experiments: the 1030 nm beam magnification (i.e. beam size) in LBO1 crystal was increased from −1.25 to −2 to decrease the laser intensity; then, the laser beam area was circularized to investigate the impact of the illumination area symmetry on the observed variation.

In the following experiment the laser beam area is circularized with two cylindrical lenses, L5. The beam size is measured with the knife-edge method in the sample plane. The experimental data and the corresponding Gaussian fitting curves are shown in Fig. 6.3(b). The determined beam radii, $w_x$ and $w_y$ are 2.05 mm and 2.26 mm, respectively. The effective beam area was 7.3 $mm^2$ and the ellipticity was 1.1. The laser illumination area is now smaller by a factor of 2 compared to the LED illumination area. With the current system, it was not possible to obtain an illumination area equal to the LED illumination area due to the spatial coherence of the beam. To create a top-hat distribution in the test cup, the spatial coherence has to be destroyed in further experiments. Table 6.4 shows the experimental parameters and statistical data. The number of replicates was the same: 9 replicates of sample cups, processed with LQC1 (concentration of 30 ng/L), and 12 replicates of blank cups, processed with AB. The data from the analyzer was divided by 5, so that only 1000 cycles were taken into account.

Firstly, with the larger laser area resulted in the fluorescence signal decrease of 28%. However, the reading of the reference photodiode was 0.83 of that measured in the first experiment (see Table 6.3). Therefore, the measured averaged fluorescence signal is now compensated for the averaged reference photodiode reading. Then, the compensated fluorescence signal is 42925 counts. Specific signal per unit area is 5755 counts/$mm^2$. This is by 14% smaller than that for LED. So, with an illumination area decreased by a factor of 2.2, the specific signal per unit area increased by a similar factor of 1.9 using laser excitation compared to LED. Again, the predicted improvement of 27% was not confirmed. Compared to the first experiment (see Table 6.3), the following was observed. With the laser illumination area increased by a factor of 3.2, the specific signal per unit area decreased by a nearly the same, factor of 3.6, which is to be expected. Therefore, as in the first experiment, we conclude that the laser excitation does not saturate the europium chelates and their distribution is rather uniform in sample cups. In addition, the laser excitation did not show the theoretical improvement in fluorescence signal.

Secondly, the blank cups signal decreased by 40% compared to LED. The background signal per unit area was 125 counts/$mm^2$ and 81 counts/$mm^2$ using laser and LED excitation, respectively. So, the illumination area decreased by a factor of 2 and the background signal per area increased by a factor of 1.5 using laser excitation compared to LED. In turn, using laser excitation, the background signal per unit area was 984 counts/$mm^2$ and 125 counts/$mm^2$ for the experiment 1 and 2, respectively. Thus, the background signal per unit area has decreased by a factor of 7.9 when the laser illumina-

Table 6.4: Statistical data of test cups of assay 2, processed with a sample LQC1 with a concentration of 30 ng/L, and with AB (0 ng/L), measured with the laser based unit and the LED based IA analyzer.

| Parameter | Laser system | LED based AQT90 |
|---|---|---|
| $A_{eff}$, $mm^2$ | 7.3 | 16 |
| Ellipticity | 1.1 | |
| Number of pulses | 1000 | 1000[a] |
| Average power, mW | 0.94 | 2.68 |
| Frequency, Hz | 90 | 250 |
| Pulse energy, µJ | 10.4 | 10.7 |
| Pulse width | 2.3 ns | 200 µs |
| | LQC1 sample | |
| $\mu_S$, counts | 35628 (42925)[b] | 49792 |
| $\sigma_S$, counts | 2839 | 3794 |
| $CV_S$ | 0.08 | 0.08 |
| $\frac{S_f}{A_{eff}}$, counts/$mm^2$ | 4774 (5755)[b] | 3031 |
| | AB sample | |
| $\mu_B$, counts | 776 (913)[b] | 1301 |
| $\sigma_B$, counts | 72.6 | 168 |
| $CV_B$ | 0.09 | 0.13 |
| $\frac{\mu_B}{A_{eff}}$, counts/$mm^2$ | 125 | 81 |
| SNR | 12.3 | 12.8 |
| S/B | 44.9 | 37.2 |

[a] data divided by 5

[b] compensated for the reference photodiode reading

tion area was increased by a factor of 3.2. The increase by 50% of the blank cup signal, observed in the first experiment, was not observed here. So, the background signal per unit area does not scale linearly with the illumination area. Apparently, the larger laser illumination area (7.3 $mm^2$) resulted in less background noise. Probably, this is due to a non-uniformity of the distribution of background noise sources in blank cups. To confirm the hypothesis, further investigations are needed.

Thirdly, the variation of blank cups counts ($CV_B$) decreased significantly compared to both the LED excitation and the laser excitation having a non-symmetrical illumination area (Table 6.3). At the same time, the variation of the reference photodiode readings is 11% and 9% for the LQC1 and AB cups, respectively. The pulse energy fluctuation corresponds to an additional noise source in Eq. 4.3. Interestingly, a much larger variation of the pulse energy of the laser, compared to the LED, does not impact the measurement result. The reason being that the cup-to-cup variation dominates over the pulse energy fluctuations. Measured with LED based IA analyzer, the reference photodiode variation is about 0.1% and can be neglected (compared to the signal variation, $CV_S$ of 8% in Table 6.4). Only in the case when the pulse energy variation is comparable to or larger than the cup-to-cup variation, it affects the measurement, as seen in Table 6.3 for the blank cups. The SNR

is nearly the same and S/B is improved by 21% compared to the LED based instrument.

The pulse energy fluctuation measured in Section 5.3 was 2.4%, see Fig. 5.23. However, that pulse energy fluctuation was measured with a temperature stabilized system. In these experiments, it was observed that for fluorescence measurements, the pulse energy fluctuation of the laser increases because the system is not temperature stabilized. However, as discussed above, the excitation pulse energy variation is not the dominating noise source in our measurements.

In order to confirm that the fluorophore excitation is not saturated using laser excitation, the following experiment was performed. The sample cups were excited with 50% of the excitation peak power. For the LED, the peak power was reduced by decreasing the LED current. For the laser, the peak power was reduced using a half wave plate and a polarizer. So, the pulse duration was constant. The fluorescence signal decreased by a factor of 2 for both LED and laser based excitation of the cups LQC1 (data not shown). For the blank cups, the fluorescence signal decreased by a factor of 2 with LED and by 1.4 for laser excitation.

## 6.4 CONCLUSION

In this chapter, laser based time-resolved fluorescence measurements of troponin I in immunoassay were discussed. The laser illumination area was 2.3 $mm^2$ and 7.3 $mm^2$ (ellipticity of 1.6 and 1.1, respectively). The measurements were compared to the developed LED based immunoassay analyzer. The excitation pulse energy of the laser was equal to that of the LED based system. The LED illumination area was 16 $mm^2$, i.e. by a factor of 7 and 2 larger than the laser illumination areas, respectively. Following conclusions were formulated.

Firstly, the fluorescence signal per unit area was larger by a factor of 6.5 and 1.9 using a laser excitation area of 2.3 $mm^2$ and 7.3 $mm^2$, respectively, compared to the LED excitation. These improvement factors nearly match the factors by which the illumination area was decreased using laser excitation. Therefore, 1) the high peak power of laser excitation does not saturate the europium chelates in our experiments; 2) the distribution of chelates in sample cups is rather uniform. Moreover, the smaller laser illumination area of 2.3 $mm^2$ resulted in an increased fluorescence signal per unit area by a factor of 3.5 compared to the larger area (7.3 $mm^2$), as expected. Interestingly, the predicted improvement of fluorescence signal by 27% was not confirmed experimentally.

Secondly, with a laser excitation area of 2.3 $mm^2$, the blank cups signal increased by 56% compared to that of the LED excitation. Likely, this was partially due to the short exponential decay from the blank cups of 124 µs, which theoretically increased the background value by 50%. However, the fluorescence signal per unit area was larger by a factor of 11 and 1.5 using a laser excitation area of 2.3 $mm^2$ and 7.3 $mm^2$, respectively, compared to the LED excitation. Moreover, with the laser illumination area increased by a factor of 3, the signal of the blank cups per unit area decreased by a factor of 8 and was then even smaller by 30% compared to the LED. Apparently, larger laser illumination area results in reduced background noise compared

to both, smaller laser illumination area and the LED. The background noise per unit area does not scale linearly with the illumination area. Therefore, it is beneficial to have reduced brightness in the center of a blank cup. We suggest that it is likely caused by a non-uniformity of noise sources distribution in blank cups, or a nonlinearity of background noise signal with excitation peak power. Further investigations are needed to confirm these hypotheses.

Thirdly, the non-symmetry of the UV illumination area and the pulse energy fluctuation of the light source impact the signal variation significantly. With a circularly illuminated laser area (ellipticity of 1.1), the variation decreased from 26% to 8% for the blank cups, compared to a non-symmetric area. Moreover, with the circularly illuminated area, this variation was comparable to that of the LED, although the pulse energy fluctuation was higher. This was due to the dominant noise contribution from the cup-to-cup variation in the measurements. Thus, with the circularly illuminated area the SNR was similar and S/B was improved by 21% compared to the LED excitation.

Finally, it was demonstrated that the narrowband laser excitation did not saturate the sample cups at the employed pulse energy level. In addition, the photobleaching study showed that for sample cups, the photobleaching rates with the laser excitation were similar to those with the LED excitation.

An important conclusion was that the distribution of background noise sources in blank cups was non-uniform and impacted the measurements considerably. Further investigation is required to understand the distribution of immunocomplexes in sample cups, and noise sources in blank cups. Unluckily, this investigation was not performed in this project due to time constraints. However, the developed optical system incorporates the possibility of scanning.

# 7

# CONCLUSION AND OUTLOOK

## 7.1 CONCLUSION

In this work, time-resolved fluorescence measurement systems for immunoassays were investigated, based on two novel light sources. Two systems were developed: firstly, a system based on LEDs at 340 nm, and 2) a system based on a solid-state passively Q-switched solid state laser emitting light at 343 nm.

For the first time to our knowledge, a time-resolved fluorescence measurement system based on a 340 nm LED was successfully employed for immunoassays detection. Two optical systems were designed, with a different magnification of $-5$ and $-4$, respectively. The first optical system was designed to collect up to 80% of the LED light, emitted from the 1x1mm$^2$ Lambertian chip and focused to an area of 5x5 mm$^2$ in the bottom of a test cup with a 6.7 mm diameter. The illuminated area was three times larger than that of the Xenon flash lamp, however still small enough to excite fluorescence efficiently and subsequently be imaged on a PMT photocathode. The LED was operated at 370 mA in pulsed mode. The LED pulse width was 200 µs and the pulse energy was 5.1 µJ when operated below the specified maximum current limit. This pulse energy was equal to the pulse energy from the Xenon flash lamp. A three orders of magnitude increase in pulse width using LED excitation compared to the flash lamp was estimated to reduce the fluorescence signal by a mere 10% due to the long fluorescence lifetime of the europium label. The signal-to-background was improved significantly when excited by the LED, expectedly due to the absence of the flash lamps afterglow and narrower emission spectrum of the LED. A test with real immunoassay samples of the cardiac marker TnI (200 ng/L), showed comparable SNR for the LED and Xenon flash lamp respectively, for the same excitation pulse energy. A SNR of 35 (measurement time 3 s), equal to that of the flash lamp system, was obtained without overdriving the LED and could be further improved by increasing the LED current.

The second, optimized LED based system, was designed to have a collection efficiency of 50% and an illumination area of 4x4 mm$^2$. The optimized illumination area had a more optimal overlap with the chemically active area in the cup and avoided generating interfering background fluorescence from outside of the chemically active area. The LED current was at 455 mA, still below the maximum specification current. The optimized LED based system was tested in an immunoassay instrument intended for PoC use. The laboratory tests were performed with a standard TnI assay and a research prototype hsTnI assay. The LoD was improved by a factor of 5, from 9.5 ng/L to 1.9 ng/L, for the standard TnI assay when measured with the LED based instrument, thus significantly outperforming the state-of-the-art flash lamp OU based instrument. The improvement was achieved primarily by optimizing the overlap between the UV illumination area and the chemically active area where the immunocomplexes are located.

In the implementation of the novel research hsTnI assay using the LED based instrument we have obtained a detection limit of 0.22 ng/L measured on plasma, showing an improvement by a factor of 3 compared to the flash lamp based instrument. Using data for an existing hsTnI assay from an external manufacturer, we estimated the required value of LoD to be 0.43 ng/L in order to meet the hsTnI criteria, which are imposed by the need of more sensitive assays for earlier diagnosis of AMI. The combination of LED excitation and the prototype hsTnI assay enabled LoD of 0.22 ng/L, which is 49% below the estimated requirement. We believe our preliminary results are an important step in the development of the hsTnI assay for PoC testing and that the hsTnI criteria will soon be documented in PoC systems using LED excitation, ultimately leading to more accurate interpretation of clinical tests and earlier diagnosis and rule-out of AMI.

A model was suggested, which included the background and noise contributions to describe time-resolved immunoassay detection. The model can be generally applied to lanthanide-based heterogeneous time-resolved fluoroimmunoassays. We showed that the temporal decay of the background in the system included two exponential terms. The SNR can be improved by choosing an optimal pre-delay time to largely match the short background decay time (about hundreds of μs), whereas the long lifetime decay term originating from the non-specific binding of the tracer antibodies to the cups inner walls cannot be filtered. We also demonstrated that the cup-to-cup variation was a dominating noise contributor that was limiting the instrument performance.

In the second part of the project, a low repetition rate, simple and cost-effective 343 nm solid-state laser source was developed through THG of a passively Q-switched diode-pumped Yb:YAG laser source. For the first time to our knowledge, a passively Q-switched, solid-state UV laser at 343 nm was demonstrated. At 343 nm, a pulse energy of 20 μJ, pulse width of 2.3 ns, and operation at a repetition rate of 100 Hz was obtained, converted from 1030 nm with pulse energy of 190 μJ and pulse width of 5.4 ns. The UV-IR conversion efficiency was 10.4% at 100 Hz, which is comparable to that obtained with mode locked lasers. The UV laser emits pulses on demand and can be electronically synchronized with the detection circuit. The low repetition rate matched particularly well the millisecond scale lifetime of lanthanide fluorophores, targeting applications in fluoroimmunoassays and time-resolved fluorescence spectroscopy. The 343 nm output targeted the excitation peak of the lanthanides. The timing jitter of the developed laser was 32.6 μs which was only 0.3% relative to the cycle of the measurement (10 ms) and 3.2% relative to a typical lifetime of europium (1 ms). In immunoassay measurements, this was smaller than typical cup-to-cup variations (6%). The timing jitter, however, can be avoided by implementing an optical feedback system. The UV pulse-to-pulse peak power fluctuation was 2.4%. The impact of these noise sources can be further decreased by signal averaging.

A few guidelines were given based on the analysis of the observed saturable absorbers damage. The recommended surface quality of intracavity components for high-power systems is 10-5 S-D. High power Yb:YAG lasers with the intracavity intensity exceeding 0.2 GW/cm$^2$ or 1.0 J/cm$^2$ (1030 nm, 10 ns), are recommended to be designed as microchip resonators with no air-crystal surface interface, despite the LIDT of 0.5 GW/cm$^2$ (1064 nm, 10

ns) provided by most crystal vendors. In addition, it was concluded that the uncertainty of doping concentration of MgO in MgO:$LiNbO_3$ crystal considerably hampers its employment for the SHG of 1030 nm. The phase-matching temperature of two 5%MgO:$LiNbO_3$ crystals for SHG of 1030 nm was not observed in the temperature range from 14°C to 100°C.

A photobleaching study was performed both with LED and laser excitation. Photobleaching constants were reported. We showed that photobleaching effects do not affect the immunoassay measurements. In addition, the significantly higher peak power of the laser excitation, compared to that of the LED (by 5 orders of magnitude), did not damage the fluorescent chelates. The photobleaching constants of sample cups using laser excitation were similar to that using LED excitation.

Finally, a laser based time-resolved fluorescence system was developed and for the first time successfully employed for measurements of troponin I in immunoassays. The laser illumination area was 2.3 $mm^2$ and 7.3 $mm^2$ with an ellipticity of 1.6 and 1.1, respectively. That was smaller by a factor of 7 and 2 compared to the LED illumination area (16 $mm^2$), respectively. The fluorescence signal per unit area was larger by a factor of 6.5 and 1.9 using the laser excitation compared to LED excitation. These factors nearly match the scaling of the illumination area. Therefore, 1) the employed fluorophores are not saturated by the laser excitation; 2) the distribution of the fluorophores in sample cups is rather uniform. However, the theoretically predicted improvement of the fluorescence signal by 27% using laser excitation was not observed.

In turn, the blank cups signal increased by 56% using laser excitation area of 2.3 $mm^2$, compared to the LED excitation. Probably, this was partially due to the short exponential decay of blank cups of 124 µs, which theoretically increases the background value by 50%. Using a laser illumination area of 2.3 $mm^2$ and 7.3 $mm^2$, the fluorescence signal per unit area (blank cups) was larger by a factor of 11 and 1.5, compared to LED. Moreover, with the laser area increased by a factor of 3 (7.3 $mm^2$ vs 2.3 $mm^2$), the fluorescence signal of the blank cups decreased by a factor of 8 and was then even smaller by 30% compared to the LED. Apparently, the background noise per unit area did not scale linearly with the illumination area. Therefore, we conclude that using the larger laser illumination area, the background noise is reduced, compared to both: the smaller laser area and the LED. Potentially, this was caused by the non-uniformity of the noise sources distribution in blank cups, or nonlinear response of the background noise to excitation peak power. This observation should be further investigated in future work.

In addition, we demonstrated that the non-symmetry of UV illumination area and pulse energy fluctuation of the light source impacted the signal variation significantly. With a circular laser illumination area (ellipticity of 1.1), the background variation decreased by 2% and 17% for the sample and blank cups, respectively, compared to a non-symmetric area. Moreover, with the symmetric laser area, this variation was comparable to that of the LED excitation, although the pulse energy fluctuation is significantly higher. This was due to the dominating noise source from the cup-to-cup variation in the measurements.

To sum up the results from the laser induced time-resolved fluorescence measurements in immunoassays: similar SNR was obtained, and S/B was

improved by 21% using laser excitation with a circularized laser area of 7.3 $mm^2$, compared to the LED excitation. Using a larger laser illumination area (7.3 $mm^2$ vs. 2.3 $mm^2$), the background noise was reduced. Further investigations are needed to study the distribution of noise sources in blank cups.

## 7.2 OUTLOOK

Potential improvements of the developed time-resolved system for immunoassays are discussed in the following. Coming back to Eq. 2.1, which nicely combines all the parameters of a time-resolved fluorescence measurement, we enumerate the following improvements.

In the designed system, the excitation efficiency, $\eta_{exc}$ is rather high (0.5). However, the fluorescence system efficiency, $\eta_{fl}$ can be improved significantly by employing a transmission-type fluorescence measurement system. In such a system, the fluorescent light is collected below the test cup. In this case, the collection is not limited by the cup geometry and the acceptance angle of the emission optical system. Instead, a much larger angle, ultimately limited by a semi-sphere of $2\pi$, can be collected. A preliminary design of such a system was performed, which showed a theoretical improvement of the collection efficiency by a factor of 22. Moreover, in the current system, the detector is limited by the requirement of low dark current. Thus, the detector quantum yield, Q, is relatively low. However, when the fluorescence signal is increased by a factor of 22, a detector with larger dark current, but also larger quantum yield, can be employed.

It was suggested based on the experimental data that the noise sources distribution in blank cups is non-uniform, which impacts the measurements considerably. Further investigation is required to understand the distribution of immunocomplexes in the sample cups as well as noise sources in the blank cups. The information of the chelates distribution will allow us to design an optical system with an optimized overlap. The optimized overlap would take into account both the distribution in sample and blank cups which is supposedly different, and thus maximize the fluorescence signal per unit area while simultaneously minimizing the background noise.

The high spatial beam quality of the laser allows for 2D scanning of the sample cups. The developed laser based optical system incorporates the possibility of scanning and can be employed for further investigation of the distribution of chemically active elements in test cups. Hopefully, this investigation will be continued. Moreover, the focusing capabilities also enable such sensitive technique as single molecule detection [32]. A single molecule detection immunoassay employing a laser as an excitation source has been demonstrated [33, 34].

For future work, the laser source will benefit from a frequency selective component stabilizing the output spectrum. Moreover, the setup will benefit from a SHG crystal which does not have to be temperature stabilized in an oven. This will result in a compact setup without lenses between the nonlinear crystals. Recently, a few promising compact designs were reported [133, 134]. In addition, it was reported that acceptance bandwidth in nonlinear crystals can be increased by a walk-off compensation, i.e. combining crystals with opposite birefringence-induced walk-off directions [132]. This

in turn can result in improved conversion efficiency. In this work, we have used LBO crystals of 10 mm and 20 mm, respectively, arranged to compensate spatial beam walk-off. However, it was not possible to obtain positive result due to limited mechanical stability. For walk-off compensation, better mechanical mounts are needed with more precise position control.

The laser based optical unit also suffers from temperature and mechanical instabilities. We believe that a more robust mechanical design and temperature management will improve the stability significantly.

# APPENDIX

## A.1 IMMUNOASSAYS

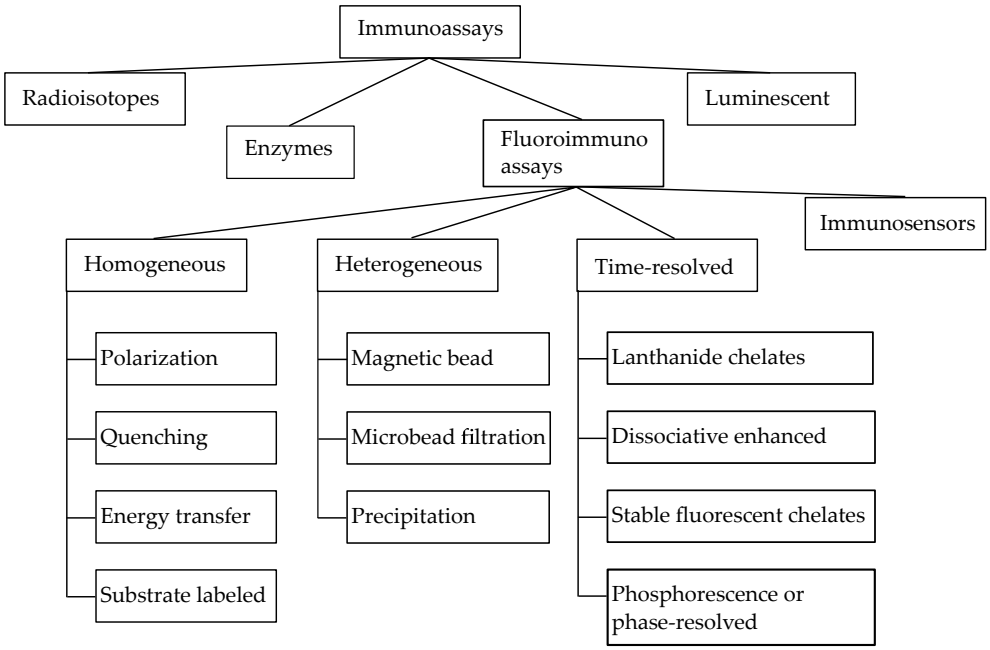


Figure A.1: Immunoassays

## A.2 TIME-RESOLVED FLUORIMETRY

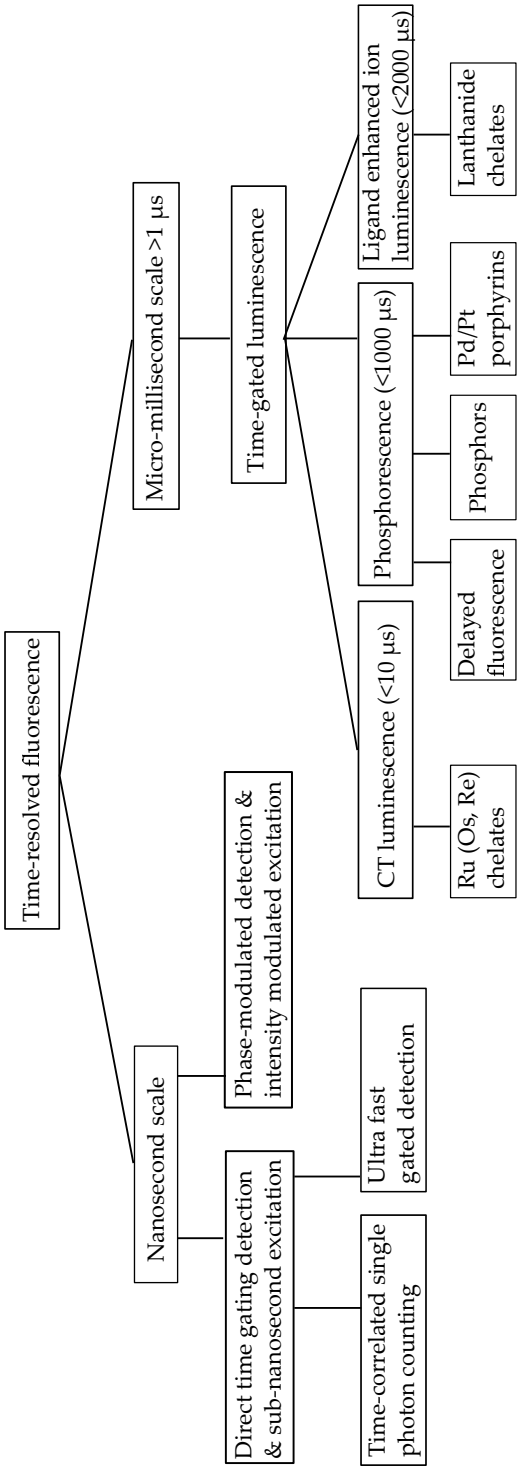


Figure A.2: Time-resolved fluorimetry

## A.3 CONTINUOUS WAVE YB:YAG LASER

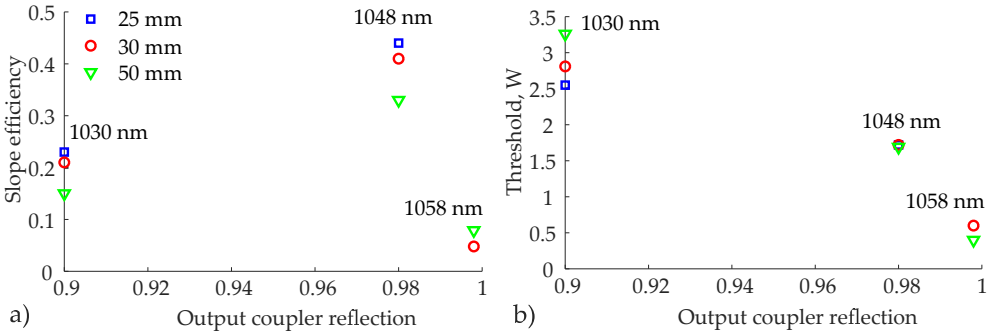


Figure A.3: Slope efficiency (a) and threshold (b) of the continuous wave (CW) Yb:YAG laser as a function of the output coupler (OC) reflection. In a nonselective cavity, different lasing wavelengths are preferred. The pump beam diameter is 210 µm. The OC radius of curvature is 100 mm.

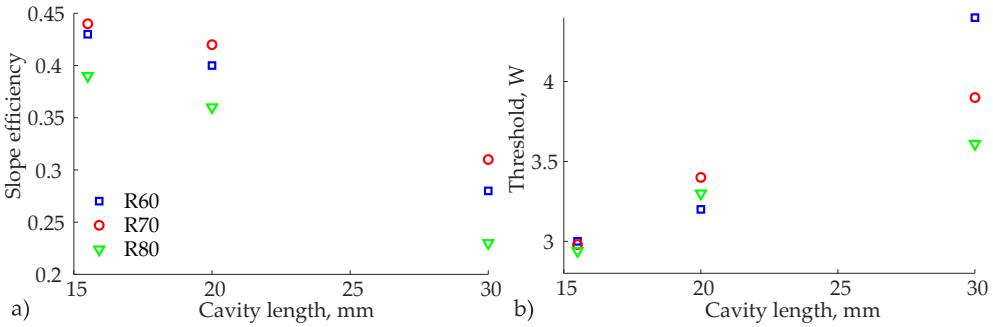


Figure A.4: Slope efficiency (a) and threshold (b) of the CW Yb:YAG laser as a function of cavity length for different output coupler reflection. The pump beam diameter is 210 µm. The OC is a plane mirror.

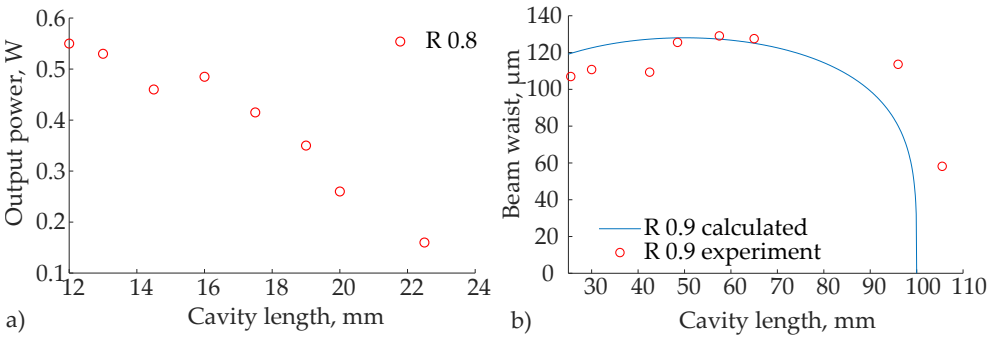


Figure A.5: a) CW output power as a function of cavity length. The pump beam diameter is 349.7 µm. The OC is a plane mirror with a reflection of 0.8. Incident pump power is 8.3 W. b) Measured laser beam waist at the output coupler as a function of cavity length. Incident pump power is 8.3 W. The OC is a curved mirror with reflection of 0.9, and radius of curvature of 100 mm.

# BIBLIOGRAPHY


[1] P. St-Louis. Status of point-of-care testing: promise, realities, and possibilities. *Clinical Biochemistry*, 33(6):427–440, 2000.

[2] P. von Lode. Point-of-care immunotesting: approaching the analytical performance of central laboratory methods. *Clinical Biochemistry*, 38(7): 591–606, 2005.

[3] S. Aldous, A. M. Richards, P. M. George, L. Cullen, W. A. Parsonage, D. Flaws, C. M. Florkowski, R. W. Troughton, J. W. O'Sullivan, C. M. Reid, L. Bannister, and M. Than. Comparison of new point-of-care troponin assay with high sensitivity troponin in diagnosing myocardial infarction. *International Journal of Cardiology*, 177(1):182–186, 2014.

[4] S. Hjortshøj, P. Venge, and J. Ravkilde. Clinical performance of a new point-of-care cardiac troponin I assay compared to three laboratory troponin assays. *Clinica Chimica Acta*, 412(3):370–375, 2011.

[5] E. Soini and H. Kojola. Time-resolved fluorometer for lanthanide chelates–a new generation of nonisotopic immunoassays. *Clinical Chemistry*, 29(1):65–68, 1983.

[6] J. R. Lakowicz. *Principles of Fluorescence Spectroscopy*. Springer US, 2006. ISBN 978-0-387-46312-4.

[7] G. Marriott, R. M. Clegg, D. J. Arndt-Jovin, and T. M. Jovin. Time resolved imaging microscopy. Phosphorescence and delayed fluorescence imaging. *Biophysical Journal*, 60(6):1374–1387, 1991.

[8] E. J. Hennink, R. De Haas, N. P. Verwoerd, and H. J. Tanke. Evaluation of a time-resolved fluorescence microscope using a phosphorescent Pt-porphine model system. *Cytometry*, 24(4):312–320, 1996.

[9] I. Hemmilä and V. Laitala. Progress in lanthanides as luminescent probes. *Journal of Fluorescence*, 15(4):529–542, 2005.

[10] J.-C. G. Bünzli. Lanthanide luminescence for biomedical analyses and imaging. *Chemical Reviews*, 110(5):2729–2755, 2010.

[11] E. P. Diamandis and T. K. Christopoulos. Europium chelate labels in time-resolved fluorescence immunoassays and DNA hybridization assays. *Analytical Chemistry*, 62(22):1149A–1157A, 1990.

[12] J. R. Lakowicz, H. Szmacinski, K. Nowaczyk, and M. L. Johnson. Fluorescence lifetime imaging of free and protein-bound NADH. *Proceedings of the National Academy of Sciences*, 89(4):1271–1275, 1992.

[13] L. Seveus, M. Väisälä, S. Syrjänen, M. Sandberg, A. Kuusisto, R. Harju, J. Salo, I. Hemmilä, H. Kojola, and E. Soini. Time-resolved fluorescence imaging of europium chelate label in immunohistochemistry and in situ hybridization. *Cytometry Part A*, 13(4):329–338, 1992.

[14] R. Connally, D. Veal, and J. Piper. Flash lamp-excited time-resolved fluorescence microscope suppresses autofluorescence in water concentrates to deliver an 11-fold increase in signal-to-noise ratio. *Journal of Biomedical Optics*, 9(4):725–734, 2004.

[15] Hamamatsu Photonics K. K. Compact 5W xenon flash lamp module, 2018. URL http://www.hamamatsu.com/eu/en/product/category/1001/3024/L9455/index.html.

[16] D. Jin, R. Connally, and J. Piper. Long-lived visible luminescence of UV LEDs and impact on LED excited time-resolved fluorescence applications. *Journal of Physics D: Applied Physics*, 39(3):461, 2006.

[17] R. Connally, D. Jin, and J. Piper. High intensity solid-state UV source for time-gated luminescence microscopy. *Cytometry Part A*, 69(9):1020–1027, 2006.

[18] S. W. Kettlitz, C. Moosmann, S. Valouch, and U. Lemmer. Sensitivity improvement in fluorescence-based particle detection. *Cytometry Part A*, 85(9):746–755, 2014.

[19] D. Jin, R. Connally, and J. Piper. Practical time-gated luminescence flow cytometry. II: Experimental evaluation using UV LED excitation. *Cytometry Part A*, 71(10):797–808, 2007.

[20] D. Jin, J. A. Piper, R. C. Leif, S. Yang, B. C. Ferrari, J. Yuan, G. Wang, L. M. Vallarino, and J. W. Williams. Time-gated flow cytometry: an ultra-high selectivity method to recover ultra-rare-event μ-targets in high-background biosamples. *Journal of biomedical optics*, 14(2):024023, 2009.

[21] N. Gahlaut and L. W. Miller. Time-resolved microscopy for imaging lanthanide luminescence in living cells. *Cytometry Part A*, 77(12):1113–1125, 2010.

[22] K. Davitt, Y.-K. Song, W. R. Patterson, A. V. Nurmikko, M. Gherasimova, J. Han, Y.-L. Pan, and R. K. Chang. 290 and 340 nm UV LED arrays for fluorescence detection from single airborne particles. *Optics Express*, 13(23):9548–9555, 2005.

[23] H. Peng, E. Makarona, Y. He, Y.-K. Song, A. V. Nurmikko, J. Su, Z. Ren, M. Gherasimova, S.-R. Jeon, G. Cui, and J. Han. Ultraviolet light-emitting diodes operating in the 340 nm wavelength range and application to time-resolved fluorescence spectroscopy. *Applied Physics Letters*, 85(8):1436–1438, 2004.

[24] S. Sartania, Z. Cheng, M. Lenzner, G. Tempea, C. Spielmann, F. Krausz, and K. Ferencz. Generation of 0.1-TW 5-fs optical pulses at a 1-kHz repetition rate. *Optics Letters*, 22(20):1562–1564, 1997.

[25] J. Rothhardt, C. Rothhardt, M. Müller, A. Klenke, M. Kienel, S. Demmler, T. Elsmann, M. Rothhardt, J. Limpert, and A. Tünnermann. 100 W average power femtosecond laser at 343 nm. *Optics Letters*, 41(8):1885–1888, 2016.

[26] J.-P. Negel, A. Loescher, A. Voss, D. Bauer, D. Sutter, A. Killi, M. Abdou Ahmed, and T. Graf. Ultrafast thin-disk multipass laser amplifier delivering 1.4 kW (4.7 mJ, 1030 nm) average power converted to 820 W at 515 nm and 234 W at 343 nm. *Optics Express*, 23(16):21064–21077, 2015.

[27] J. Dong, K. Ueda, A. Shirakawa, H. Yagi, T. Yanagitani, and A. A. Kaminskii. Composite Yb:YAG/Cr4+:YAG ceramics picosecond microchip lasers. *Optics Express*, 15(22):14516–14523, 2007.

[28] J. Dong, Y. Ren, and H. Cheng. >1 MW peak power, an efficient Yb:YAG/Cr4+:YAG composite crystal passively Q-switched laser. *Laser Physics*, 24(5):055801, 2014.

[29] M. Tsunekane and T. Taira. High peak power, passively Q-switched Yb:YAG/Cr:YAG micro-lasers. *IEEE Journal of Quantum Electronics*, 49 (5):454–461, 2013.

[30] B. Li, B. Sun, and H. Mu. High-efficiency generation of 355 nm radiation by a diode-end-pumped passively Q-switched Nd: YAG/Nd:$YVO_4$ laser. *Applied Optics*, 55(10):2474–2477, 2016.

[31] N. K. Seitzinger, K. D. Hughes, and F. E. Lytle. Optimization of signal-to-noise ratios in time-filtered fluorescence detection. *Analytical Chemistry*, 61(23):2611–2615, 1989.

[32] W. E. Moerner and D. P. Fromm. Methods of single-molecule fluorescence spectroscopy and microscopy. *Review of Scientific Instruments*, 74 (8):3597–3619, 2003.

[33] Singulex. The Sgx Clarity System, 2018. URL https://www.singulex.com/sgx-clarity-system/.

[34] C. P. McCarthy, N. E. Ibrahim, A. Lyass, Y. Li, H. K. Gaggin, M. L. Simon, R. Mukai, P. Gandhi, N. Kelly, S. R. Motiwala, R. R. J van Kimmenade, J. M. Massaro, R. B. D'Agostino, and J. L. Januzzi. Single-molecule counting of high-sensitivity troponin I in patients referred for diagnostic angiography: Results from the CASABLANCA (Catheter Sampled Blood Archive in Cardiovascular Diseases) study. *Journal of the American Heart Association*, 7(6):e007975, 2018.

[35] I. A. Hemmilä. *Applications of Fluorescence in Immunoassays*. A Wiley-Interscience publication. Wiley, 1991. ISBN 9780471510918.

[36] S. A. Berson and R. S. Yalow. Quantitative aspects of the reaction between insulin and insulin-binding antibody. *The Journal of Clinical Investigation*, 38(11):1996–2016, 1959.

[37] G. Barnard, F. Kohen, H. Mikola, and T. Lövgren. Measurement of estrone-3-glucuronide in urine by rapid, homogeneous time-resolved fluoroimmunoassay. *Clinical Chemistry*, 35(4):555–559, 1989.

[38] I. Hemmilä. Time-resolved fluorometric determination of terbium in aqueous solution. *Analytical Chemistry*, 57(8):1676–1681, 1985.

[39] I. Hemmilä, S. Dakubu, V.-M. Mukkala, H. Siitari, and T. Lövgren. Europium as a label in time-resolved immunofluorometric assays. *Analytical Biochemistry*, 137(2):335 – 343, 1984.

[40] E. Reichstein, Y. Shami, M. Ramjeesingh, and E. P. Diamandis. Laser-excited time-resolved solid-phase fluoroimmunoassays with the new europium chelate 4, 7-bis (chlorosulfophenyl)-1, 10-phenanthroline-2, 9-dicarboxylic acid as label. *Analytical Chemistry*, 60(10):1069–1074, 1988.

[41] S. Yamada, F. Miyoshi, K. Kano, and T. Ogawa. Highly sensitive laser fluorimetry of europium (III) with1, 1, 1-trifluoro-4-(2-thienyl)-2, 4-butanedione. *Analytica Chimica Acta*, 127:195–198, 1981.

[42] H. Déchaud, R. Bador, F. Claustrat, and C. Desuzinges. Laser-excited immunofluorometric assay of prolactin, with use of antibodies coupled to lanthanide-labeled diethylenetriaminepentaacetic acid. *Clinical Chemistry*, 32(7):1323–1327, 1986.

[43] I. Hemmilä and T. Ståhlberg. *Bioanalytical Applications of Labelling Technologies: A Review of Trends and Opportunities in Biospecific Assay, Based on the Product Offering of Wallac, an EG & G Company*. Wallac Oy, 1994. ISBN 9519489290.

[44] A. K. Hagan and T. Zuchner. Lanthanide-based time-resolved luminescence immunoassays. *Analytical and Bioanalytical Chemistry*, 400(9): 2847–2864, 2011.

[45] D. Jin, R. Connally, and J. Piper. Practical time-gated luminescence flow cytometry. I: Concepts. *Cytometry Part A*, 71(10):783–796, 2007.

[46] F. S. Apple, P. O. Collinson, and IFCC Task Force on Clinical Applications of Cardiac Biomarkers. Analytical characteristics of high-sensitivity cardiac troponin assays. *Clinical Chemistry*, 58(1):54–61, 2012.

[47] C. A. Burtis, N. W. Tietz, E. R. Ashwood, and D. E. Bruns. *Tietz Textbook of Clinical Chemistry and Molecular Diagnostics*. Number vb. 564 in Tietz Textbook of Clinical Chemistry and Molecular Diagnostics. Elsevier Saunders, 2006. ISBN 9780721601892.

[48] J. W. Lichtman and J.-A. Conchello. Fluorescence microscopy. *Nature Methods*, 2(12):910, 2005.

[49] T. Lövgren, L. Meriö, K. Mitrunen, M.-L. Mäkinen, M. Mäkelä, K. Blomberg, T. Palenius, and K. Pettersson. One-step all-in-one dry reagent immunoassays with fluorescent europium chelate label and time-resolved fluorometry. *Clinical Chemistry*, 42(8):1196–1201, 1996.

[50] L. Välimaa, J. Ylikotila, H. Kojola, T. Soukka, H. Takalo, and K. Pettersson. Streptavidin-coated spot surfaces for sensitive immunoassays using fluorescence surface readout. *Analytical and Bioanalytical Chemistry*, 391(6):2135–2144, 2008.

[51] K. Pettersson, T. Katajamäki, K. Irjala, V. Leppanen, K. Majamaa-Voltti, and P. Laitinen. Time-resolved fluorometry (TRF)-based immunoassay concept for rapid and quantitative determination of biochemical myocardial infarction markers from whole blood, serum and plasma. *Luminescence*, 15(6):399–407, 2000.

[52] R. N. Nurmukhametov, L. V. Volkova, and S. P. Kabanov. Fluorescence and absorption of polystyrene exposed to UV laser radiation. *Journal of Applied Spectroscopy*, 73(1):55–60, 2006.

[53] P. von Lode, J. Rosenberg, K. Pettersson, and H. Takalo. A europium chelate for quantitative point-of-care immunoassays using direct surface measurement. *Analytical Chemistry*, 75(13):3193–3201, 2003.

[54] CLSI. Evaluation of detection capability for clinical laboratory measurement procedures; approved guideline-second edition. *CLSI document EP17-A2*, Wayne, PA: Clinical and Laboratory Standards Institute, 2012.

[55] J. Schiettecatte, E. Anckaert, and J. Smitz. Interferences in immunoassays. In *Advances in Immunoassay Technology*, chapter 3. InTech, 2012.

[56] World Health Organization. Cardiovascular diseases (CVDs), 2017. URL http://www.who.int/mediacentre/factsheets/fs317/en/.

[57] T. E. Caragher, B. B. Fernandez, F. L. Jacobs, and L. A. Barr. Evaluation of quantitative cardiac biomarker point-of-care testing in the emergency department. *Journal of Emergency Medicine*, 22(1):1–7, 2002.

[58] K. Thygesen, J. S. Alpert, A. S. Jaffe, M. L. Simoons, B. R. Chaitman, H. D. White, Writing Group on behalf of the Joint ESC/ACCF/AHA/WHF Task Force for the Universal Definition of Myocardial Infarction, and Authors/Task Force Members Chairpersons. Third universal definition of myocardial infarction. *European Heart Journal*, 33 (20):2551–2567, 2012.

[59] P. M. McKie, D. M. Heublein, C. G. Scott, M. Lou Gantzer, R. A. Mehta, R. J. Rodeheffer, M. M. Redfield, J. C. Burnett, and A. S. Jaffe. Defining high-sensitivity cardiac troponin concentrations in the community. *Clinical Chemistry*, 59(7):1099–1107, 2013.

[60] D. M. Kimenai, R. M. A. Henry, C. J. H. van der Kallen, P. C. Dagnelie, M. T. Schram, C. D. A. Stehouwer, J. D. E. van Suijlen, M. Niens, O. Bekers, S. J. Sep, N. C. Schaper, M. P. van Dieijen-Visser, and S. J. Meex. Direct comparison of clinical decision limits for cardiac troponin T and I. *Heart*, 102(8):610–616, 2016.

[61] M. Franzini, V. Lorenzoni, S. Masotti, C. Prontera, D. Chiappino, D. Della Latta, M. Daves, I. Deluggi, M. Zuin, L. Ferrigno, A. Mele, F. Marcucci, C. A. Caserta, P. Surace, A. Messineo, G. Turchetti, C. Passino, M. Emdin, and A. Clerico. The calculation of the cardiac troponin T 99th percentile of the reference population is affected by age, gender, and population selection: a multicenter study in Italy. *Clinica Chimica Acta*, 438:376–381, 2015.

[62] T. Zeller, F. Ojeda, F. J Brunner, P. Peitsmeyer, T. Münzel, H. Binder, N. Pfeiffer, M. Michal, P. S. Wild, S. Blankenberg, and K. J. Lackner. High-sensitivity cardiac troponin I in the general population–defining reference populations for the determination of the 99th percentile in the gutenberg health study. *Clinical Chemistry and Laboratory Medicine (CCLM)*, 53(5):699–706, 2015.

[63] R. Twerenbold, A. Jaffe, T. Reichlin, M. Reiter, and C. Mueller. High-sensitive troponin T measurements: what do we gain and what are the challenges? *European Heart Journal*, 33(5):579–586, 2012.

[64] T. Keller, T. Zeller, F. Ojeda, S. Tzikas, L. Lillpopp, C. Sinning, P. Wild, S. Genth-Zotz, A. Warnholtz, E. Giannitsis, M. Möckel, C. Bickel, D. Peetz, K. Lackner, S. Baldus, T. Münzel, and S. Blankenberg. Serial changes in highly sensitive troponin I assay and early diagnosis of myocardial infarction. *JAMA*, 306(24):2684–2693, 2011.

[65] K. Wildi, M. R. Gimenez, R. Twerenbold, T. Reichlin, C. Jaeger, A. Heinzelmann, C. Arnold, B. Nelles, S. Druey, P. Haaf, P. Hillinger, N. Schaerli, P. Kreutzinger, Y. Tanglay, T. Herrmann, Z. M. Weidmann, L. Krivoshei, M. Freese, C. Stelzig, C. Puelacher, K. Rentsch, S. Osswald, and C. Mueller. Misdiagnosis of myocardial infarction related to limitations of the current regulatory approach to define clinical decision values for cardiac troponin. *Circulation*, 131(23):2032–2040, 2015.

[66] T. Zeller, H. Tunstall-Pedoe, O. Saarela, F. Ojeda, R. B. Schnabel, T. Tuovinen, M. Woodward, A. Struthers, M. Hughes, F. Kee, V. Salomaa, K. Kuulasmaa, and S. Blankenberg. High population prevalence of cardiac troponin I measured by a high-sensitivity assay and cardiovascular risk estimation: the MORGAM biomarker project scottish cohort. *European Heart Journal*, 35(5):271–281, 2013.

[67] P. Hedberg and G. Wennecke. A preliminary evaluation of the AQT90 FLEX TnI immunoassay. *Clinical Chemistry and Laboratory Medicine*, 47 (3):376–378, 2009.

[68] S. Eriksson, T. Ilva, C. Becker, J. Lund, P. Porela, K. Pulkki, L.-M. Voipio-Pulkki, and K. Pettersson. Comparison of cardiac troponin I immunoassays variably affected by circulating autoantibodies. *Clinical Chemistry*, 51(5):848–855, 2005.

[69] H. Sund, K. Blomberg, N. Meltola, and H. Takalo. Design of novel, water soluble and highly luminescent europium labels with potential to enhance immunoassay sensitivities. *Molecules*, 22(10), 2017.

[70] G. J. Hahn and W. Q. Meeker. *Statistical intervals: a guide for practitioners*. John Wiley & Sons, Inc., 1991.

[71] M. Latva, H. Takalo, V.-M. Mukkala, C. Matachescu, J. C. Rodríguez-Ubis, and Jo. Kankare. Correlation between the lowest triplet state energy level of the ligand and lanthanide (III) luminescence quantum yield. *Journal of Luminescence*, 75(2):149–169, 1997.

[72] CLSI/NCCLS. Protocols for determination of limits of detection and limits of quantitation; approved guideline. *NCCLS document EP17-A*, Wayne, PA: Clinical and Laboratory Standards Institute, 2004.

[73] C. Hönninger, R. Paschotta, M. Graf, F. Morier-Genoud, G. Zhang, M. Moser, S. Biswal, J. Nees, A. Braun, G. A. Mourou, I. Johannsen, A. Giesen, W. Seeber, and U. Keller. Ultrafast ytterbium-doped bulk lasers and laser amplifiers. *Applied Physics B*, 69(1):3–17, 1999.

[74] H. Z. Cao, F. J. Liu, H. M. Tan, H. Y. Peng, M. H. Zhang, Y. Q. Chen, B. Zhang, B. L. Chen, and C. J. Wang. Laser diode end-pumped Yb: YAG/LBO green laser. *Laser Physics*, 19(5):919, 2009.

[75] P. Ye, S. Zhu, Z. Li, H. Yin, P. Zhang, S. Fu, and Z. Chen. Passively Q-switched dual-wavelength green laser with an Yb:YAG/Cr4+:YAG/YAG composite crystal. *Optics Express*, 25(5): 5179–5185, 2017.

[76] V. V. Ter-Mikirtychev, M. A. Dubinskii, and V. A. Fromzel. Q-switched, TEMoo-mode, diode-pumped Yb3+:YAG laser with extended tunability. *Optics Communications*, 197(4-6):403–411, 2001.

[77] S. Chénais, F. Druon, S. Forget, F. Balembois, and P. Georges. On thermal effects in solid-state lasers: The case of ytterbium-doped materials. *Progress in Quantum Electronics*, 30(4):89–153, 2006.

[78] G. C. Sun, Y. D. Li, M. Zhao, X. Y. Chen, J. B. Wang, and G. B. Chen. Highly efficient CW intracavity frequency-doubled Yb:YAG-LBO laser at 515 nm under 968 nm diode laser pumping. *Laser Physics*, 21(5):883, 2011.

[79] W. P. Risk. Modeling of longitudinally pumped solid-state lasers exhibiting reabsorption losses. *The Journal of the Optical Society of America B*, 5(7):1412–1423, 1988.

[80] F. D. Patel, E. C. Honea, J. Speth, S. A. Payne, R. Hutcheson, and R. Equall. Laser demonstration of Yb/sub 3/Al/sub 5/O/sub 12/(YbAG) and materials properties of highly doped Yb:YAG. *IEEE Journal of Quantum Electronics*, 37(1):135–144, 2001.

[81] Y. Kalisky, C. Labbe, K. Waichman, L. Kravchik, U. Rachum, P. Deng, J. Xu, J. Dong, and W. Chen. Passively Q-switched diode-pumped Yb:YAG laser using Cr4+-doped garnets. *Optical materials*, 19(4):403–413, 2002.

[82] S. Chénais, F. Balembois, F. Druon, G. Lucas-Leclin, and P. Georges. Thermal lensing in diode-pumped ytterbium lasers-part II: evaluation of quantum efficiencies and thermo-optic coefficients. *IEEE Journal of Quantum Electronics*, 40(9):1235–1243, 2004.

[83] S. Chénais, F. Balembois, F. Druon, G. Lucas-Leclin, and P. Georges. Thermal lensing in diode-pumped ytterbium lasers-Part I: theoretical analysis and wavefront measurements. *IEEE Journal of Quantum Electronics*, 40(9):1217–1234, 2004.

[84] F. Augé, F. Druon, F. Balembois, P. Georges, A. Brun, F. Mougel, G. Aka, and D. Vivien. Theoretical and experimental investigations of a diode-pumped quasi-three-level laser: the Yb/sup 3+/-doped Ca/-sub 4/GdO (BO/sub 3/)/sub 3/(Yb: GdCOB) laser. *IEEE Journal of Quantum Electronics*, 36(5):598–606, 2000.

[85] T. Y. Fan. Heat generation in Nd:YAG and Yb:YAG. *IEEE Journal of Quantum Electronics*, 29(6):1457–1459, 1993.

[86] W. Koechner. *Solid-state laser engineering*, volume 1. Springer, 2013.

[87] J. Dong, Y. Ren, G. Wang, and Y. Cheng. Efficient laser performance of Yb:Y3Al5O12/Cr4+: 3Al5O12 composite crystals. *Laser Physics Letters*, 10(10):105817, 2013.

[88] A. M. Malyarevich, I. A. Denisov, K. V. Yumashev, V. P. Mikhailov, R. S. Conroy, and B. D. Sinclair. V:YAG–a new passive Q-switch for diode-pumped solid-state lasers. *Applied Physics B: Lasers and Optics*, 67(5): 555–558, 1998.

[89] J. Dong. Numerical modeling of CW-pumped repetitively passively Q-switched Yb:YAG lasers with Cr:YAG as saturable absorber. *Optics Communications*, 226(1-6):337–344, 2003.

[90] J. Šulc, T. Koutnỳ, H. Jelínková, K. Nejezchleb, and V. Škoda. Yb: YAG/Cr:YAG composite crystal with external and microchip resonator. In *Solid State Lasers XXI: Technology and Devices*, volume 8235, page 823522. International Society for Optics and Photonics, 2012.

[91] R. Feldman, Y. Shimony, and Z. Burshtein. Passive Q-switching in Nd YAG/Cr4+:YAG monolithic microchip laser. *Optical Materials*, 24(1-2): 393–399, 2003.

[92] W. Jiang, Y. Liu, W. Chen, S. Zhu, Z. Chen, G. Zhang, Y. Chen, and Z. Chen. Composite Yb:YAG/Cr4+:YAG/YAG crystal passively Q-switched lasers at 1030 nm. *Applied Optics*, 54(7):1834–1838, 2015.

[93] W. Zheng, T. Chen, and H. Liu. Diode-pumped passively Q-switched YAG/Yb:YAG laser with Cr4+:YAG as a saturable absorber. *Journal of Russian Laser Research*, 34(2):109–113, 2013.

[94] Lidaris. Laser-induced damage morphology, 2018. URL http://lidaris.com/glossary-2/laser-induced-damage-morphology/.

[95] M. Bass, L. S. Weichman, S. Vigil, and B. K. Brickeen. The temperature dependence of Nd/sup 3+/ doped solid-state lasers. *IEEE Journal of Quantum Electronics*, 39(6):741–748, 2003.

[96] O. Kimmelma, I. Tittonen, and S. C. Buchter. Thermal tuning of laser pulse parameters in passively Q-switched Nd:YAG lasers. *Applied Optics*, 47(23):4262–4266, 2008.

[97] M. Nie, Q. Liu, E. Ji, and M. Gong. End-pumped temperature-dependent passively Q-switched lasers. *Applied Optics*, 54(28):8383–8387, 2015.

[98] M. Tsunekane and T. Taira. Temperature and polarization dependences of Cr:YAG transmission for passive Q-switching. In *2009 Conference on Lasers and Electro-Optics and 2009 Conference on Quantum electronics and Laser Science Conference*, pages 1–2, June 2009. doi: 10.1364/CLEO.2009.JTuD8.

[99] H. P. H. Cheng, P. Tidemand-Lichtenberg, O. B. Jensen, P. E. Andersen, P. M. Petersen, and C. Pedersen. All passive synchronized Q-switching of a quasi-three-level and a four-level Nd: YAG laser. *Optics Express*, 18(23):23987–23993, 2010.

[100] A. E. Siegman. *Lasers*. University Science Books, 1986.

[101] Y. P. Lan, Y. F. Chen, and S. C. Wang. Repetition-rate dependence of thermal loading in diode-end-pumped Q-switched lasers: influence of energy-transfer upconversion. *Applied Physics B*, 71(1):27–31, 2000.

[102] K. Rottwitt and P. Tidemand-Lichtenberg. *Nonlinear Optics: Principles and Applications*. CRC Press, 2014. ISBN 9781466565821.

[103] R. W. Boyd. *Nonlinear Optics, Third Edition*. Academic Press, Inc., Orlando, FL, USA, 3rd edition, 2008. ISBN 0123694701, 9780123694706.

[104] W. P. Risk, T. R. Gosnell, and A. V. Nurmikko. *Compact Blue-Green Lasers*. Cambridge, UK: Cambridge University Press, January 2003.

[105] G. D. Boyd and D. A. Kleinman. Parametric interaction of focused Gaussian light beams. *Journal of Applied Physics*, 39(8):3597–3639, 1968.

[106] V. G. Dmitriev, G. G. Gurzadyan, and D. N. Nikogosyan. *Handbook of nonlinear optical crystals*, volume 64. Springer, 2013.

[107] V. G. Dmitriev and D. N. Nikogosyan. Effective nonlinearity coefficients for three-wave interactions in biaxial crystal of mm2 point group symmetry. *Optics Communications*, 95(1-3):173–182, 1993.

[108] Covesion Ltd. Covesion guide to PPLN. Material properties of Lithium Niobate, 2018. URL https://www.covesion.com/support/covesion-guide-to-ppln/material-properties-of-lithium-niobate.html.

[109] J. L. Nightingale, W. J. Silva, G. E. Read, W. J. Kozlovski, and R. L. Byer. Lasers and nonlinear optical materials. In *Proc. SPIE*, volume 681, page 20, 1986.

[110] O. I. Lavrovskaya, N. I. Pavlova, and A. V. Tarasov. Second harmonic generation of light from an AIG:Nd3+ laser in an optically biaxial crystal of KTiOPO4. *Soviet Phyics Crystallography*, 31:678–681, 1986.

[111] D. N. Nikogosyan. *Nonlinear Optical Crystals: A Complete Survey*. Springer-Verlag New York, 2005.

[112] A. Borsutzky, R. Brünger, C. Huang, and R. Wallenstein. Harmonic and sum-frequency generation of pulsed laser radiation in BBO, LBO, and KD*P. *Applied Physics B*, 52(1):55–62, 1991.

[113] D. A. Roberts. Simplified characterization of uniaxial and biaxial nonlinear optical crystals: a plea for standardization of nomenclature and conventions. *IEEE Journal of Quantum Electronics*, 28(10):2057–2074, Oct 1992.

[114] B. Boulanger, J. P. Fève, G. Marnier, B. Ménaert, X. Cabirol, P. Villeval, and C. Bonnin. Relative sign and absolute magnitude of d(2) nonlinear coefficients of KTP from second-harmonic-generation measurements. *Journal of the Optical Society of America B*, 11(5):750–757, 1994.

[115] R. C. Eckardt, H. Masuda, Y. X. Fan, and R. L. Byer. Absolute and relative nonlinear optical coefficients of KDP, KD* P, BaB/sub 2/O/-sub 4/, LiIO/sub 3/, MgO: LiNbO/sub 3/, and KTP measured by phase-matched second-harmonic generation. *IEEE Journal of Quantum Electronics*, 26(5):922–933, 1990.

[116] T. Ukachi, R. J. Lane, W. R. Bosenberg, and C. L. Tang. Measurements of noncritically phase-matched second-harmonic generation in a $LiB_3O_5$ crystal. *Applied Physics Letters*, 57(10):980–982, 1990.

[117] J.-J. Zondy, M. Abed, and A. Clairon. Type-II frequency doubling at $\lambda$= 1.30 μm and $\lambda$= 2.53 μm in flux-grown potassium titanyl phosphate. *Journal of the Optical Society of America B*, 11(10):2004–2015, 1994.

[118] O. Gayer, Z. Sacks, E. Galun, and A. Arie. Temperature and wavelength dependent refractive index equations for MgO-doped congruent and stoichiometric $LiNbO_3$. *Applied Physics B*, 91(2):343–348, 2008.

[119] A. Smith. SNLO. URL http://www.as-photonics.com/index.php.

[120] D. E. Zelmon, D. L. Small, and D. Jundt. Infrared corrected sellmeier coefficients for congruently grown lithium niobate and 5 mol.% magnesium oxide–doped lithium niobate. *Journal of the Optical Society of America B*, 14(12):3319–3322, 1997.

[121] A. L. Aleksandrovskiĭ, G. I. Ershova, G. K. Kitaeva, S. P. Kulik, I. I. Naumova, and V. V. Tarasenko. Dispersion of the refractive indices of $LiNbO_3$:Mg and $LiNbO_3$:Y crystals. *Soviet Journal of Quantum Electronics*, 21(2):225, 1991.

[122] D. H. Jundt, M. Kajiyama, D. Djukic, and M. Falk. Optical methods to characterize crystal composition of MgO-doped lithium niobate. *Journal of Crystal Growth*, 312(8):1109–1113, 2010.

[123] P. M. Bridenbaugh, J. R. Carruthers, J. M. Dziedzic, and F. R. Nash. Spatially uniform and alterable SHG phase-matching temperatures in lithium niobate. *Applied Physics Letters*, 17(3):104–106, 1970.

[124] Q. Liu, F. Lu, M. Gong, C. Li, and D. Ma. 15 W output power diode-pumped solid-state lasers at 515 nm. *Laser Physics Letters*, 4(1):30, 2006.

[125] X. Guo, W. Hou, H. Peng, H. Zhang, G. Wang, Y. Bi, A. Geng, Y. Chen, D. Cui, and Z. Xu. 4.44 W of CW 515 nm green light generated by intracavity frequency doubling Yb:YAG thin disk laser with LBO. *Optics Communications*, 267(2):451–454, 2006.

[126] L. Goldberg, B. Cole, C. McIntosh, V. King, A. D. Hays, and Stephen R. Chinn. Narrow-band 1 W source at 257 nm using frequency quadrupled passively Q-switched Yb:YAG laser. *Optics Express*, 24(15):17397–17405, 2016.

[127] S. P. Velsko, M. Webb, L. Davis, and C. Huang. Phase-matched harmonic generation in lithium triborate (LBO). *IEEE Journal of Quantum Electronics*, 27(9):2182–2192, 1991.

[128] K. Kato. Tunable UV generation to 0.2325 mu m in LiB/sub 3/O/sub 5. *IEEE Journal of Quantum Electronics*, 26(7):1173–1175, 1990.

[129] A. V. Egorysheva and V. M. Skorikov. Efficient nonlinear optical material BiB3O6 (BIBO). *Inorganic Materials*, 45(13):1461, 2009.

[130] B. Wu, N. Chen, C. Chen, D. Deng, and Z. Xu. Highly efficient ultraviolet generation at 355 nm in LiB3O5. *Optics Letters*, 14(19):1080–1081, 1989.

[131] D. N. Nikogosyan. Beta barium borate (BBO). *Applied Physics A*, 52(6): 359–368, 1991.

[132] A. V. Smith, D. J. Armstrong, and W. J. Alford. Increased acceptance bandwidths in optical frequency conversion by use of multiple walk-off-compensating nonlinear crystals. *Journal of the Optical Society of America B*, 15(1):122–141, 1998.

[133] J. Hirohashi, M. Hatori, M. Sakairi, S. Miyazawa, S. Takekawa, T. Taniuchi, and Y. Furukawa. 355nm generation by Fan-out PP-LBGO device. In *Lasers and Electro-Optics (CLEO), 2014 Conference on*, pages 1–2. IEEE, 2014.

[134] J. Hirohashi, T. Taniuchi, S. Makio, K. Imai, M. Hatori, H. Motegi, Y. Tomihari, M. Hoshi, and Y. Furukawa. Monolithic Fan-out PPMgSLT device for cascaded 355nm generation. In *CLEO: Science and Innovations*, pages SM4I–6. Optical Society of America, 2014.

[135] S.-L. Huang, T.-Y. Tsui, C.-H. Wang, and F.-J. Kao. Timing jitter reduction of a passively Q-switched laser. *Japanese Journal of Applied Physics*, 38(3A):L239, 1999.

[136] D. Nodop, J. Limpert, R. Hohmuth, W. Richter, M. Guina, and A. Tünnermann. High-pulse-energy passively Q-switched quasi-monolithic microchip lasers operating in the sub-100-ps pulse regime. *Optics Letters*, 32(15):2115–2117, 2007.

[137] J. B. Khurgin, F. Jin, G. Solyar, C.-C. Wang, and S. Trivedi. Cost-effective low timing jitter passively Q-switched diode-pumped solid-state laser with composite pumping pulses. *Applied Optics*, 41(6):1095–1097, 2002.

[138] B. Cole, L. Goldberg, C. W. Trussell, A. Hays, B. W. Schilling, and C. McIntosh. Reduction of timing jitter in a Q-switched Nd:YAG laser by direct bleaching of a Cr4+:YAG saturable absorber. *Optics Express*, 17(3):1766–1771, 2009.

[139] M. W. Smillie, M. Silver, S. T. Lee, and T. J. Cook. High single-pulse energy, passively Q-switched Nd:YAG laser for defence applications. In *Solid State Lasers XXIII: Technology and Devices*, volume 8959, page 89590Z. International Society for Optics and Photonics, 2014.

## COLOPHON

This document was typeset using the typographical look-and-feel `classicthesis` developed by André Miede. The style was inspired by Robert Bringhurst's seminal book on typography "*The Elements of Typographic Style*". `classicthesis` is available for both LaTeX and LyX:

http://code.google.com/p/classicthesis/

*Final Version* as of September 4, 2018 (`classicthesis`).